Experimental Investigation of Fan Rotor Response to Inlet Swirl Distortion

Dustin J. Frohnapfel

Thesis submitted to the Faculty of the
Virginia Polytechnic Institute and State University
in partial fulfillment of the requirements for the degree of

Master of Science
in
Mechanical Engineering

Walter F. O'Brien, Chair
K. Todd Lowe
Alfred L. Wicks

April 29, 2016
Blacksburg, Virginia

Keywords: Turbofan Engine, Inlet Distortion, Swirl, Secondary Flow, Ground Test

Experimental Investigation of Fan Rotor Response to Inlet Swirl Distortion

Dustin J. Frohnapfel

ABSTRACT

Next generation aircraft design focuses on highly integrated airframe/engine architectures that exploit advantages in system level efficiency and performance. One such design concept incorporates boundary layer ingestion which locates the turbofan engine inlet near enough to the lifting surface of the aircraft skin that the boundary layer is ingested and reenergized. This process reduces overall aircraft drag and associated required thrust, resulting in fuel savings and decreased emissions; however, boundary layer ingestion also creates unique challenges for the turbofan engines operating in less than optimal inlet flow conditions.

The engine inlet flow profiles predicted from boundary layer ingesting aircraft architectures contain complex distortions that affect the engine operability, durability, efficiency, and performance. One component of these complex distortion profiles is off-axial secondary flow, commonly referred to as swirl. As a means to investigate the interactions of swirl distortion with turbofan engines, an experiment was designed to measure distorted flow profiles in an operating turbofan research engine.

Three-dimensional flow properties were measured at discrete planes immediately upstream and immediately downstream of the fan rotor, isolating the component for analysis. Constant speed tests were conducted under clean and distorted test conditions. For clean tests, a straight cylindrical inlet duct was attached to the fan case; for distorted tests, a StreamVane swirl distortion generator was inserted into the inlet duct. The StreamVane was designed to induce a swirl distortion matching results of computation fluid dynamics models of a conceptual blended wing body aircraft at a plane upstream of the fan. The swirl distortion was then free to develop naturally within the inlet duct before being ingested by the engine.

Results from the investigation revealed that the generated swirl profile developed, mixed, and dissipated in the inlet duct upstream of the fan. Measurements immediately upstream of the fan rotor leading edge revealed 50% reduction in measured flow angle magnitudes along with evidence of fanwise vortex convection when compared to the StreamVane design profile. The upstream measurements also indicated large amounts of secondary flow entered the fan rotor. Measurements immediately downstream of the fan rotor trailing edge demonstrated that the fan processed the distortion and further reduced the intensity of the swirl; however, non-uniform secondary flow persisted at this plane. The downstream measurements confirmed that off-design conditions entered the fan exit guide vanes, likely contributing to cascading performance deficiencies in downstream components and reducing the performance of the propulsor system.

Experimental Investigation of Fan Rotor Response to Inlet Swirl Distortion

Dustin J. Frohnapfel

ABSTRACT FOR PUBLIC RELEASE

Next generation aircraft design focuses on highly integrated airframe/engine architectures that exploit advantages in system level efficiency and performance. One such design concept incorporates boundary layer ingestion to reduce overall aircraft drag, resulting in fuel savings and decreased emissions; however, boundary layer ingestion also creates unique challenges for the turbofan engines operating in less than optimal inlet flow conditions.

One component of the complex distorted inlet flow profiles associated with integrated airframe/engine configurations is the presence of large amounts of secondary flow, or swirl, which affects engine operability, durability, efficiency, and performance. An experiment utilizing a StreamVane swirl distortion generator was designed to measure the effects of swirl on the fan rotor in an operating turbofan research engine. The StreamVane was designed to induce a tailored swirl distortion in the inlet duct which was subsequently ingested by the turbofan engine.

Results from the investigation revealed that the generated swirl profile developed and mixed in the inlet duct upstream of the fan. Measurements immediately upstream of the fan rotor leading edge revealed 50% reduction in measured flow angle magnitudes along with evidence of fanwise vortex convection when compared to the StreamVane design profile. The upstream measurements also indicated large amounts of secondary flow entered the fan rotor. Measurements immediately downstream of the fan rotor trailing edge demonstrated that the fan processed the distortion and further reduced the intensity of the swirl; however, non-uniform secondary flow persisted at this plane. The downstream measurements confirmed that off-design conditions entered the fan exit guide vanes, likely contributing to cascading performance deficiencies in downstream components and reducing the performance of the propulsor system.

Acknowledgements

First and foremost, I would like to acknowledge and graciously thank the National Institute of Aerospace and NASA Langley Research Center for funding this research effort in association with NASA's Environmentally Responsible Aviation Project (NIA cooperative agreement RD-2917), project managers: Fay Collier (LaRC), Hamilton Fernandez (LaRC), Greg Gatlin (LaRC), and Bo Walkley (NIA). In addition, I would also like to thank John Bonet and Ron Kawai of the Boeing Research and Technology Company for providing invaluable information and assistance with BLI inlet flow profiles. The support and attention to this project that all of these research partners provided was truly remarkable.

I would like to thank my thesis committee: Dr. O'Brien, Dr. Lowe, and Dr. Wicks. You genuinely care about each of your students and it shows. Thank you for giving me the opportunity to complete this research effort in your laboratories along with all of the experience and assistance that you could provide. It impressed me that you three gentlemen seemed to always have time to help me while running world-class facilities.

To all of my colleagues at the VT TurboLab: THANK YOU! I cannot possibly express the gratitude that I have for all of the hard work that each of you has contributed for me to complete my research. This is especially true for Justin Bailey, Anthony Ferrar, William Schneck, Chaitanya Halbe, and Gregg Perley. Thank you for both supporting my activities in the lab as well as becoming excellent friends. I expect the friendship and working relationships that we have built will continue throughout our careers and life.

Finally, to my parents, Tim and Penny Frohnapfel, and my sister, Tiffany Frohnapfel, thank you for believing in my wildest dreams and supporting me throughout this endeavor. From phone calls and visits to proofing conference papers, you have given me more than I can ever return. I am proud that the solid foundation of our family and the work ethic that I mimic from each of you allows me to accomplish my goals. I could not have done it without you.

Sincerely,
Dustin J. Frohnapfel

Contents

List of Figures

List of Tables

Nomenclature

	English	
a	Speed of Sound	ft/s
b	Transducer Calibration Intercept	psia
C_d	Discharge Coefficient	
Cp_P	Static Pressure Pressure Coefficient	
Cp_{P0}	Total Pressure Pressure Coefficient	
Cp_α	Radial Flow Angle Pressure Coefficient	
Cp_β	Tangential Flow Angle Pressure Coefficient	
C_r	Radial Velocity	ft/s
C_θ	Tangential Velocity	ft/s
C_z	Axial Velocity	ft/s
$C_{r\theta}$	Two-Dimensional, In-Plane Velocity Magnitude - Polar Coordinates	ft/s
$C_{r\theta z}$	Three-Dimensional Velocity Magnitude - Polar Coordinates	ft/s
D	Drag, Diameter	lb_f,ft
g	Gravitational Acceleration	ft/s^2
h_m	Station Altitude	ft
k_0	Mission Constant without TSFC Effects	
k_T	Mission Constant with TSFC Effects	ft/s
L	Lift	lb_f
M	Mach Number	
m	Transducer Calibration Slope	psia/V
m_1	Initial Mass	lb_m
m_2	Final Mass	lb_m
m_f	Fuel Mass	lb_m
$\dot{m}_a$	Mass Flow Rate (Air)	lb_m/s
$\dot{m}_f$	Mass Flow Rate (Fuel)	lb_m/s
N_1	Fan Speed	RPM
P	Pressure Measurement, Static Pressure	psia,psia
P_0	Total Pressure	psia
$P_{1,2,3,4,5}$	Five Hole Probe Measured Pressures	psia
P_{atm}	Atmospheric Pressure	psia
P_{blm}	Bellmouth Wall Static Pressure	psia
P_{std}	Standard Atmospheric Pressure Reference	psia
P_{svo}	StreamVane Outlet Wall Static Pressure	psia
$\bar{p}$	Four Port Average Five Hole Pressure	psia
R	Gas Constant (Air)	ft lb_f/lb_m °R
r	Radius	ft
r_{tip}	Fan Blade Tip Radius	ft

Re_D	Reynold's Number	
s	Range	ft
T	Thrust, Temperature Measurement, Static Temperature	lb_f,°F,°F
T_0	Total Temperature	°F
T_{atm}	Atmospheric Temperature	°F
T_{std}	Standard Atmospheric Temperature Reference	°F
TSFC	Thrust Specific Fuel Consumption	$(lb_m/s)/lb_f$
u_∞	Freestream Velocity	ft/s
V	Voltage Measurement	V

Greek

α	Radial Flow Angle	deg
β	Tangential Flow Angle	deg
γ	Specific Heat Ratio (Air)	
δ	Standard Pressure Correction Factor	
θ	Standard Temperature Correction Factor, Fan Angle	,deg
μ	Dynamic Viscosity	psia s

Subscript

clean	Indicates Clean Test Result
corr	Indicates Term Corrected to Standard Atmospheric Conditions
distorted	Indicates Distorted Test Result
ideal	Indicates Ideal Term
meas	Indicates Measured Term

Abbreviation

AIP	Aerodynamic Interface Plane
AWOS	Automated Weather Observing System
BLI	Boundary Layer Ingestion
BWB	Blended Wing Body Aircraft
CAD	Computer-Aided Design
CFD	Computational Fluid Dynamics
CMC	Ceramic Matrix Composite
CON	Conventional Tube and Wing Aircraft
ERA	Environmentally Responsible Aviation
FAA	Federal Aviation Administration
FLA	Forward Looking Aft
GTOW	Gross Take Off Weight
HWB	Hybrid Wing Body Aircraft
NASA	National Aeronautics and Space Administration
NIST	National Institute of Standards and Technology
NOAA	National Oceanic and Atmospheric Administration
NWS	National Weather Service
P&WC	Pratt and Whitney Canada
PRSEUS	Pultruded Rod Stitched Efficient Unitized Structure

Chapter 1 – Introduction

1.1 Thesis Overview

Recently, the desirability of highly integrated aircraft which combine multiple subsystems into an optimized flight vehicle has been a focus of the aviation industry. These novel aircraft designs show exceptional efficiency and performance benefits; however, the combination of conventional components into advanced aircraft architectures is known to produce significant design challenges to engineers. A specific example of the challenges of highly integrated aircraft is the existence of non-uniform inlet flow entering the turbofan engine. The research presented in the following thesis is the culmination of a focused investigation into fan rotor response to inlet swirl distortion with the goal of providing useful insight into fan capabilities of processing swirl distortions.

The inlet distortion profile tested in this experiment was created from a computation fluid dynamics model of a conceptual next generation blended wing body aircraft. All experimental testing was conducted using a modified turbofan research engine at the Virginia Tech Turbomachinery and Propulsion Research Laboratory in Blacksburg, VA. A StreamVane swirl distortion device generated the desired swirl pattern in the inlet of the research engine. Flow measurements were taken using a five-hole three-dimensional flow probe at two discrete measurement planes (immediately upstream and immediately downstream of the fan rotor) isolating the fan rotor for analysis.

This chapter (Chapter 1) reviews the current state of the art for distortion testing in aircraft engines as well as places this current research investigation into the context of modern turbofan engine design and airframe integration. Chapter 2 outlines the experimental setup, including pertinent instrumentation and hardware, data acquisition, and data collection schemes. Chapter 3 documents the data reduction process from collected sensor outputs to physical fluid dynamic properties. The resulting flow parameters at the two measurement planes under both clean and distorted test conditions are presented in Chapter 4. Chapter 5 summarizes the significant experimental outcomes as well as reports all conclusions determined from the experimental results.

1.2 Literature Review and Background

1.2.1 Environmentally Responsible Aviation and the Future of Subsonic Transport Aircraft

Modern commercial aircraft design is motivated by requirements to transport passengers and cargo as safely and efficiently as possible. Until now, this has been predominantly accomplished by conventional tube and wing aircraft configurations with a focus on individual component and subsystem improvements to increase overall aircraft efficiency and performance. Recently however, component level efficiencies have begun to approach theoretical maximums and the pace of aircraft system level efficiency advances has diminished. Component design limitations, coupled with ever increasing fuel costs, environmental regulations for fuel-burn and emissions reductions, and the need to reduce flight noise such that more densely populated areas can be serviced have necessitated seeking unconventional, highly integrated aircraft architectures for future designs.

In 2009, NASA initiated the Environmentally Responsible Aviation (ERA) project with the primary goal of maturing novel aircraft technologies into viable solutions for future generation flight vehicles. The specific criteria (summarized in Table 1.1) focus on reductions in aircraft noise, emissions, fuel burn, and runway length. Decreasing noise and runway length will allow operators to service more densely populated areas with lessened restrictions on schedule and flight paths. Reductions in fuel burn and emissions will not only benefit the environment but also save operators in fuel costs.

Table 1.1: NASA N+3 Program Goals

Technology Benefits*	N+1 (2015)	N+2 (2020**)	N+3 (2025)
Noise (cum below Stage 4)	-32 dB	-42 dB	-71 dB
LTO NOx Emissions (below CAEP 6)	-60%	-75%	-80%
Cruise NOx Emissions (rel.to 2005 best in class)	-55%	-70%	-80%
Aircraft Fuel/Energy Consumption (rel. to 2005 best in class)	-33%	-50%	-60%

* Projected benefits once technologies are matured and implemented by industry. Benefits vary by vehicle size and mission: N+1 and N+3 values are referenced to a 737-800 with CFM56-7B engines, N+2 values are referenced to a 777-200 with GE90 engines

** ERA's time phased approach includes advancing "long-pole" technologies to TRL 6 by 2015

*** CO_2 emission benefits dependent on life cycle CO_{2e} per MJ for fuel and/or energy source used

The defined ERA plan focuses on N+2 technologies while promoting further advancement toward N+3 goals. In order to accomplish the stated goals, NASA has outlined several promising enabling technologies (Figure 1.1) for research and development including active and passive flow control, advanced materials, advanced propulsion systems, and highly integrated airframe/engine architectures [1,2].

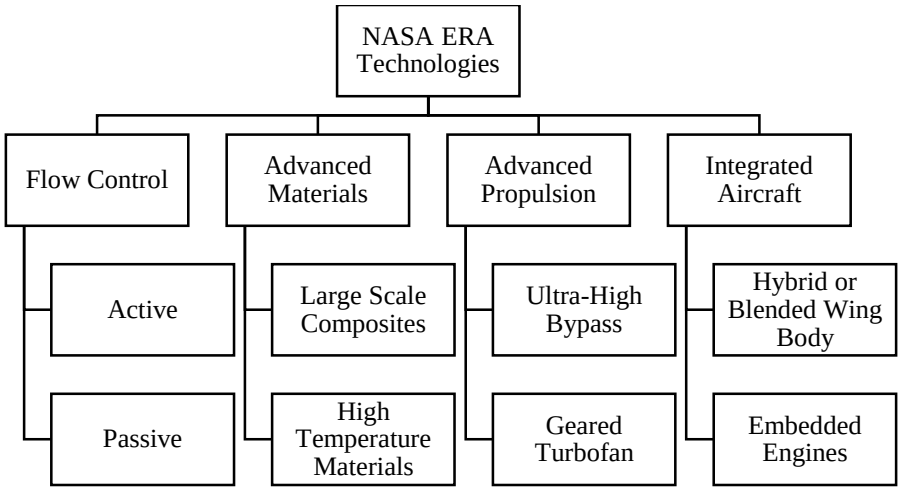

Figure 1.1: NASA ERA Sponsored Enabling Technologies

Flow control can lead to size and weight reductions due to increased performance of smaller control surfaces. This includes active flow control where secondary or external energy is added to a normally independent system to maintain or increase control authority as well as passive flow control where engineered solutions are utilized in primary design of components that offer increased control performance. The ERA project intends to develop both active and passive flow control as a means to reduce drag, fuel burn, and overall aircraft weight. Wind tunnel testing of sweeping jet actuators applied to the trailing edge of the vertical tail of the Boeing 757 ecoDemonstrator have produced 20% increased side force with deflections of the modified rudder. This increase of force could reduce the required size of vertical tail structures which will directly decrease the aerodynamic drag and structural weight of the tail sub-system [3]. In addition to active flow control, passive flow control is being considered to maintain laminar flow over wing surfaces. With the drag advantages of laminar flow well documented [4], it is important to maintain extremely smooth leading edges on aircraft wings. Laminar flow wings can yield up to 30% reductions in fuel burn. A significant cause of degraded surface finishes is the buildup of insect strike residue which can trip flow into the turbulent regime beginning at the leading edge of wings. Laboratory and sub-scale tests utilizing anti-stick coatings and textured finishes have shown mixed benefits in minimizing residue particle height; however additional investigations are ongoing [5,6].

Another enabling technology for the future ERA-type aircraft is large-scale use of advanced composite materials. High strength-to-weight ratios make these materials ideal for replacing conventional aerospace metals in aircraft frames and engines. Citing requirements for large open cabin space in blended wing body aircraft architectures, composite materials can reduce the weight penalty when compared to aluminum frames. One limiting feature of composites is the relatively high cost of fabrication. The PRSEUS project within ERA is testing not only material properties, but also unconventional geometry and highly modular assemblies of composites by combining aircraft skin, stringers, and frame components into single parts. The PRSEUS project aims to maintain high strength-to-weight ratios of composite components, while developing inexpensive means of fabrication [7-10]. Along with structural components, high temperature engine components can be upgraded through the use of ceramic matrix composites (CMCs). CMCs offer advantages in component weight, high temperature survivability, and cost when compared to

exotic materials currently used in hot sections of turbine engines. The use of CMCs allows for greater fuel burn temperature and decreased cooling of hot section components; both aspects directly relate to increased efficiency, decreased fuel burn, and decreased emissions [11,12].

Improvements to conventional propulsion systems, such as ultra-high bypass turbofans, geared turbofans, and open rotor turbofans are under ERA program consideration and testing [1]. Ultra-high bypass and geared turbofan engines take advantage of increasing flow path area rather than flow velocity to increase bypass mass flow rate, and therefore thrust. Reducing fan speed and flow velocity directly relates to decreased jet noise [13]. Open rotor turbofan designs take the ultra-high bypass concept further by eliminating large portions of the engine nacelle. Again, increasing the fan area while decreasing fan speed offers noise reduction and increased propulsive efficiency. Studies conducted on open rotor turbofans have shown fuel burn deceases of 10%, with theoretical improvements up to 25% in optimized designs [11,14]. An advantage of using a conventional turbofan is the ability to embed it subsurface; by definition, the open rotor engines cannot be embedded.

Finally, future aircraft must be designed in highly integrated architectures to fully capitalize on the systems level efficiency gains discussed above. Combining wing and fuselage components in a blended wing body planform yields improvements in lift-to-drag ratio. Because the fuselage and cabin are designed as lifting bodies, less lift is required from the wings which results in size and weight reductions. Decreased weight enables shorter takeoff and landing lengths, minimizing the ground noise levels near airports. Furthermore, installing engines near the aircraft skin or embedding engines subsurface reduces form drag on the propulsion subsystem and enables the concept of boundary layer ingestion for additional efficiency improvements [1,7,15].

1.2.2 Boundary Layer Ingesting Aircraft Configurations

Future aircraft concepts must combine enabling technologies into a highly integrated vehicle to provide the cumulative benefit of each component while solving complicated systems level challenges. With the guidance of NASA and the ERA program, several concept aircraft that radically alter conventional design methodology are being engineered and tested. These novel architectures build on the entire history of aviation with several drastically advanced features such as extra wide and blended wing bodies and aft mounted, embedded engines [15,16]. Examples include the MIT D-8 “Double Bubble” and the Boeing N2A-EXTE “Hybrid Wing Body”. The MIT-D8 “Double Bubble” maintains a relatively conventional tube and wing design with the difference being the extra wide, or double wide, fuselage [17,18]. The Boeing N2A-EXTE “Hybrid Wing Body” incorporates the fuselage and wing into a highly integrated, blended design which utilizes the entire aircraft as a lifting body [19-21].

Both concept designs take advantage of large fuselage body area to aid with overall lift of the vehicle. Additionally, both aircraft have aft mounted engines that are located close to the surface of the fuselage. This second feature has garnered much interest in the propulsion research industry. When mounted near the surface of the aircraft, the engines operate in the low speed boundary layer flow region created by viscous effects of flow over the aircraft surface. Commonly referred to as Boundary Layer Ingestion (BLI), this method of integrating the propulsion systems and lifting

systems offers several unique advantages with reductions in overall aircraft drag, fuel burn, and noise when compared to conventional podded, wing mounted engines. Figure 1.2 illustrates the reduction in frontal area and boundary layer thickness of a BLI engine installation compared to a pylon mounted engine installation. Both ram drag and boundary layer parasitic drag are reduced in the BLI arrangement.

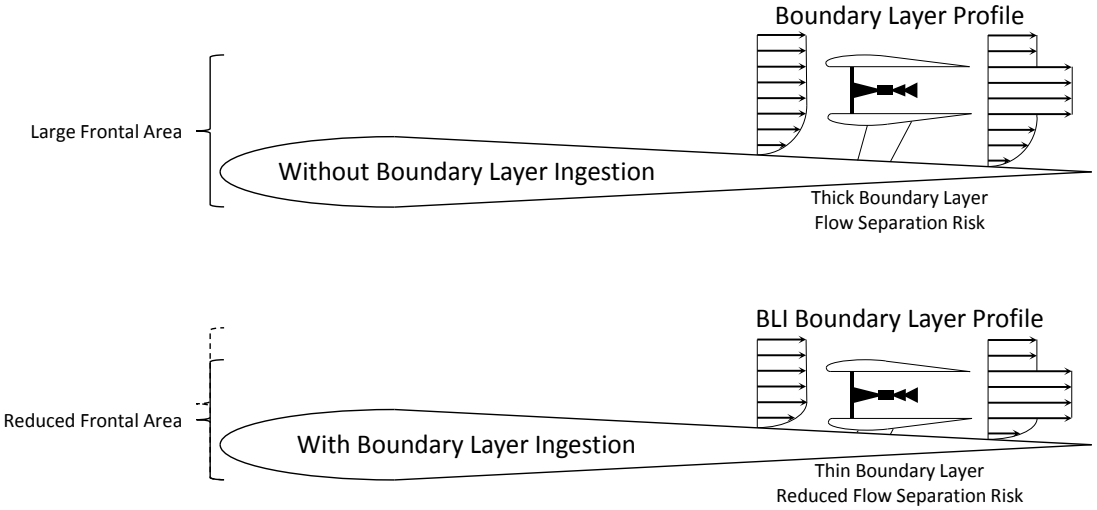

Figure 1.2: Schematic of Boundary Layer Ingestion Benefits

While BLI offers many advantages, a few difficulties remain with successfully integrating current turbofan engine technology into complex aircraft architectures. Because the flow properties vary within the boundary layer, the engines experience severe non-uniformities in the inlet flow which can lead to significantly off-design fan inlet conditions. The flow distortions associated with BLI pose interesting topics in aerodynamics, aeromechanics, performance, and efficiency which require further propulsion research and engineering [13,22-26]

1.2.3 Opportunities Associated with BLI-Type Aircraft

Highly integrated, blended wing body aircraft architectures, such as the Boeing N2A-EXTE utilize the entire aircraft as a lifting body, significantly increasing lift-to-drag ratio [7,23,27]. Beginning with the Brequet range equation (Eq. 1.1) a high level case study was performed to demonstrate the fuel savings benefit of increasing lift-to-drag ratio. The initial assumptions associated with this case study included the following: engine performance is not affected by installation type (conventional or blended wing body), fuel mass flow rates are negligible compared to air mass flow rates, and the exhaust nozzle is optimized.

$$s = \frac{L}{D}\frac{T}{\dot{m}_f}\frac{u_\infty}{g}\ln\left(\frac{m_1}{m_2}\right) \tag{1.1}$$

Substituting the equation for thrust specific fuel consumption, or TSFC, (Eq. 1.2) into Equation 1.1 yields Equation 1.3.

$$TSFC = \frac{\dot{m}_f}{T} \tag{1.2}$$

$$s = \frac{L}{D}\frac{1}{TSFC}\frac{u_\infty}{g}\ln(\frac{m_1}{m_2}) \tag{1.3}$$

Again, assuming engine performance is unchanged with respect to installation architecture and the two competing architectures are flying identical missions, Equation 1.3 can be recast with the addition of a mission constant (Eq. 1.4) into Equation 1.5.

$$k_0 = s(TSFC)\left(\frac{g}{u_\infty}\right) \tag{1.4}$$

$$k_0 = \frac{L}{D}\ln(\frac{m_1}{m_2}) \tag{1.5}$$

Additionally, assuming the difference in mass throughout the flight is only attributable to fuel burned (Eq. 1.6), Equation 1.5 is rewritten as Equation 1.7.

$$m_2 = m_1 - m_f \tag{1.6}$$

$$k_0 = \frac{L}{D}\ln\left(\frac{m_1}{m_1 - m_f}\right) = -\frac{L}{D}\ln\left(\frac{m_1 - m_f}{m_1}\right) = -\frac{L}{D}\ln\left(1 - \frac{m_f}{m_1}\right) \tag{1.7}$$

Finally, equating the mission constant for a conventional tube and wing aircraft with the mission constant for a blended wing body aircraft (Eq. 1.8) and assuming that the total takeoff weight is approximately equal (reduced fuel weight offsets additional structural weight in the blended wing body aircraft) (Eq. 1.9), the relationship between the architectures can be written as Equation 1.10.

$$(k_0)_{CON} = (k_0)_{BWB} \tag{1.8}$$

$$(m_1)_{CON} = (m_1)_{BWB} = m_1 \tag{1.9}$$

$$\left(-\frac{L}{D}\ln\left(1 - \frac{m_f}{m_1}\right)\right)_{CON} = \left(-\frac{L}{D}\ln\left(1 - \frac{m_f}{m_1}\right)\right)_{BWB} \tag{1.10}$$

Rearranging Equation 1.10 shows the relationship between mass of fuel and lift-to-drag ratio in Equation 1.11.

$$\left(m_f\right)_{BWB} = m_1\left[1 - \left(1 - \frac{\left(m_f\right)_{CON}}{m_1}\right)^{\frac{\left(\frac{L}{D}\right)_{CON}}{\left(\frac{L}{D}\right)_{BWB}}}\right] \tag{1.11}$$

From the simplified equation, a preliminary design model (Figure 1.3) was constructed to illustrate the benefits of high lift-to-drag ratio. The model shows that as the lift-to-drag ratio increases compared to conventional values while holding other terms constant, the required fuel mass for the mission decreases; as the fuel mass percentage of gross takeoff weight increases, these benefits are reduced.

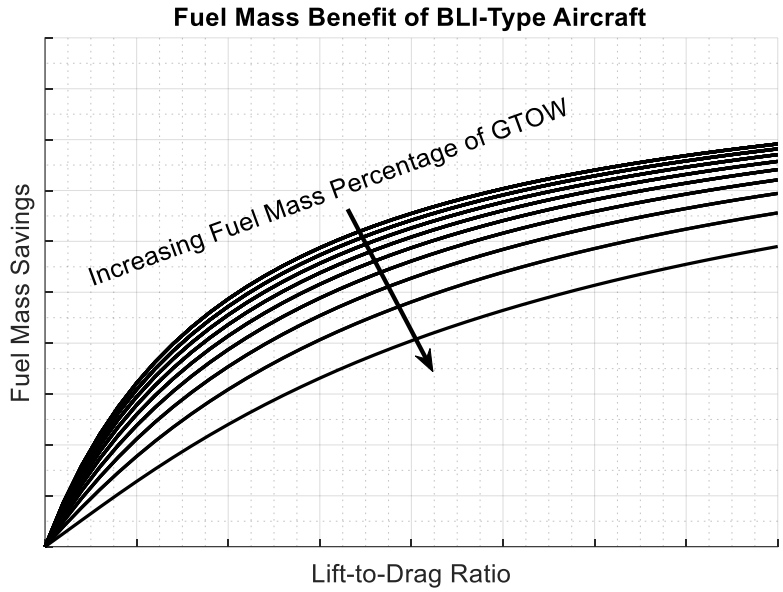

Figure 1.3: Fuel Mass Benefit of BLI-Type Aircraft

While this highly idealized model assumes that the performance of the propulsion system remains unaffected by the installation architecture, it clearly illustrates the benefits of optimized blended wing body aircraft designs.

To further exploit the benefits of highly integrated blended wing body designs, engines can be embedded for boundary layer ingestion (BLI). With the goals of the ERA program in mind, BLI aircraft designs can be optimized to reduce fuel consumption (and associated emissions) and aircraft noise, making BLI an appealing concept for the future of commercial aviation. By ingesting and re-energizing the relatively low speed flow in the boundary layer on the top surface of the lifting body, boundary layer parasitic drag is reduced and flow attachment is maintained at greater angles of attack. Not only are the losses associated with the boundary layer drag on the aircraft reduced, but engine/airframe architecture can be optimized to decrease overall aircraft drag and weight [23,28].

This reduction of drag and weight is directly reflected as a reduction in fuel burn and therefore reduced emissions. Previous studies of blended wing body aircraft configurations concluded that fuel burn could be additionally decreased by more than 16% through the use of optimized BLI engine design when compared to non-BLI designs flying identical missions. All of these features validate BLI as an appealing concept for the future of commercial aviation; however, the non-uniform flow associated with ingesting the boundary layer can produce design challenges for propulsion engineers [13,23,25,28-30].

1.2.4 Challenges Associated with BLI-Type Aircraft

While significant improvements in system level aircraft efficiency can be achieved through the use of highly integrated aircraft configurations, design and optimization of subsystems remains important. The propulsion system is particularly susceptible to performance losses when considering near-surface mounted or embedded engines that ingest non-uniform boundary layer flow. Engine/airframe integration poses considerable challenges in inlet design. Due to non-uniform boundary layer flow entering the inlet duct, the fan rotor of a BLI engine experiences drastically different conditions when compared to conventional pylon installation. Without mitigation efforts, the inlet flow distortions associated with BLI applications produce engine performance reductions. [29,31,32]

Studies of inlet flow distortion have concluded that propulsive losses are attributable to the engine continuously operating in a field of varying inlet flow conditions. The fan cycles in and out of highly distorted regions in the flow which create local depressions in fan efficiency [33,34] as well as contribute to dynamic aeromechanical loads and stresses [35]. A previous investigation concluded that a severe inlet total pressure distortion caused an increase in engine TSFC of approximately 15% [31]. Additionally, the distortions create aerodynamic problems such as reduction of fan stall margin [36], production of secondary flow fields, thrust losses, and efficiency degradation [34].

By revisiting the high level systems study previously discussed, Equation 1.11 can be updated with the effect of TSFC beginning with Equation 1.3.

$$s = \frac{L}{D}\frac{1}{TSFC}\frac{u_\infty}{g}\ln(\frac{m_1}{m_2}) \tag{1.3}$$

From previous research, it can no longer be assumed that engine performance is unchanged with respect to installation architecture when incorporating BLI into the design. Assuming the two competing architectures are flying identical missions, Equation 1.3 can be recast with the addition of a new mission constant (Eq. 1.12) into Equation 1.13.

$$k_T = s\left(\frac{g}{u_\infty}\right) \tag{1.12}$$

$$k_T = \frac{L}{D}\frac{1}{TSFC}\ln(\frac{m_1}{m_2}) \tag{1.13}$$

Similar to before, the difference in mass throughout the flight is assumed to be only attributable to fuel burned (Eq. 1.6). Equation 1.13 is rewritten as Equation 1.14.

$$k_T = -\frac{L}{D}\frac{1}{TSFC}\ln\left(1-\frac{m_f}{m_1}\right) \tag{1.14}$$

Finally, equating the mission constant for a conventional tube and wing aircraft with the mission constant for a blended wing body aircraft (Eq. 1.15) and assuming that the total takeoff weight is

approximately equal (reduced fuel weight offsets additional structural weight in the blended wing body aircraft) (Eq. 1.9), the relationship between the architectures is updated in Equation 1.16.

$$(k_T)_{CON} = (k_T)_{BWB} \tag{1.15}$$

$$\left(-\frac{L}{D}\frac{1}{TSFC}\ln\left(1-\frac{m_f}{m_1}\right)\right)_{CON} = \left(-\frac{L}{D}\frac{1}{TSFC}\ln\left(1-\frac{m_f}{m_1}\right)\right)_{BWB} \tag{1.16}$$

Rearranging Equation 1.16 shows the relationship between mass of fuel, lift-to-drag ratio, and TSFC in Equation 1.17.

$$\left(m_f\right)_{BWB} = m_1\left[1-\left(1-\frac{\left(m_f\right)_{CON}}{m_1}\right)^{\frac{\left(\frac{L}{D}\frac{1}{TSFC}\right)_{CON}}{\left(\frac{L}{D}\frac{1}{TSFC}\right)_{BWB}}}\right] \tag{1.17}$$

The updated model based on Equation 1.17 is illustrated in Figure 1.4. With the addition of BLI associated TSFC penalties, the model shows that additional lift-to-drag ratio margin must be achieved to offset propulsive efficiency losses. This fact demonstrates the total system interdependencies that must be optimized to benefit from BLI propulsion architectures.

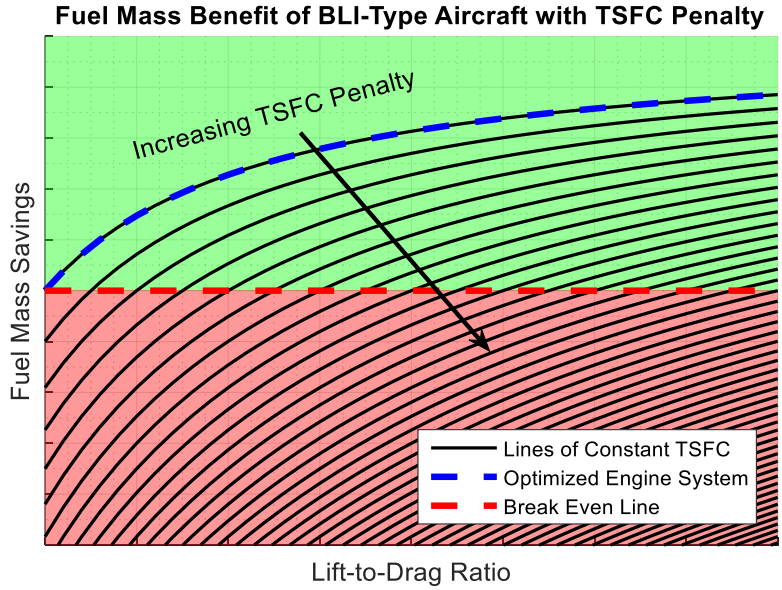

Figure 1.4: Fuel Mass Benefit of BLI-Type Aircraft with TSFC Penalty

Investigations into BLI propulsion have determined complex, coupled total pressure and swirl distortions generated by the airframe geometry and engine/airframe integration are two primary sources of losses in engine performance. Total pressure distortions typically arise from low energy boundary layer flow ingestion and flow separation within complex inlet duct geometry. Circumferential and radial pressure gradients then interact with the fan rotor causing changes in the inlet total pressure field resulting in off-design conditions entering the engine [30]. Substantial

experimental research has previously concluded that inlet total pressure distortions typically contribute to degradations in fan pressure ratio and therefore fan efficiency [31-33,37]. Inlet swirl distortions in highly integrated engine/airframe architectures typically arise from upstream wake shedding, secondary flow mixing, and aggressive flight maneuvers [30]. Until now, inlet swirl distortion investigations have been limited to computational models and isolated fan component tests [34,38,39]. New technology, such as the StreamVane utilized in this paper, has enabled engineers to study the effects of inlet swirl distortion in full-scale, operational turbofan engines.

1.2.5 Inlet Swirl Distortion

Inlet swirl distortion, also known as inlet secondary flow distortion, is a condition in which the velocity profile entering an engine contains a significant amount of vorticity and non-axial flow. Historically, this type of distortion has been less of a concern than inlet total pressure distortions. Citing relatively simple inlet duct geometry, robust distortion tolerant fan designs, and the use of inlet guide vanes, swirl distortion was considered mitigated in early design phases. However, the advent of high-performance military aircraft with complex engine inlet ducts and ultra-high bypass turbofan engines entering the commercial aviation market has since shown increased prominence of inlet swirl distortions on the performance and durability of aircraft propulsion systems.

The SAE International S-16 Turbine Engine Inlet Flow Distortion Committee characterizes and defines swirl according to four categories: bulk swirl, tightly-wound vortices, paired swirl, and cross-flow swirl. Bulk swirl (Figure 1.5a) is a large scale, global rotation of the flow field in a single direction and is typically caused by large aircraft structures and inlet duct geometry upstream of the engine. Tightly-wound vortices (Figure 1.5b) are small scale (approximately 20% flow area), high intensity flow regions where the local flow velocity rapidly and continuously changes direction. Tightly-wound vortices are typically caused by small aircraft structures upstream of the engine inlet, inlet lip separation, and ground vortices. Paired swirl (Figure 1.5c), consists of a set of contra-rotating vortices and is commonly associated with flow mixing in the presence of low pressure regions in serpentine inlet ducts. The final type of inlet swirl is cross-flow swirl (Figure 1.5d). This swirl profile is caused by external flow crossing the inlet at an angle normal to axial direction and is common in fans with short inlet ducts in high crosswind conditions.

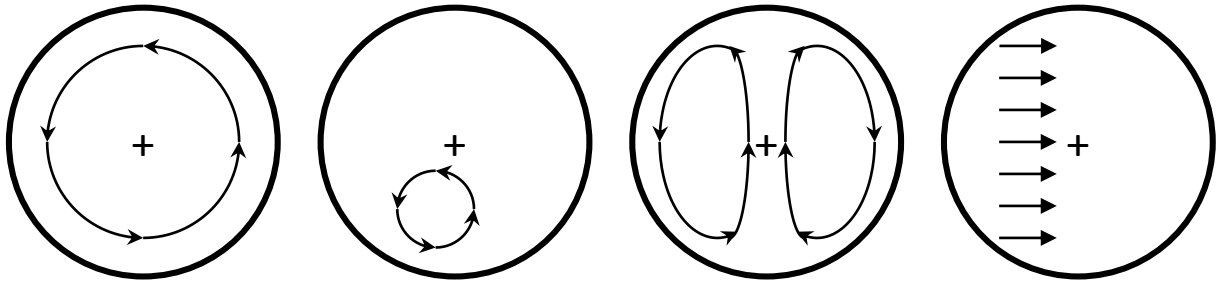

Figure 1.5: Swirl Distortion Categories
Bulk Swirl (a), Tightly-Wound Vortex (b), Paired Swirl (c), and Cross-Flow Swirl (d)

All categories of inlet swirl are classified in terms of swirl descriptors: sector swirl, swirl intensity, swirl directivity, and swirl pairs. The use of swirl descriptors generalizes the extent (scale), intensity (strength), direction (co-rotating or counter-rotating with respect to fanwise rotation), and number of vortices in a flow profile [40].

Investigations of inlet swirl distortion have been limited when compared to the inlet total pressure distortion counterpart. This is primarily due to the difficulty associated with generating tailored swirl profiles without disturbing other properties of the flow field [41]. In general, experiments of generic swirl have determined this type of inlet distortion contributes to performance losses in the fan system creating a cascading effect in downstream engine stages. The direction of the swirl has a significant effect on the fan rotor loading. Co-rotating swirl reduces the blade incidence angle contributing to reduced rotor loading; whereas, counter-rotating swirl increases the blade incidence angle contributing to increased rotor loading [29].

Computational investigations of inlet swirl distortion have been focused on fan pressure ratio, temperature ratio, and efficiency. These investigations concluded that co-rotating swirl caused reductions in fan pressure ratio and fan temperature ratio, and counter-rotating swirl caused opposite effects when compared to nominal axial inlet flow. Both results indicate reductions in adiabatic efficiency of the fan stage [38,39,42]. Additionally, the effect of multiple ingested vortices led to significant fan pressure ratio reductions with substantial effect on the fan stage stall margin [39].

The validation of the computational models in these cases was limited due to scarce experimental data available for comparison; however, an experimental investigation was conducted using a BLI inlet profile in a simulated low-speed, single-stage fan apparatus. The resulting measured flow parameters indicated good agreement with computational data trends, and the BLI inlet profile contributed to approximately 2% isentropic fan efficiency losses [34]. Due to several design differences between the simulated low-speed, single-stage fan apparatus and an actual turbofan engine, the experiment was only representative of swirl effects on turbofan rotors. To study realistic turbofan conditions, a distortion device, known as a StreamVane has recently been developed to model complex inlet swirl distortions in operational turbofan engines [43]. This distortion device, which models realistic flow profiles derived from conceptual aircraft, is inserted into the inlet duct of a turbofan engine where flow measurements indicating fan/distortion interactions are taken. The results have shown that as the distortion profile progresses streamwise toward the fan, the swirl intensity decreases and defined vortex features tend to convect in the fanwise direction [44,45].

It is clear that swirl distortion contributes to considerable losses in performance and efficiency of the propulsion system; however, at the aircraft systems level perspective, substantial performance and efficiency gains can offset subsystem losses. The improvements in drag, noise, fuel burn, and emissions continue to suggest BLI engine architectures as a leading concept for future aircraft designs. Furthermore, with focused research in inlet flow distortions, propulsion systems will advance toward distortion tolerant components and the temporary negative performance impacts of distortion will be mitigated.

1.3 Research Motivation

As a contribution to the NASA ERA project, the current research investigation was conducted to experimentally demonstrate the interactions of inlet swirl on an operational turbofan engine in support of the development of highly integrated engine/airframe aircraft architectures. Previously, the study of complex inlet distortion profiles was limited to computational models which relied on generic experimental swirl distortion data for validation. The requirement for enhanced experimental verification methods that examine realistic inlet conditions associated with a specific aircraft design motivated this research investigation.

Additionally, the idea of highly integrated engine installations requires understanding of the propulsion system response to inlet swirl distortions. The experimental data collected here characterizes the inlet and outlet conditions of a fan experiencing a severe inlet swirl distortion associated with a concept BLI-type aircraft. The resulting parameters assist in understanding performance, efficiency, and durability of the turbofan engine and designate focus areas of future fan rotor designs. Experiments of this type are vital toward mitigating negative effects of integrated propulsion and serve as additional sources of information for the task of designing distortion tolerant engine components.

Chapter 2 – Experimental Methods

2.1 Introduction to the Experiment

In order to characterize the flow parameters associated with a severe inlet swirl distortion, a series of turbofan engine ground tests were designed and conducted at the Virginia Tech Turbomachinery and Propulsion Research Laboratory. A StreamVane swirl distortion generator was inserted into the inlet duct of a modified Pratt & Whitney Canada JT15D-1 turbofan engine. This distortion generator simulated the engine inlet swirl profile produced by a conceptual, future generation blended wing body BLI-type aircraft designed by Boeing Research and Technology as part of the NASA ERA project.

Flow measurements were taken at the fan rotor inlet plane (Station 1.0) and fan rotor outlet plane (Station 1.5) to isolate and determine the response of the fan rotor to the selected swirl distortion profile. Along with distorted test measurements, clean test measurements were collected after removing the StreamVane from the engine inlet duct. The calculated deviations from clean test results indicate changes in fan rotor performance and illustrate the effects of swirl distortion on the propulsion system.

2.2 The StreamVane Swirl Distortion Generator

The StreamVane swirl distortion generator used in this experiment was modeled to create the engine inlet swirl profile associated with a near surface mounted engine installation of a conceptual blended wing body BLI-type aircraft configuration. Additionally, the profile was considered by designers as a worst-case-scenario associated with large amounts of boundary layer ingestion and multiple ingested leading edge vortices generated by aggressive aircraft maneuvers. The profile was derived from wind tunnel test data [20] and CFD analysis of a scale model aircraft.

The wind tunnel tests illustrated the flow field around the airframe; however, due to the use of flow-through nacelles in the scale model, engine response to the simulated flow field was not measured. Experimental flow visualization results showed strong vortices generated by the leading edge of the blended wing body aircraft being ingested into the engine inlets. While the experimental data provided limited information about the response of the propulsion system, it served as realistic inputs for numerical models which included more realistic engine architectures.

CFD analysis completed the preliminary research effort by calculating the inlet flow profile with simulated engines installed in the model. The two-dimensional velocity streamlines and swirl angles at the engine aerodynamic interface plane were then extracted from the CFD results (Figure 2.1). In the figure, the radial and tangential flow angles indicated high levels of off-axis inlet flow, while the normalized in-plane velocity profile showed as much as 60% of the local velocity magnitude was off-axis of the engine centerline.

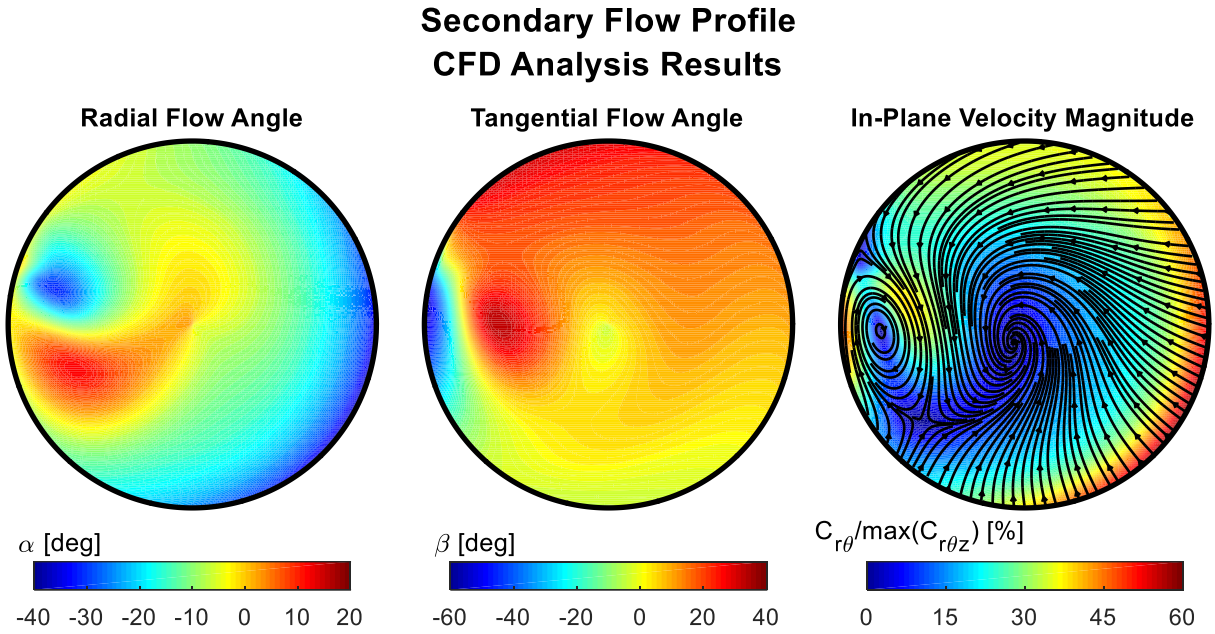

Figure 2.1: Two-Dimensional Swirl Distortion Profile extracted from CFD Results

According to the categories defined by the S-16 Committee, the inlet flow profile contained two primary swirl structures – a co-rotating (fanwise) bulk swirl distortion and a counter-rotating (anti-fanwise) tightly-wound vortex centered at approximately 80% radius from centerline and 90° anti-clockwise from top-dead-center.

This velocity profile was used as the input to the Virginia Tech StreamVane Method which generated a three-dimensional swirl distortion device [43,44]. The StreamVane design technique positioned stationary turning vanes in a coordinated pattern that manipulate the uniform input flow into the desired swirled output flow. A computational routine calculated positon, spacing, and angles of the turning vanes and output a three-dimensional coordinate array of the StreamVane device. This three-dimensional script was then read by a CAD program where additional features such as a shroud and mounting flange were added. Due to the complex geometry associated with the StreamVane, the finalized CAD model was fabricated to engine-scale using additive manufacturing. The finished StreamVane (Figure 2.2) was then mounted in the engine inlet for distortion testing.

Figure 2.2: Engine-Scale StreamVane Swirl Distortion Generator

2.3 The Turbofan Engine Research Platform

2.3.1 Overview

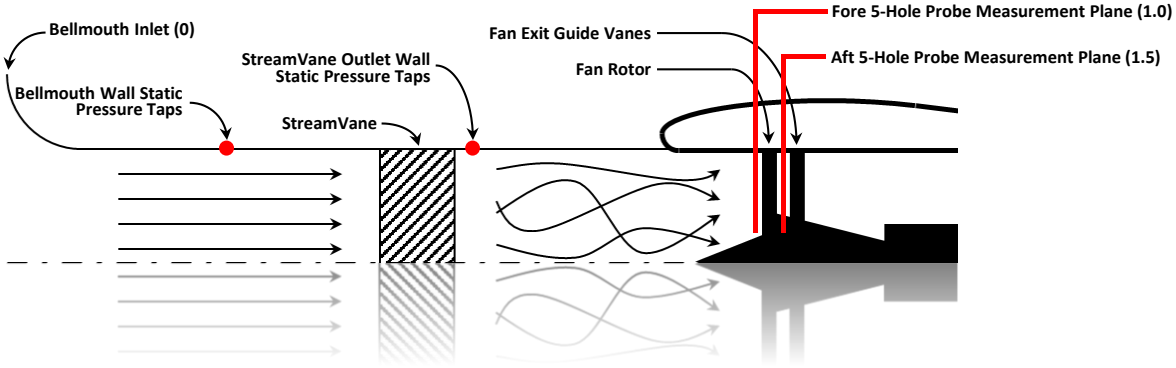

Figure 2.3: Turbofan Engine Research Platform Schematic

Experimental swirl distortion ground tests were conducted using a modified Pratt & Whitney Canada JT15D-1 turbofan engine research platform at the Virginia Tech Turbomachinery and Propulsion Research Laboratory. A schematic of the engine research platform is shown in Figure 2.3. Atmospheric air entered a cylindrical inlet duct via a bellmouth inlet (Station 0). The flow then encountered the StreamVane test article where swirl was introduced. The swirl profile was allowed to develop in additional cylindrical duct sections before being ingested by the engine. This development length was intended to reduce small-scale wake effects in the flow field produced by the turning vanes of the StreamVane device. Fan case penetrations both fore (Station 1.0) and aft (Station 1.5) of the fan rotor permitted flow measurements to be taken with a traversing five-hole three-dimensional flow probe. By circumferentially rotating the StreamVane distortion device and radially traversing the five-hole three-dimensional flow probe, flow properties were

measured in the annular flow path at the two planes. Additionally, wall static pressure was measured at the bellmouth inlet and the StreamVane outlet planes.

2.3.2 Local Atmospheric Conditions

Local atmospheric pressure and temperature were measured and recorded every twenty minutes using a weather station at the Virginia Tech Montgomery Executive Airport. Located less than one quarter mile away from the engine test cell, the National Institute of Standards and Technology (NIST) traceable instrumentation serves as a Federal Aviation Administration (FAA) certified Automated Weather Observing System (AWOS) weather station capable of highly accurate atmospheric condition monitoring. These atmospheric data were available from the National Weather Service (NWS) in the form of historical weather data tables which were accessed posttest. The historical temperature data was recorded at local conditions; however, the historical atmospheric pressure data was corrected to standard atmospheric conditions. For congruency with measured experimental data, the atmospheric pressure data must first be uncorrected to local conditions according to Equation 2.1 (supplied by National Oceanic and Atmospheric Administration, NOAA), where the station altitude is in meters.

$$P_{atm} = P_{atm_{cor}} \left(\frac{288 - 0.0065 * h_m}{288} \right)^{5.2561} \tag{2.1}$$

Figure 2.4 shows example daily trends for the local atmospheric conditions during a typical test day. The experimental atmospheric pressure and temperature were interpolated from these trends based on the timestamp of the experimental data point.

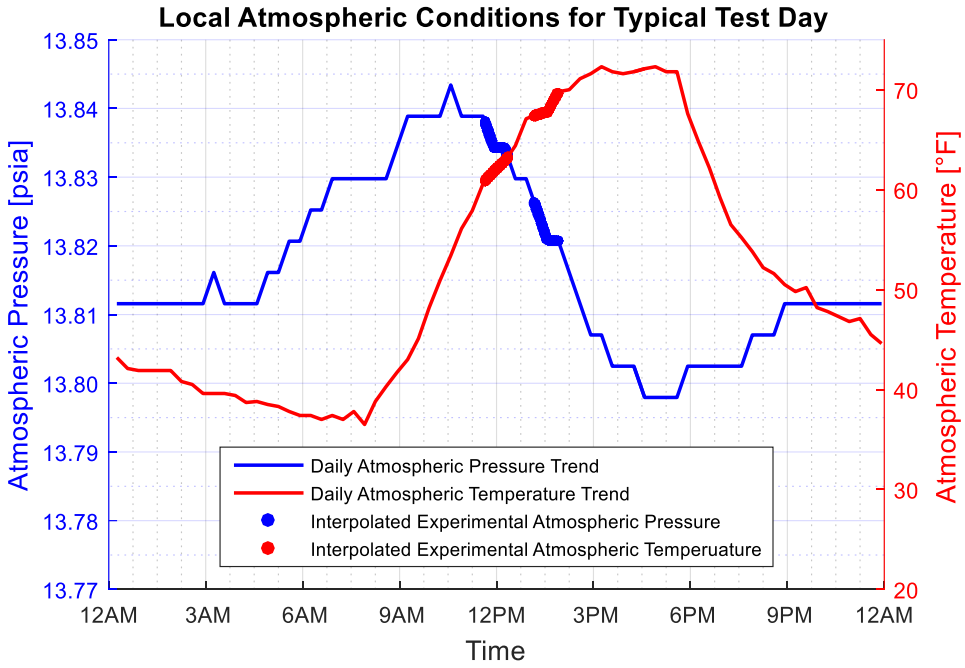

Figure 2.4: Local Atmospheric Conditions with Interpolated Experimental Data

From the plot, the values vary slightly during data collection periods. This variation was later removed from experimental data by using correction factors that related all collected data back to standard atmospheric conditions. The correction factors for pressure and temperature are shown in Equations 2.2 and 2.3 respectively.

$$\delta = \frac{P_{atm}}{P_{std}} \; where \; P_{std} = 14.696 \; psia \tag{2.2}$$

$$\theta = \frac{T_{atm}}{T_{std}} \; where \; T_{std} = 59 \; °F \tag{2.3}$$

2.3.3 Mass Flow Rate Calibrated Bellmouth Inlet

Air at atmospheric conditions entered an open bellmouth inlet adapter approximately five and one half fan diameters upstream of the fan rotor inlet plane. The smooth walled bellmouth inlet was designed according to ASME standard practices [46]. The bellmouth assisted in conditioning the flow axially in the inlet duct and allowed for inlet mass flow rate measurements. Four wall static pressure taps were located one and one half fan diameters downstream of the inlet plane, as indicated in Figure 2.3. The wall static pressure taps were installed every 90° circumferentially, beginning at 45° fanwise (anti-clockwise) from top-dead-center. The static pressures were measured with Omega PX139-005D4V pressure transducers, specifications of which are summarized in Table 2.1.

Table 2.1: Omega PX139-005D4V Static Pressure Transducer Specifications

Full Scale Range	±5 psig
Excitation Voltage	5 Vdc @ 2mA
Output Voltage	0.25–4.25 Vdc
Span	4±0.1 Vdc
Linearity and Hysteresis	±0.1% Full Scale
Repeatability	±0.3% Full Scale
Zero Balance	2.25±0.1 Vdc
Compensated Temperature Range	32-122°F
Zero Temperature Effects	±0.5% Full Scale
Span Temperature Effects	±0.5% Full Scale
Proof Pressure	>3x Full Scale Pressure
Burst Pressure	>5x Full Scale Pressure

The static pressures were then correlated to calibration data to empirically determine the mass flow rate of air entering the engine. The complete derivation of the mass flow rate can be found in the next chapter.

2.3.4 StreamVane Rotator

Continuing downstream, the flow encountered the inlet of the StreamVane swirl distortion device at approximately two fan diameters upstream of the fan rotor, one fan diameter upstream of the

defined aerodynamic interface plane (AIP). The StreamVane was installed in a rotating mount and encased in an airtight housing (Figure 2.5). Rather than using multiple five-hole flow probes or moving a single five-hole flow probe to multiple circumferential locations around the fan case, the entire flow profile rotated incrementally which enabled the use of a single five-hole flow probe and a single fan case penetration at each axial measurement plane. This not only simplified the instrumentation and reduced the number of probes and transducers, but also preserved the structural integrity of the fan case by limiting the total number of probe penetrations to two.

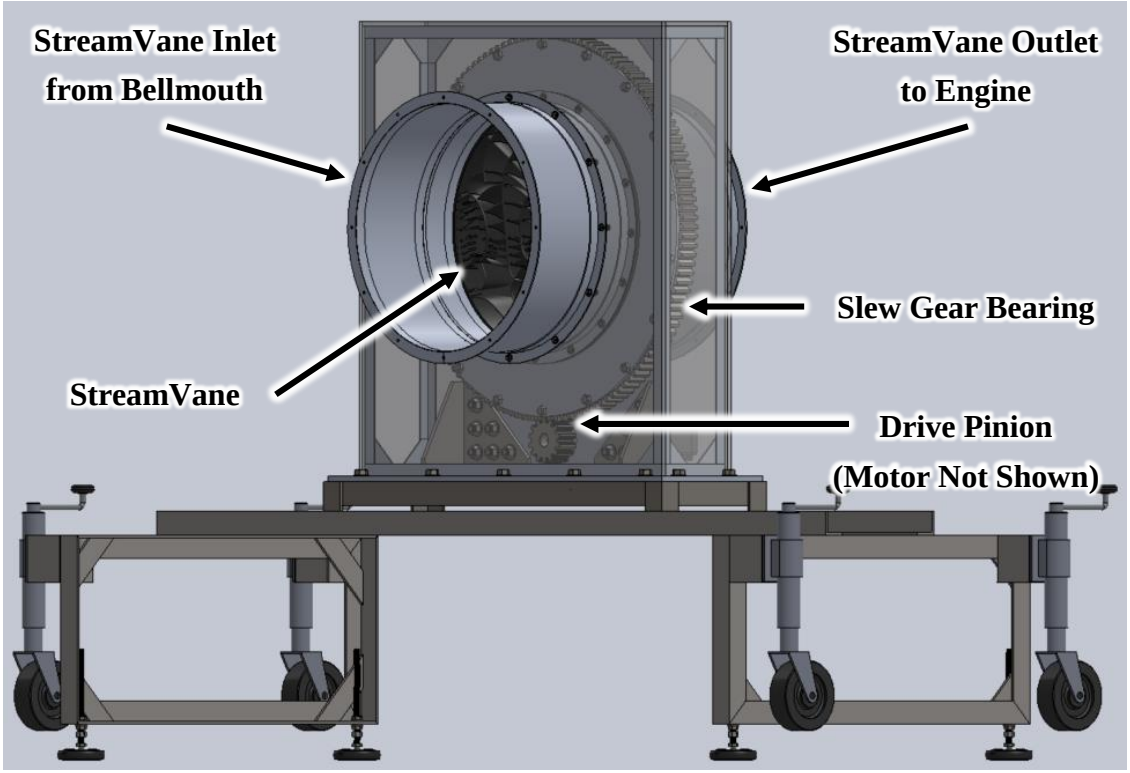

Figure 2.5: StreamVane Rotator

A stepper motor (Anaheim Automation – 34Y314S-LW8) connected to a torque multiplying planetary gear box (Anaheim Automation – GBPH-0902-NS-050-AA341-625) rotated a pinion gear (Rotek – P4-3.5D2) which in turn rotated the large slip ring geared bearing (Rotek – L629E9Z(P)). By micro-stepping the stepper motor, the rotational accuracy of the gear system was ±0.001°. Additionally, by rotating in a single direction, gear backlash was eliminated.

Four wall static pressure taps were located on the discharge flange of the StreamVane rotator near the outlet plane of the StreamVane, as indicated in Figure 2.3. The wall static pressure taps were installed circumferentially at every 90°, beginning at 45° fanwise from top-dead-center. Each static pressure was measured with a dedicated Omega PX139-005D4V pressure transducer, specifications of which are summarized in Table 2.1. Tunnel sections coupled the discharge flange of the StreamVane rotator to the fan case of the engine and allowed for swirl development and dissipation of small scale wake effects before the swirl profile interacted with the fan rotor.

2.3.5 Modified Turbofan Engine

All distortion tests were conducted using a modified Pratt & Whitney Canada JT15D-1 turbofan engine. Several important design parameters of the engine are summarized in Table 2.2. The two-stage axial turbine of the 2,200 pound thrust turbofan engine drives a centrifugal core compressor and a twenty-one inch fan. The fan rotor of this particular engine model includes two design features that made it ideal for severe inlet distortion testing – a mid-span shroud and a part-span stiffener. These features enhance the strength and durability of the fan blades, reducing the risk of aeromechanical failure associated with dynamic loading as the fan cycled through the distortion profile. Important fan geometry data are summarized in Table 2.3.

Table 2.2: P&WC JT15D-1 Engine Parameters at Design (100%) Corrected Fan Speed

Fan Speed	16000 RPM
Fan Blade Tip Speed	1466 ft/s
Mass Flow Rate	73.10 lbm/s
Fan Pressure Ratio	1.5
Bypass Ratio	3.3
Thrust	2200 lb

Table 2.3: P&WC JT15D-1 Fan Geometry Data

Fan Diameter	21.000 in
Number of Blades	28
Blade Root Chord Length	2.436 in
Blade Tip Chord Length	3.047 in
Blade Root Radius	4.250 in (40% Blade Tip Radius)
Blade Mid-Span Shroud Radius	7.750 in (74% Blade Tip Radius)
Blade Part-Span Stiffener Radius	9.190 in (88% Blade Tip Radius)
Blade Tip Radius	10.500 in (100% Blade Tip Radius)
Core/Bypass Splitter Case Radius	6.500 in (62% Blade Tip Radius)

The fan speed throughout testing was measured using a Monarch ROS-W Remote Optical Sensor (Table 2.4) mounted in the tunnel wall near the fan inlet plane. The sensor emits light from an LED source, and detects a reflection from a polished once-per-rev target attached to the fan shaft. The time difference between two successive pulses yields an accurate fan speed measurement. The output voltage of the sensor was processed real-time to produce a fan speed in RPM which was recorded by the data acquisition system.

Table 2.4: Monarch ROS-W Remote Optical Sensor Specifications

Speed Range	1-250000 RPM
Excitation Voltage	3-15 Vdc @ 40 mA
Output Voltage	Negative Pulse Input Voltage to Zero
Illumination	Visible Red LED
Operating Temperature	14-158 °F
Operating Range	0-36 in and 45° from Target

2.3.6 Five-Hole Three-Dimensional Flow Probe and Radial Traverse

Flow measurements were taken at two axial planes in the turbofan engine research platform using a five-hole three-dimensional flow probe (United Sensor – DAT-187-35-J-33-CD-K-LW). Illustrated in Figure 2.6, the 3/16 inch diameter probe features a prism-style five-hole pressure port arrangement with a shielded thermocouple protruding from the probe tip. The five simultaneously measured pressures were normalized into four pressure coefficients [47] and correlated to known values from a calibration procedure [Appendix A]. The flow parameters directly measured (via correlation to calibration data) were the radial flow angle, tangential flow angle, total pressure, static pressure, and total temperature.

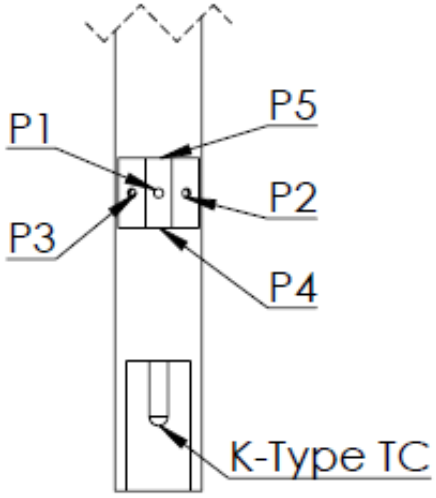

Figure 2.6: Five-Hole Three-Dimensional Flow Probe Schematic

The five pressures acting on the five-hole three-dimensional flow probe were measured using one of two Scannivalve ZOC17 pressure scanners. For Station 1.0 measurements, a ±2.5 psig pressure scanner was appropriate; for Station 1.5 measurements, a ±15 psig pressure scanner was appropriate. Specifications of the pressure scanners are summarized in Table 2.5. The total temperature of the flow was measured with a standard K-Type thermocouple.

Table 2.5: Scannivalve ZOC17 Pressure Scanner Specifications

Number of Pressure Inputs	8
Full Scale Range	±2.5 psig (upstream) ±15 psig (downstream)
Excitation Voltage	±15 Vdc @ 100mA
Output Voltage	±5 Vdc
Span	10 Vdc
Accuracy (Linearity, Hysteresis, Repeatability)	±0.08% Full Scale
Resolution	Infinite
Scan Rate	50 kHz
Compensated Temperature Range	32-122 °F
Zero Temperature Effects	±0.009% Full Scale
Span Temperature Effects	±0.007% Full Scale
Proof Pressure	200% Full Scale Pressure

The probe was secured in a traversing-rotating mount (Figure 2.7) allowing for two degrees of positioning freedom. The linear traversing mechanism was driven by a stepper motor allowing the probe sensing area to plunge radially through the fan case. The manually controlled rotatory mechanism allowed the probe sensing area to rotate for alignment during installation in the engine. Once aligned, the rotary table was locked in place via set screws and did not move throughout data collections. A detailed probe installation guide can be found in Appendix B.

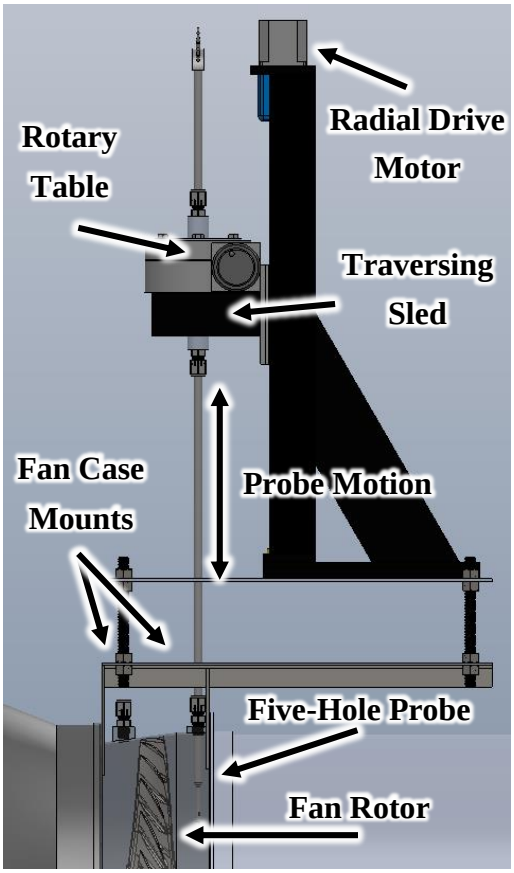

Figure 2.7: Five-Hole Three-Dimensional Flow Probe Radial Traversing Mount shown in Station 1.0 Configuration

2.3.7 Data Acquisition System

Excitation voltage for the two types of pressure transducers was independently supplied by two dedicated Agilent E3610A DC power supplies. Voltage outputs from the eight Omega PX139-005D4V pressure transducers and five Scannivalve ZOC17 pressure transducers were measured using National Instruments PXI-6255 digital voltmeters housed in a National Instruments PXI-1044 chassis and recorded by a local desktop PC.

Thermocouple wires were routed to a National Instruments SCXI-1303 isothermal terminal block serving as a high-accuracy cold-junction. The generated voltage was conditioned using a National Instruments SCXI-1102 module and measured using a National Instruments PXI-6255 digital voltmeter housed in a National Instruments PXI-1044 chassis and recorded by a local desktop PC.

The voltage output from the Monarch ROS-W Remote Optical Sensor was sampled at high-frequency and measured using a dedicated National Instruments PXI-6255 digital voltmeter housed in a National Instruments PXI-1044 chassis and recorded by a local desktop PC. In an effort to limit high-frequency data file size, the fan speed was processed real time to output engine speed rather than raw voltages. Data acquisition sample rates for the various instrumentation is summarized in Table 2.6.

Table 2.6: Data Acquisition Sample Rates

Pressure Measurements	128 Hz
Temperature Measurements	4 Hz
Fan Speed Measurements	500000 Hz (Processed to 4 Hz Speed Signal)

All data acquisition and motor control was facilitated through the use of a custom National Instruments LabView software package.

2.4 The Experimental Test Matrix

In order to thoroughly characterize the effects of inlet swirl distortion on the fan rotor of an operating turbofan engine, a comprehensive test matrix was devised. This test plan consisted of selecting a fan speed, defining radial and circumferential measurement locations, setting data sampling times, and choosing a feasible number of test replications. The following section summarizes the decision making process behind forming and implementing the experimental test matrix (Table 2.7 – Table 2.9).

2.4.1 Selecting the Fan Speed

With the incorporation of a mid-span shroud and a part-span stiffener, the Pratt & Whitney Canada JT15D-1 was well suited for inlet swirl distortion tests and the associated dynamic blade loading conditions. These design features resulted in limited risk of aeromechanical failure. Aerodynamic effects of the inlet swirl distortion and the associated non-uniform flow directionality entering the fan rotor were more difficult to overcome and posed considerable risk to the fan stall margin. In order to mitigate the threat of fan stall, the corrected fan speed was restricted to 65% of design maximum and held constant for all measurements. This fan speed setting provided ample stall margin for the fan under the severe inlet swirl distortion conditions and resulted in near transonic blade tip speeds with an inlet mass flow rate of approximately 45 lbm/s.

2.4.2 Selecting the Measurement Locations

Axial measurement planes located immediately upstream (Station 1.0) and immediately downstream (Station 1.5) of the fan rotor isolated the component for analysis (Figure 2.3). At each measurement plane, a coordinated procedure of incrementally rotating the StreamVane swirl distortion generator while incrementally traversing the five-hole three-dimensional flow probe allowed complete mapping of the flow profile. For all measurements, the inlet plane of the

StreamVane generator was located approximately two fan diameters upstream of the fan inlet plane.

The StreamVane was incrementally rotated 15 degrees to achieve 24 circumferential measurement locations at each axial measurement plane. Due to engine architecture, the number of possible radial measurement locations at each axial measurement plane varied slightly. At Station 1.0, the five-hole probe was unobstructed and could be plunged through the fan case to the hub. At Station 1.5, the core/bypass splitter case interfered with and limited the plunge depth of the probe. For congruency, all Station 1.0 radial measurement locations were repeated at Station 1.5 with the exception of two near hub radial locations.

Additionally, the axial clearance of the probe varied at each radial measurement location due to fan blade lean. Station 1.0 measurements were taken within one and one quarter inches upstream of the fan rotor leading edge; Station 1.5 measurements were taken within one half of one inch downstream of the fan rotor trailing edge. Figure 2.8 summarizes the five-hole three-dimensional flow probe measurement locations for this investigation.

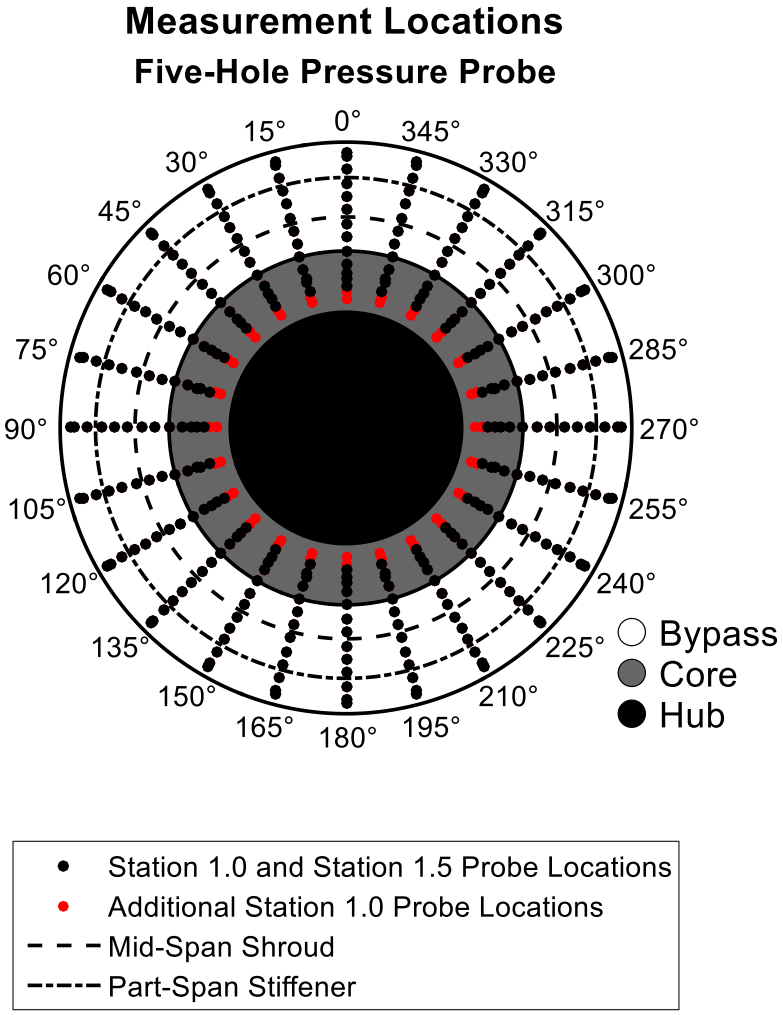

Figure 2.8: Five-Hole Three-Dimensional Flow Probe Measurement Locations

2.4.3 Selecting the Data Acquisition Parameters

Experimental data was collected for five seconds at each measurement location to determine a steady state mean value. After each movement but before each collection, a three second dwell period was set to allow the flow to reach steady state conditions. Additionally, five test replications at each experimental condition were performed to gather a statistical basis for measurement accuracy and repeatability. The repeated test results provided an acceptable level of accuracy in the measured data.

2.4.4 Summarizing the Text Matrix

Table 2.7: The Experimental Test Matrix – Engine Settings for Test

Corrected Fan Speed (% Max. of 16000 RPM)	65% Max. (Approx. 10400 RPM)
Fan Blade Tip Speed	950 ft/s (Approx. 0.85 Mach)
Corrected Inlet Mass Flow Rate	45 lbm/s (Nominal)
Fan Pressure Ratio	1.27 (Nominal)

Table 2.8: The Experimental Test Matrix (Continued) – Experimental Parameters

	Station 1.0	Station 1.5
Number of Circumferential Locations	24	24
Number of Radial Locations	15	13
Axial Clearance of Probe to Fan Rotor	<1.25”	<0.50”
Sampling Time	5 seconds	5 seconds
Settling Time	3 seconds	3 seconds
Number of Test Replications	5	5

Table 2.9: The Experimental Test Matrix (Continued) – Measurement Locations for Test

Radial Location	Circumferential Location	Axial Location
r/r_{tip}	θ	Station Number
0.45	0-345° by 15°	1.0
0.48	0-345° by 15°	1.0
0.49	0-345° by 15°	1.0 & 1.5
0.52	0-345° by 15°	1.0 & 1.5
0.54	0-345° by 15°	1.0 & 1.5
0.57	0-345° by 15°	1.0 & 1.5
0.62	0-345° by 15°	1.0 & 1.5
0.67	0-345° by 15°	1.0 & 1.5
0.71	0-345° by 15°	1.0 & 1.5
0.76	0-345° by 15°	1.0 & 1.5
0.81	0-345° by 15°	1.0 & 1.5
0.86	0-345° by 15°	1.0 & 1.5
0.90	0-345° by 15°	1.0 & 1.5
0.95	0-345° by 15°	1.0 & 1.5
0.96	0-345° by 15°	1.0 & 1.5

To determine the deviations in flow properties from nominal uniform inlet flow conditions, the StreamVane was removed from the setup and "clean" test measurements were collected. The clean test setup involved removing the StreamVane distortion generator, the StreamVane rotator, and the StreamVane outlet wall static pressure taps. Fan speed settings were identical to distorted test settings; however, with the absence of the blockage profile from the StreamVane device in the inlet duct, the corrected air mass flow rates entering the engine were slightly elevated during clean tests. Additionally, since the clean test flow profile was assumed uniform, the measurements were only required to be taken at a single circumferential location.

2.5 Experimental Setup and Procedure

2.5.1 Overview

Testing for both measurement planes consisted of a rigorous, well-defined experimental procedure that ensured the collection of useful data in the most accurate and efficient method possible. This procedure involved installing and aligning the multi-dimensional flow probe into the engine, building the inlet tunnel ducting, setting up the StreamVane rotator and aligning the StreamVane distortion device, positioning and attaching the bellmouth inlet, connecting all instrumentation lines, calibrating all pressure transducers, conducting the engine test, recalibrating all pressure transducers, and post-processing data (summarized in Figure 2.9). The following sections provide a detailed outline of the experimental procedure utilized for engine testing of swirl distortion including important differences between the axial measurement planes (Station 1.0 and Station 1.5) that were required due to engine architecture, clearances, and risk management. An illustrated engine setup procedure can be found in Appendix B.

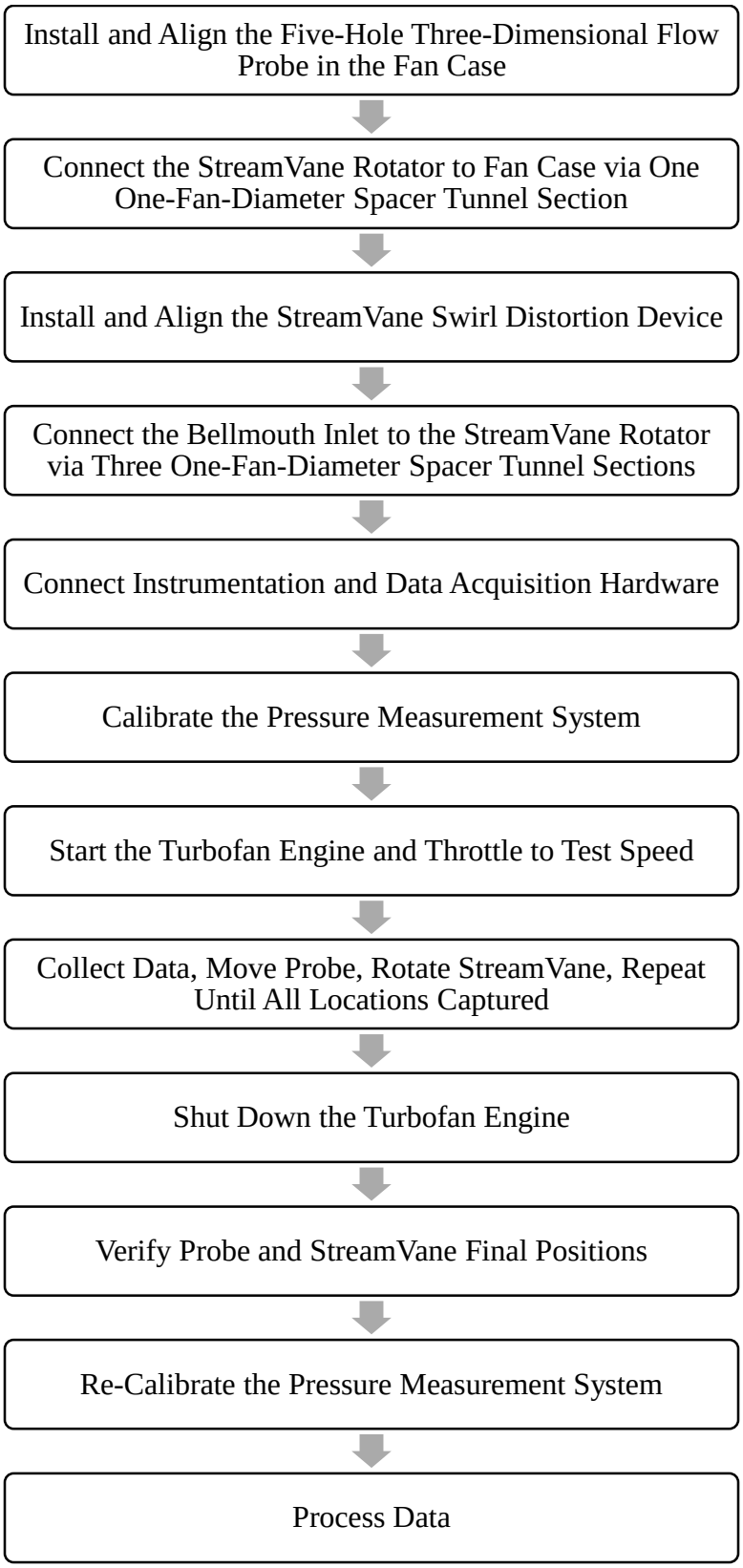

Figure 2.9: Experimental Procedure Overview

2.5.2 Station 1.0 – Fan Rotor Inlet Tests

Station 1.0 experimental setup began with the P&WC JT15D-1 turbofan engine mounted in a custom pylon which allowed easy access to the fan case. The five-hole, three-dimensional flow probe was the first instrument installed on the research platform. A universal radial traverse fixture was mounted using existing hardpoints on the fan case and the radial traverse was then positioned at the appropriate streamwise location. A rotary table was then installed on the radial traverse to allow for two degrees of freedom in probe alignment. Compression fittings on the exterior of the fan case and top and bottom of the rotary table secured the probe throughout testing. The probe mount axis was aligned perpendicular to the engine axis using a certified straight stainless steel shaft that was an identical diameter to the five-hole, three-dimensional probe. This procedure ensured that the probe would plunge smoothly and accurately through the fan case into the flow path.

With the alignment shaft replaced by the probe, and the probe inserted through the fan case, radial and rotary alignment was performed. The probe was secured in the compression fittings and further locked in place with set screw shaft collars located above and below the rotary table mount. The motorized radial traverse was then used to retract the tip of the probe to the inner wall of the fan case. A feeler gage ensured that the tip of the probe was flush with the fan case wall, indicating that the probe was radially aligned. Next, a custom rotary alignment apparatus consisting of a stiff aluminum frame and brass tubing was bolted to the fan case. The tubing was assumed to be parallel to the engine axis and served as a small open jet wind tunnel impinging on the sensing head of the five-hole probe. The close proximity of the open end of the tubing to the five-hole probe ensured that the flow was axial at the impingement point. A Dwyer 477A-1 handheld digital manometer was then connected to the P2-P3 pressure ports on the five-hole probe and compressed air was supplied to the upstream end of the brass tubing. Exploiting the nulling nature of the prism style five-hole probe, the rotary table was rotated while monitoring the manometer until the measured differential pressure was stable near zero. The angle on the rotary table was noted, and the process was repeated several times until the standard error of the average measured angle was within a tolerance threshold of ±0.020°. With the probe aligned to the flow direction, the rotary alignment apparatus was removed, the probe was retracted to the inner wall of the fan case, the five-pressure ports were connected to the dedicated pressure transducers via plastic tubing, and the thermocouple was connected to the terminal block via thermocouple wire. A detailed probe alignment process guide can be found in Appendix B.

Next, a thin walled, aluminum inlet duct tunnel section was fastened to the fan case. This tunnel section was used to position the StreamVane at an appropriate upstream location. The offset distance allowed the small-scale wake structures generated by the turning vanes of the StreamVane device to dissipate before entering the measurement plane and fan rotor. Also, a mounting plate for the optical once-per-rev speed sensor was attached to the wall of this tunnel section, allowing the device to view the tip of the spinner cone where the reflective target was attached.

Continuing upstream, the StreamVane rotator was attached to the tunnel section. The StreamVane was aligned in the rotator using specific markings on the StreamVane shroud and the rotator tunnel walls. With the StreamVane aligned, the static pressure taps at the outlet flange were connected to the dedicated pressure transducers via plastic tubing. The bellmouth inlet was then fastened to

the upstream rotator flange and secured. The static pressure taps (located at one and one half diameters downstream of the bellmouth inlet) were connected to the dedicated pressure transducers via plastic tubing.

With the engine setup complete, the pressure system was calibrated prior to engine startup. For this, a Dwyer 477B-4 handheld digital manometer was used to set a known reference input pressure. The Omega PX139-005D4V pressure transducers were calibrated to an appropriate range (typically 0 to 2.5 psig) by supplying an elevated reference pressure across the entire bank of eight transducers and recording a negative differential pressure representing a wall static pressure. The Scannivalve ZOC17 pressure transducers were calibrated to an appropriate range (typically 0 to 2.5 psig) by supplying an elevated reference pressure across the entire bank of eight transducers and recording a negative differential pressure similar to test conditions. Following calibration, the instrumentation pressure lines were reconnected to each transducer in preparation for testing.

A custom National Instruments LabView software package was then initialized on the data acquisition computer. This software allowed the user to set data acquisition rates and times for the various instruments, to define motor positions for both the StreamVane rotator and radial traverse, and to monitor instrumentation signals throughout the test. All experimental values were "Locked-In" prior to engine start and automatically called upon during data collection.

The engine was then started and allowed to idle for several minutes to reach an equilibrium temperature. After warming, the throttle position was set to an uncorrected fan speed based on the local atmospheric temperature and again allowed to stabilize. Once stabilized, the data acquisition software commanded the radial traverse motor to plunge the five-hole probe to the desired depth, paused briefly to allow the pressure to reach steady state, collected pressure and temperature data simultaneously, then moved radially to the next plunge depth where the data collection process repeated. After the last radial location, the probe retracted to the "Home" position, the rotator engaged, rotating the StreamVane, and the plunge process repeated. Through the coordinated motions of incrementally plunging the five-hole probe and rotating the StreamVane distortion device, the entire flow profile was measured.

After the measurement domain was fully mapped, the engine was shutdown, the experimental setup was inspected for any inconsistencies from startup conditions, and the pressure transducers were recalibrated using an identical process as previously defined.

It should be noted that minor changes were made to the setup for clean, non-distorted flow testing. First, the StreamVane rotator was removed from the inlet tunnel and replaced by a smooth wall tunnel section of identical axial length. Removing the StreamVane rotator also removed the StreamVane outlet wall static pressure taps. Because the flow was assumed uniform in the clean test, five-hole probe measurements were only taken at the top-dead-center circumferential location at each plunge depth. All other parameters, including engine fan speed and data acquisition rates and times, remained constant regardless of test conditions.

2.5.3 Station 1.5 – Fan Rotor Outlet Tests

Station 1.5 experimental setup began with the P&WC JT15D-1 turbofan engine mounted in a custom pylon which allowed easy access to the fan case. The five-hole, three-dimensional flow probe was the first instrument installed on the research platform. A universal radial traverse fixture was mounted using existing hardpoints on the fan case and the radial traverse was then positioned at the appropriate streamwise location. A rotary table was then installed on the radial traverse to allow for two degrees of freedom in probe alignment. Compression fittings on the exterior of the fan case and top and bottom of the rotary table secured the probe throughout testing. The probe mount axis was aligned perpendicular to the engine axis using a certified straight stainless steel shaft that was an identical diameter to the five-hole, three-dimensional probe. This procedure ensured that the probe would plunge smoothly and accurately through the fan case into the flow path.

With the alignment shaft replaced by the probe, and the probe inserted through the fan case, radial and rotary alignment was performed. The probe was secured in the compression fittings and further locked in place with set screw shaft collars located above and below the rotary table mount. The motorized radial traverse was then used to retract the tip of the probe outside the fan case. Next, a custom rotary alignment apparatus consisting of a stiff aluminum frame and brass tubing was bolted to the fan case. The tubing was assumed to be parallel to the engine axis and served as a small open jet wind tunnel impinging on the sensing head of the five-hole probe. The close proximity of the open end of the tubing to the five-hole probe ensured that the flow was axial at the impingement point. A Dwyer 477A-1 handheld digital manometer was then connected to the P2-P3 pressure ports on the five-hole probe and compressed air was supplied to the upstream end of the brass tubing. Exploiting the nulling nature of the prism style five-hole probe, the rotary table was rotated while monitoring the manometer until the measured differential pressure was stable near zero. The angle on the rotary table was noted, and the process was repeated several times until the standard error of the average measured angle was within a tolerance threshold of ±0.020°. The probe was then plunged through the fan case and retracted to the inner wall of the fan case. A feeler gage ensured that the tip of the probe was flush with the fan case wall, indicating that the probe was radially aligned. With the probe properly aligned to the flow direction and retracted to the inner wall of the fan case, the five-pressure ports were connected to the dedicated pressure transducers via plastic tubing, and the thermocouple was connected to the terminal block via thermocouple wire. A detailed probe alignment process guide can be found in Appendix B.

Next, a thin walled, aluminum inlet duct tunnel section was fastened to the fan case. This tunnel section was used to position the StreamVane at an appropriate upstream location. The offset distance allowed the small-scale wake structures generated by the turning vanes of the StreamVane device to dissipate before entering the measurement plane and fan rotor. Also, a mounting plate for the optical once-per-rev speed sensor was attached to the wall of this tunnel section, allowing the device to view the tip of the spinner cone where the reflective target was attached.

Continuing upstream, the StreamVane rotator was attached to the tunnel section. The StreamVane was aligned in the rotator using specific markings on the StreamVane shroud and the rotator tunnel walls. With the StreamVane aligned, the static pressure taps at the outlet flange were connected to the dedicated pressure transducers via plastic tubing. The bellmouth inlet was then fastened to

the upstream rotator flange and secured. The static pressure taps (located at one and one half diameters downstream of the bellmouth inlet) were connected to the dedicated pressure transducers via plastic tubing.

With the engine setup complete, the pressure system was calibrated prior to engine startup. For this, a Dwyer 477B-4 handheld digital manometer was used to set a known reference input pressure. The Omega PX139-005D4V pressure transducers were calibrated to an appropriate range (typically 0 to 2.5 psig) by supplying an elevated reference pressure across the entire bank of eight transducers and recording a negative differential pressure representing a wall static pressure. The Scannivalve ZOC17 pressure transducers were calibrated to an appropriate range (typically 0 to 10 psig) by supplying an elevated reference pressure across the entire bank of eight transducers and recording a positive differential pressure similar to test conditions. Following calibration, the instrumentation pressure lines were reconnected to each transducer in preparation for testing.

A custom National Instruments LabView software package was then initialized on the data acquisition computer. This software allowed the user to set data acquisition rates and times for the various instruments, to define motor positions for both the StreamVane rotator and radial traverse, and to monitor instrumentation signals throughout the test. All experimental values were "Locked-In" prior to engine start and automatically called upon during data collection.

The engine was then started and allowed to idle for several minutes to reach an equilibrium temperature. After warming, the throttle position was set to an uncorrected fan speed based on the local atmospheric temperature and again allowed to stabilize. Once stabilized, the data acquisition software commanded the radial traverse motor to plunge the five-hole probe to the desired depth, paused briefly to allow the pressure to reach steady state, collected pressure and temperature data simultaneously, then moved radially to the next plunge depth where the data collection process repeated. After the last radial location, the probe retracted to the "Home" position, the rotator engaged, rotating the StreamVane, and the plunge process repeated. Through the coordinated motions of incrementally plunging the five-hole probe and rotating the StreamVane distortion device, the entire flow profile was measured.

After the measurement domain was fully mapped, the engine was shutdown, the experimental setup was inspected for any inconsistencies from startup conditions, and the pressure transducers were recalibrated using an identical process as previously defined.

It should be noted that minor changes were made to the setup for clean, non-distorted flow testing. First, the StreamVane rotator was removed from the inlet tunnel and replaced by a smooth wall tunnel section of identical axial length. Removing the StreamVane rotator also removed the StreamVane outlet wall static pressure taps. Because the flow was assumed uniform in the clean test, five-hole probe measurements were only taken at the top-dead-center circumferential location at each plunge depth. All other parameters, including engine fan speed and data acquisition rates and times, remained constant regardless of test conditions.

Chapter 3 – Experimental Data Analysis

3.1 Introduction to the Data

Throughout the investigation, a large amount of experimental data was collected and a rigorous bookkeeping and processing strategy was necessary. One optical once-per-rev fan speed sensor, nine to thirteen pressure transducers, one thermocouple, all sampled at various rates and ranges at each of the approximately 300 collection points, repeated five times, both fore and aft of the fan rotor resulted in nearly 50,000 individual measurements.

In order to maintain organization, the data acquisition system automatically recorded each measurement as a sequential file which was indexed and documented for offline processing. With each file corresponding to a different measurement, it was extremely important to maintain accurate documentation. Following the conclusion of each test, the data files were quickly post-processed and examined for validity before continuing with the next series of collections. Inter-test data validation ensured that collected measurements were within anticipated ranges and indicated any problems with experimental setup before the initiation of the next test.

At the conclusion of each measurement plane data collection phase, a formal data reduction was performed. This included processing the raw instrumentation data, time averaging sampled data, correlating physical measurements to desired flow parameters, calculating inferred parameters from measured parameters, and test-to-test averaging of repeated results. The following sections describe the data reduction, processing, and analysis techniques employed to extract physical, meaningful information form the collected experimental data.

3.2 Instrument Data Reduction

3.2.1 Overview

Three distinct measurement devices were utilized to collect experimental data. An optical once-per-rev speed sensor measured fan speed, pressure transducers measured static wall pressures and five-hole three-dimensional flow probe pressures, and a thermocouple measured flow total temperature. Each instrument required a unique data reduction process to extract useful information regarding the physical phenomena associated with a turbofan engine operating in a distorted inflow condition.

3.2.2 Optical Once-Per-Rev Speed Sensor

The optical once-per-rev speed sensor is a laser emitting/detecting device used for timing of rotating shafts. The emitter pulses a laser beam while a detector waits for a return pulse from a reflective target attached to the spinner cone on the fan shaft. The detector operates as a binary instrument, returning voltage levels based on the status of the return signal. While a return signal is not detected, the sensor records a high state voltage; conversely, when a return signal is detected, the sensor records a low state voltage. An inline LabView pulse edge monitoring routine detected changes between the state level of the signal and automatically calculated the period of time between successive pulses. The timing signal was then used to calculate the rotational speed of the fan as the inverse of pulse frequency.

The optical once-per-rev sensor was active for the entire period of engine operation but only recorded engine speed data during discrete data collection windows. With a sample rate of 500 kHz, 2.5 million samples were produced over the full five second sampling waldo window. Because speed resolution was not critical to the experimental investigation, these speed values were stored for one quarter second, time averaged, and recorded at a reduced sample rate of 4 Hz. As a means of reducing data file size, it was important to process the speed data in real-time and output only useful speed information for experimental condition monitoring.

The time-averaged fan speed for a single data point was then calculated from the 4 Hz data. Because atmospheric conditions change, the time-averaged speed was corrected to standard atmospheric conditions according to Equation 3.1. This corrected fan speed served as a means of reporting identical experimental conditions among subsequent tests regardless of local atmospheric conditions.

$$N_{1_{corr}} = \frac{N_{1_{meas}}}{\sqrt{\theta}} \tag{3.1}$$

3.2.3 Pressure Transducers

Two types of pressure transducers were utilized for collecting pressure data during experimental tests with each outputting voltages that were linearly proportional to the applied pressures. Prior to and following each experimental test, the pressure transducers were calibrated to a specific range by supplying several known reference pressures and recording the associated output voltages. With the supplied pressure/voltage relationship, linear fit models were calculated for each transducer (Equation 3.2). These linear fit models were later used to interpret the recorded voltages into usable pressure data.

$$P_{meas} = mV_{meas} + b \tag{3.2}$$

The pressure transducer voltages were sampled at 128 Hz over the five second data collection period. The recorded voltages were processed using linear fit models and time-averaged, resulting in a single steady state pressure data point. Because atmospheric conditions change, the time-averaged measured pressure was corrected to standard atmospheric conditions according to

Equation 3.3. This corrected pressure served as a means of reporting identical experimental conditions among subsequent tests regardless of local atmospheric conditions.

$$P_{corr} = \frac{P_{meas}}{\delta} \tag{3.3}$$

3.2.4 Thermocouple

Air total temperature at each measurement point was measured using a standard K-type thermocouple embedded in the tip of the five-hole three-dimensional flow probe. The temperature data was processed real-time and recorded at 4 Hz. The time-averaged temperature from the five second data collection period was calculated from the sampled data resulting in a single steady state temperature data point. Because atmospheric conditions change, the time-averaged measured temperature was corrected to standard atmospheric conditions according to Equation 3.4. This corrected temperature served as a means of reporting identical experimental conditions among subsequent tests regardless of local atmospheric conditions.

$$T_{corr} = \frac{T_{meas}}{\theta} \tag{3.4}$$

3.3 Measured and Inferred Flow Parameters

3.3.1 Overview

Over the course of the investigation, the data collected by the various instruments were reduced into directly measured and indirectly computed flow parameters. Directly measured parameters include primitive pressure and temperature terms which were in turn used to calculate more complex flow details. These parameters characterized flow throughout the experiment. The following sections demonstrate the processes utilized to extract meaningful physical data from the compiled assortment of measurements.

3.3.2 Bellmouth Inlet Static Pressure

The four wall static pressure taps located on the bellmouth inlet tunnel wall measured and recorded the static pressure of the flow entering the research turbofan engine. Most importantly, the static pressure at this location was used to calculate the mass flow rate of air entering the engine. Along with the mass flow rate of air, variation in the four static pressure measurements can indicate interactions between the StreamVane and the inlet flow upstream of the distortion device.

3.3.3 Bellmouth Inlet Mass Flow Rate

The averaged value of the four static pressure measurements along with the total pressure within the inlet (assuming no losses, the total pressure in the inlet is equal to the atmospheric pressure) were used to calculate the Mach number at the defined bellmouth inlet plane (Equation 3.5). This Mach number was used to calculate an ideal mass flow rate (Equation 3.6) [48] from which the Reynolds number of the flow can be extracted (Equation 3.7).

$$M = \sqrt{\frac{2}{\gamma - 1}\left(\left(\frac{P_0}{P}\right)^{\frac{\gamma-1}{\gamma}} - 1\right)} \tag{3.5}$$

$$\dot{m}_{a_{ideal}} = \frac{P_0\sqrt{\gamma}}{\sqrt{RT_0}}\left(\frac{2}{\gamma+1}\right)^{\frac{\gamma+1}{2(\gamma-1)}} \tag{3.6}$$

$$Re_D = \frac{4\dot{m}_{a_{ideal}}}{\pi\mu D} \tag{3.7}$$

The Reynolds number dependent discharge coefficient of the actual bellmouth inlet was interpolated from calibration tables using the ideal Reynolds number input (Equation 3.8). The discharge coefficient was then used as a correction factor to calculate the actual inlet mass flow rate from the ideal inlet mass flow rate (Equation 3.9). Finally, the mass flow rate was corrected to standard atmospheric conditions to remove local atmospheric variations from the experimental data (Equation 3.10).

$$C_d = f(Re_D) \tag{3.8}$$

$$\dot{m}_a = C_d\dot{m}_{a_{ideal}} \tag{3.9}$$

$$\dot{m}_{a_{corr}} = \frac{\dot{m}_a\sqrt{\theta}}{\delta} \tag{3.10}$$

3.3.4 StreamVane Outlet Static Pressure

The four wall static pressure taps located on the StreamVane outlet tunnel wall measured and recorded the static pressure of the flow immediately downstream of the distortion device. The static pressures at discrete circumferential measurement locations indicated the magnitude of secondary flow associated with the various features of the swirl distortion profile.

3.3.5 Radial Flow Angle

The radial flow angle measured the offset angle formed between the local flow direction and the axial flow direction in the radial reference frame. This parameter, along with the tangential flow angle, expresses one of the two principal indicators of secondary flow and provides verification of swirl within the measurement planes. Figure 3.1 illustrates the radial flow angle as the angle formed between the radial and axial velocity components, summarized by Equation 3.11.

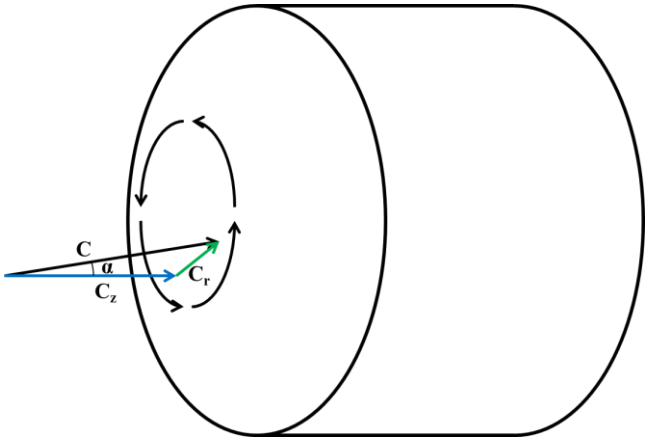

Figure 3.1: Radial Flow Angle Illustration

$$\alpha = \tan^{-1}\left(\frac{C_r}{C_z}\right) \tag{3.11}$$

The radial flow angle at Station 1.0 and Station 1.5 was measured using the five-hole three-dimensional flow probe. The measured pressures acting on the sensing ports of the probe were normalized into a pressure coefficient (Equation 3.12) [47] which was then interpolated to a calibration map (Figure 3.2). This calibration map related the pressure coefficient to a radial flow angle. The smoothly varying calibration map output a single radial flow angle based on the calculated pressure coefficient at each measurement location.

$$Cp_\alpha = \frac{P_4 - P_5}{P_1 - \bar{P}} \tag{3.12}$$

$$\bar{P} = \frac{P_2 + P_3 + P_4 + P_5}{4} \tag{3.13}$$

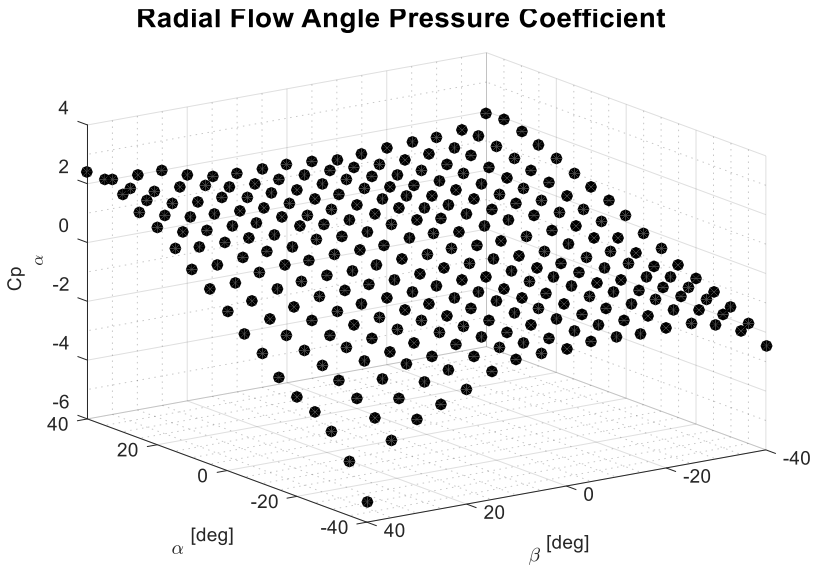

Figure 3.2: Radial Flow Angle Calibration Map

3.3.6 Tangential Flow Angle

The tangential flow angle, also referred to as the swirl angle, measured the offset angle formed between the local flow direction and the axial flow direction in the tangential reference frame. This parameter, along with the radial flow angle, expresses one of the two principal indicators of secondary flow and provides verification of swirl within the measurement planes. Figure 3.3 illustrates the tangential flow angle as the angle formed between the tangential and axial velocity components, summarized by Equation 3.14.

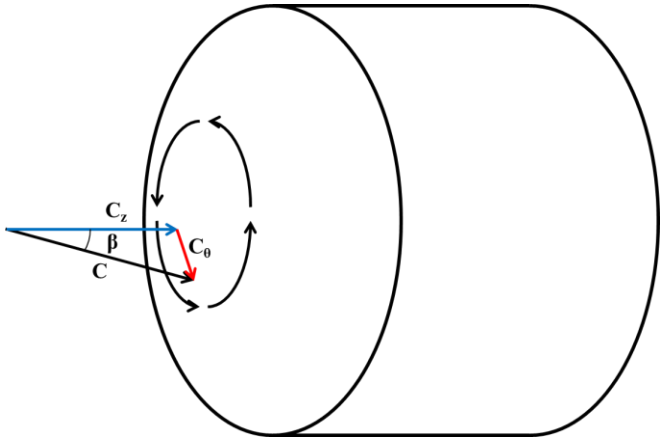

Figure 3.3: Tangential Flow Angle Illustration

$$\beta = \tan^{-1}\left(\frac{C_\theta}{C_z}\right) \tag{3.14}$$

The tangential flow angle Station 1.0 and Station 1.5 was measured using the five-hole three-dimensional flow probe. The measured pressures acting on the sensing ports of the probe were

normalized into a pressure coefficient (Equation 3.15) [47] which was then interpolated to a calibration map (Figure 3.4). This calibration map related the pressure coefficient to a tangential flow angle. The smoothly varying calibration map output a single tangential flow angle based on the calculated pressure coefficient at each measurement location.

$$Cp_{\beta} = \frac{P_2 - P_3}{P_1 - \bar{P}} \tag{3.15}$$

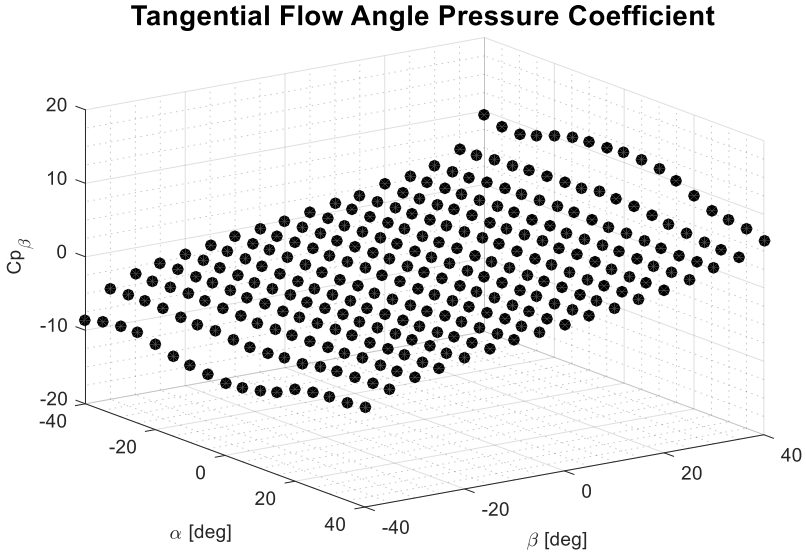

Figure 3.4: Tangential Flow Angle Calibration Map

3.3.7 Flow Total Pressure

Measuring the total pressure of the flow was important in determining the amount of energy contained in the fluid at the various stations surrounding the fan rotor. The upstream total pressure field (Station 1.0) indicated any losses resulting from flow interactions with the solid body distortion device as well as viscous losses resulting from turbulent diffusion, wall friction in the boundary layer, and secondary flow mixing. The downstream total pressure field (Station 1.5) indicated performance variations in the fan rotor such as changes in fan pressure ratio and work input to the flow.

After measuring the flow angles at the discrete measurement points, the total pressure of the flow could be found using a similar interpolation method as previous described. A total pressure pressure coefficient (Equation 3.16) was interpolated from a calibration map (Figure 3.5) at each radial and tangential flow angle pair. From the value, the total pressure of the flow could be calculated by algebraically rearranging Equation 3.17 [47] to Equation 3.18.

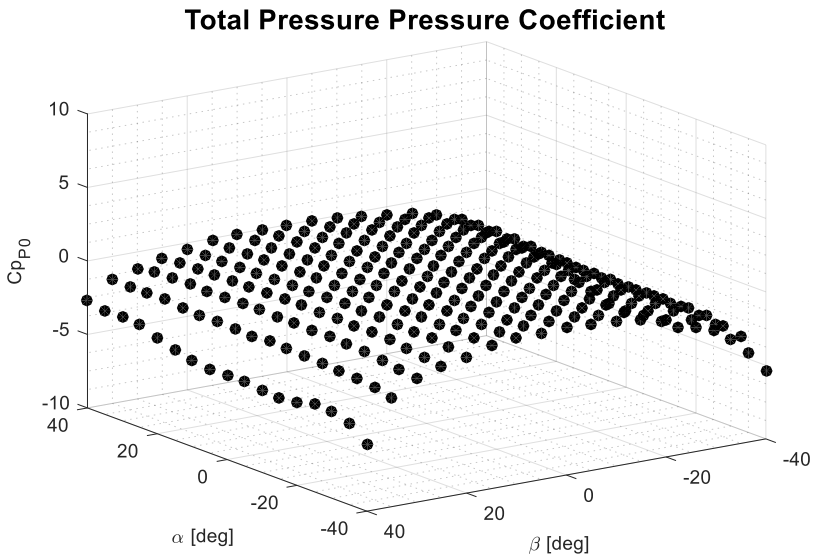

Figure 3.5: Flow Total Pressure Calibration Map

$$Cp_{P0} = f(\alpha, \beta) \tag{3.16}$$

$$Cp_{P0} = \frac{P_1 - P_0}{P_1 - \bar{P}} \tag{3.17}$$

$$P_0 = P_1 - Cp_{P0}(P_1 - \bar{P}) \tag{3.18}$$

3.3.8 Flow Static Pressure

The static pressure of the flow was important in estimating the velocity magnitude of secondary flow. Upstream (Station 1.0) variations in static pressure characterized regions of strong secondary flow where swirl was likely present. Downstream (Station 1.5) variations in static pressure indicated regions of the flow where swirl persisted through the rotor as well as potential evidence of flow separation from the rotor blades.

After measuring the flow angles at the discrete measurement points, the static pressure of the flow could be found using an interpolation method similar to the total pressure measurements. A static pressure pressure coefficient (Equation 3.19) was interpolated from a calibration map (Figure 3.6) at each radial and tangential flow angle pair. From the value, the static pressure of the flow could be calculated by algebraically rearranging Equation 3.20 [47] to Equation 3.21.

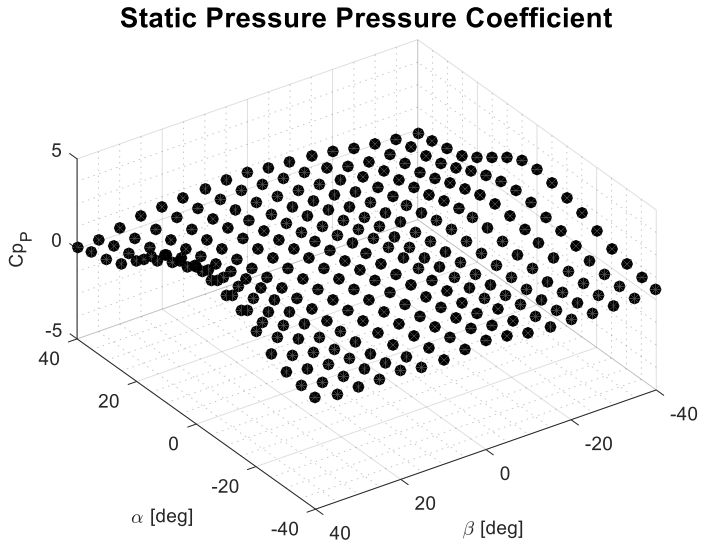

Figure 3.6: Flow Static Pressure Calibration Map

$$Cp_P = f(\alpha, \beta) \tag{3.19}$$

$$Cp_P = \frac{\bar{P} - P}{P_1 - \bar{P}} \tag{3.20}$$

$$P = \bar{P} - Cp_P(P_1 - \bar{P}) \tag{3.21}$$

3.3.9 Flow Mach Number

The Mach number was critical for measuring the velocity magnitude of the flow which further characterized the secondary flow profile. Utilizing the isentropic flow assumptions, the Mach number was a derived parameter consisting of a relationship between the total and static pressures of the flow (Equation 3.22).

$$M = \sqrt{\frac{2}{\gamma - 1}\left[\left(\frac{P_0}{P}\right)^{\frac{\gamma-1}{\gamma}} - 1\right]} \tag{3.22}$$

3.3.10 Flow Total Temperature

The flow total temperature was directly measured from the thermocouple embedded in the five-hole three-dimensional flow probe. Similar to the total pressure of the flow, variations in the total temperature indicated local changes in the energy of the flow as well as changes in the fan rotor efficiency.

3.3.11 Flow Static Temperature

The flow static temperature was the final component required to fully characterize the velocity profile at Station 1.0 and Station 1.5 measurement planes. After calculating the flow Mach number and total temperature, the isentropic flow assumptions were again employed to calculate the flow static temperature according to Equation 3.23.

$$T = \frac{T_0}{1 + \frac{\gamma - 1}{2} M^2} \tag{3.23}$$

3.3.12 Flow Velocity Profile

With the primitive flow properties of pressure and temperature measured and recorded, the velocity field was fully characterized. The three-dimensional velocity field illustrated the cumulative effects of the swirl distortion on the fan rotor performance. The Station 1.0 velocity profile indicated off axis flow entering the fan rotor; while the Station 1.5 velocity field indicated the persistence of swirl distortion through the rotor, flow turning abnormalities, and off design flow conditions entering downstream engine stages.

To compute the three-dimensional velocity components in polar coordinates, the velocity magnitude must first be determined. Equation 3.24 shows the calculation of the local speed of sound which was input into Equation 3.25 along with the calculated Mach number to determine the local velocity magnitude at each discrete measurement point.

$$a = \sqrt{\gamma R T} \tag{3.24}$$

$$C_{r\theta z} = Ma \tag{3.25}$$

Next, the velocity magnitude was decomposed into the three-dimensional velocity components using the measured flow angles. Figure 3.7 illustrates the coordinate vector system which relates the velocity components and velocity magnitude.

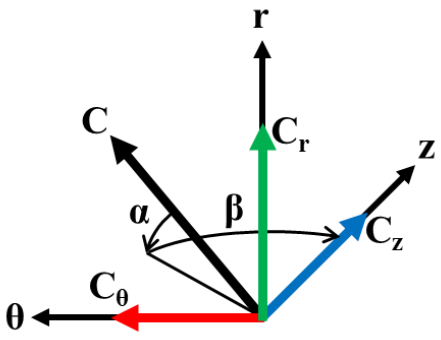

Figure 3.7: Three-Dimension Velocity Components in Polar Coordinates

From the figure, the relationship of radial flow angle, tangential flow angle, and velocity magnitude was defined. Due to the compound flow angles found within the flow field, a coordinate transformation (Equation 3.26-3.28) was derived to calculate the radial, tangential, and axial velocity components.

$$C_r = C_{r\theta z} \sin(\alpha) \tag{3.26}$$

$$C_\theta = C_{r\theta z} \cos(\alpha) \sin(\beta) \tag{3.27}$$

$$C_z = C_{r\theta z} \cos(\alpha) \cos(\beta) \tag{3.28}$$

With the components of the velocity profile extracted, the in-plane velocity magnitude was calculated as the square root sum of squared radial and tangential velocity components (Equation 3.29).

$$C_{r\theta} = \sqrt{{C_r}^2 + {C_\theta}^2} \tag{3.29}$$

Chapter 4 – Experimental Results and Discussion

4.1 Introduction to the Results

Physical flow parameters were measured and computed using the data collection and reduction process outlined in the previous two chapters. The conditions entering and exiting the fan rotor were critical in determining the effects of inlet swirl distortions on the operation and performance of the fan rotor stage of the turbofan engine research platform. These results included flow angles, pressures, temperatures, and velocity profiles as well as the experimental conditions of fan speed and air mass flow rate. The following chapter is separated into three sections which present the experimental results: Experimental Condition Monitoring, Station 1.0 Results, and Station 1.5 Results.

The Experimental Condition Monitoring section presents the measurements that were intended to remain constant throughout all tests. These measurements included fan speed, inlet air mass flow rate, bellmouth inlet static pressures, and StreamVane outlet static pressures. The results were presented and compared to demonstrate that desired experimental conditions were constant throughout the entire investigation.

The Station 1.0 Results section presents the measurements that were specific to the data acquired with the five-hole three-dimensional flow probe positioned at the inlet plane to the fan rotor. These measurements included radial and tangential flow angles, total and static pressures, Mach number, total and static temperatures, and secondary flow velocity profiles. The results were presented as contour plots that compare clean test (no StreamVane installed) results with distorted test (StreamVane installed) results. Because the flow was assumed to be uniform for the clean test condition and all data was taken at a single circumferential location, the clean test results were assumed to be constant at each radius around the circumference of the annulus.

The Station 1.5 Results section presents the measurements that were specific to the data acquired with the five-hole three-dimensional flow probe positioned at the outlet plane to the fan rotor. These measurements included radial and tangential flow angles, total and static pressures, Mach number, total and static temperatures, and secondary flow velocity profiles. The results were presented as contour plots that compare clean test (no StreamVane installed) results with distorted test (StreamVane installed) results. Because the flow was assumed to be uniform for the clean test condition and all data was taken at a single circumferential location, the clean test results were assumed to be constant at each radius around the circumference of the annulus.

In the plots, the fan angle, θ, was often used as the independent variable for comparison of the various parameters. The fan angle was defined as the angle, with respect to top-dead-center, through which the fan rotates to match the rotated StreamVane index. In other words, the fan angle was the angle which matches the location of the distortion profile as it would be encountered in a fixed geometry inlet duct of an operational aircraft configuration. Therefore, the results were presented in a stationary reference frame with respect to the StreamVane as though the five-hole three-dimensional flow probe was physically moved to each discrete circumferential location. Figure 4.1 offers an illustration to help clarify the data visualization scheme.

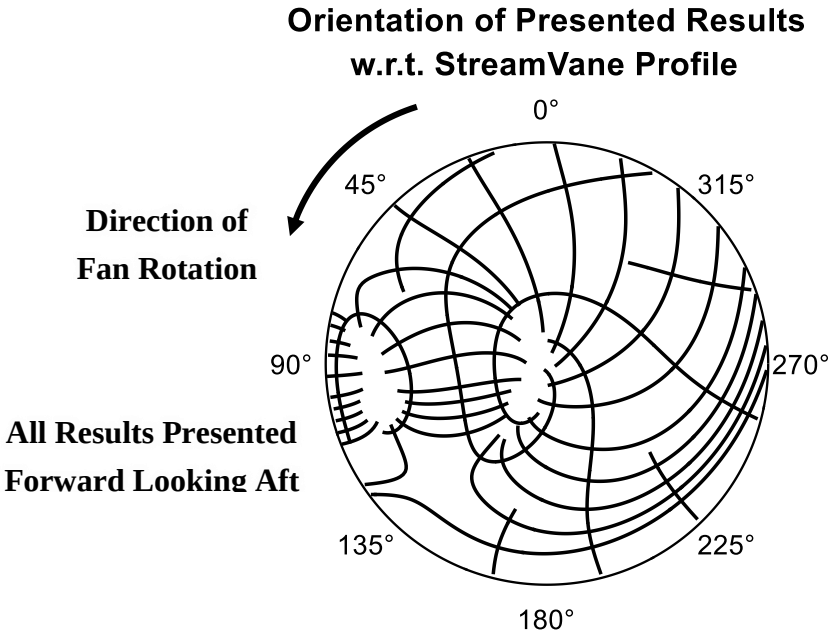

Figure 4.1: Method of Experimental Results Presentation

Due to significant differences in results at the two measurement planes, the use of identical scales was not always appropriate; therefore, special attention must be given to understanding the scaling used in the various plots. Also, normalization with atmospheric conditions is typically used and is noted when applied.

4.2 Experimental Condition Monitoring

4.2.1 Overview

This section presents the experimental results that were independent of the five-hole three-dimensional flow probe measurement plane. The fan speed, inlet air mass flow rate, bellmouth inlet static pressure, and StreamVane outlet static pressure were intended to remain constant throughout the investigation such that the measurements at the two fan rotor interrogation planes were comparable.

The data presented in the subsequent plots is the test-to-test average results from five repeated tests at a single constant fan speed. Where available, clean and distorted test results are presented for side-by-side comparison. All results are presented forward-looking-aft (FLA) with the fan angle beginning at top-dead-center and progressing anti-clockwise in the direction of fan rotation (summarized in Figure 4.1).

4.2.2 Fan Speed

The one controllable parameter held constant throughout the entire investigation was the fan speed setting. Due to the hydro-mechanical throttle control used by the P&WC JT15D-1 turbofan engine, the fan speed fluctuated, or hunted, during operation. While the variations in fan speed were limited to approximately ±0.2%, repeated testing was necessary to obtain a stationary statistical data set from which conclusions could be drawn.

The throttle control mechanism in the engine utilizes discrete sensors within the flow path to adjust fuel flow rates and maintain a constant fan speed. In a distorted test condition, the sensors can detect disturbances in the pressure field and fluctuate the fuel flow rate accordingly. This fluctuation was typically minor and was related to the StreamVane circumferential set point. As the profile rotated in the inlet duct, the distortion caused the core and fan speed to vary. For this reason, active throttle control by the engine operator was needed at each StreamVane circumferential set point. Once the speed value was tuned, data collection ensued and no additional throttle changes were made until the subsequent StreamVane rotation point.

The collected once-per-rev data was processed and corrected to standard atmospheric conditions. Figure 4.2 shows the resulting test-to-test average corrected fan speed trace for the five repetitions of distorted and clean tests.

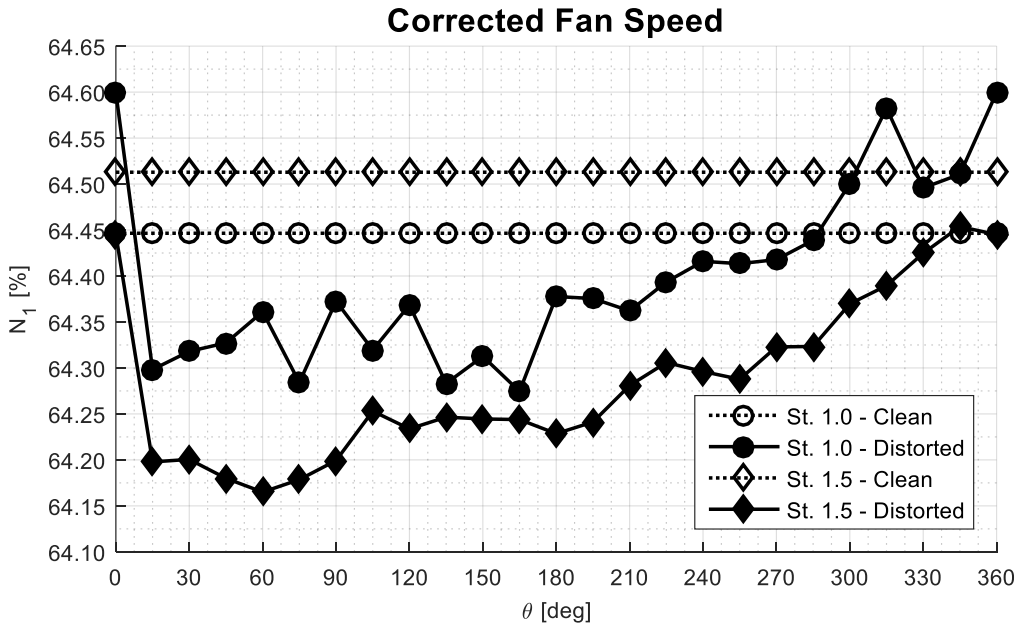

Figure 4.2: Corrected Fan Speed Trace w.r.t. Fan Angle

The average corrected fan speed was controlled to within one percent of the target fan speed of 65%, which was considered extraordinarily good for the hydro-mechanical speed control system on this engine. Comparing the Station 1.0 and Station 1.5 average corrected fan speed results showed that the fan speed was controlled to within one half of one percent for all test conditions, indicating near constant test conditions throughout the entire investigation.

4.2.3 Bellmouth Inlet Static Pressure

The test-to-test average bellmouth static pressure results normalized by the atmospheric pressure are presented in Figure 4.3. The results showed an elevated static pressure in the inlet duct when the StreamVane was installed. This result was attributed to the distortion device blockage profile which created deficits in axial through flow velocity yielding increases in static pressure. Due to negligible circumferential effects upstream of the StreamVane distortion device, the four bellmouth static pressure measurements were combined into a single averaged data point. This averaged data point was then used to calculate the inlet air mass flow rate, as described in Chapter 3.

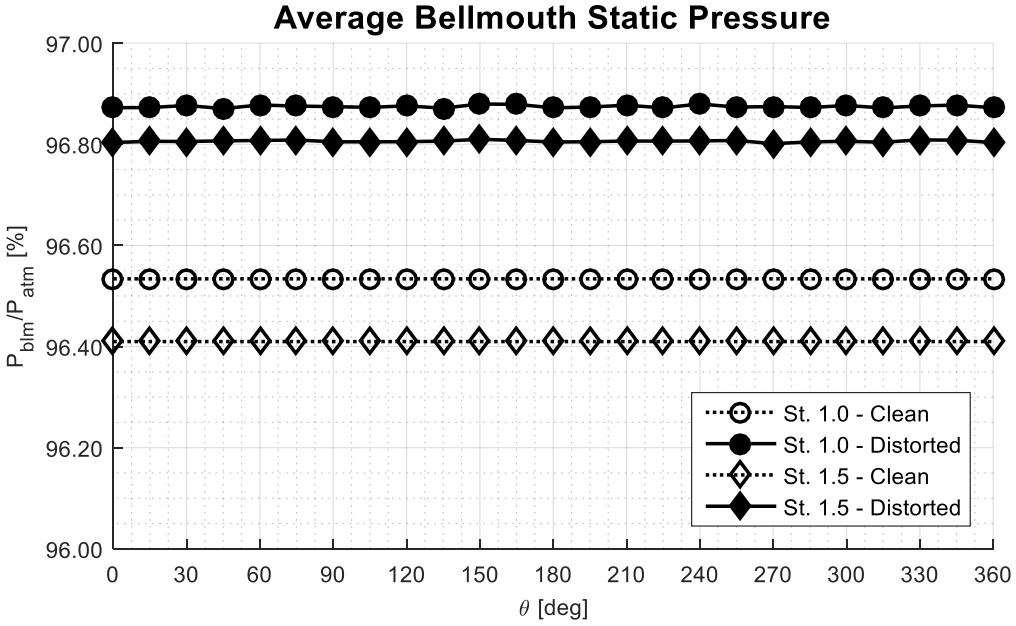

Figure 4.3: Bellmouth Inlet Static Pressure w.r.t. Fan Angle

4.2.4 Bellmouth Inlet Mass Flow Rate

Figure 4.4 illustrates the test-to-test average corrected inlet air mass flow rate entering the engine at each fan angle measurement point throughout the entire measurement campaign. Due to the increased bellmouth inlet static pressure and resulting deficit in through flow velocity caused by the StreamVane blockage profile, the mass flow rate under distorted test conditions was found to be approximately one pound-mass per second lower than that of the clean test conditions. The

remarkable outcome is the stability in the mass flow rate across the measurement domain. Through the use of the hydro-mechanical throttle control on the turbofan engine, nearly constant experimental conditions were accomplished.

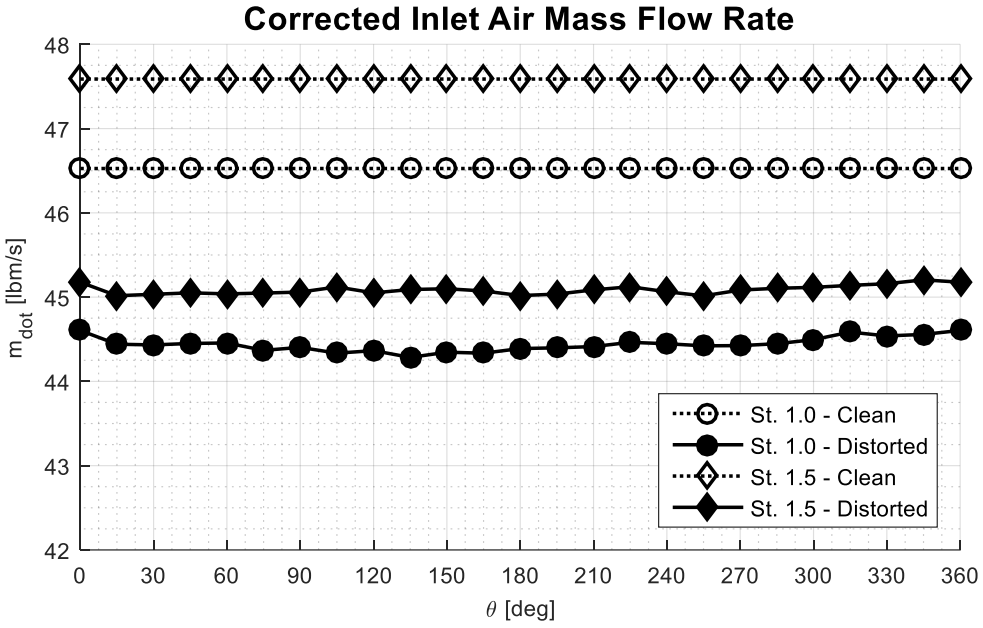

Figure 4.4: Bellmouth Inlet Corrected Air Mass Flow Rate w.r.t. Fan Angle

4.2.5 StreamVane Outlet Static Pressure

The first downstream measurements of the distortion profile occurred at the outlet plane of the StreamVane. The test-to-test average StreamVane outlet static pressure results normalized by the atmospheric pressure are presented in Figure 4.5. As displayed, the static pressure results at each circumferential location were rotated in a manner that relocates each static pressure measurement to the same fan angle. In other words, the four measurements were clocked relative to the fan angle such that each corresponds to an identical location with respect to the StreamVane profile.

Upon initial inspection of the data, the static pressure at the outlet of the StreamVane was everywhere lower than the bellmouth inlet static pressure. This result was due to the negative pressure gradient produced by the engine as well as the large amounts of secondary flow produced by the StreamVane. As the secondary flow mixes, the effects of the swirl propagate into the boundary layer flow which produces variations in the static pressure measurements at the wall.

Because the variation in the results from the four static pressure taps was considered low, the four measurements were collapsed into a single averaged data point at each circumferential fan angle. Figure 4.6 shows the resulting average wall static pressure at the outlet of the StreamVane distortion device with respect to the fan angle. In the figure, the static pressure was found to vary in a nearly cyclic procession at each of the fan angle measurement locations. Because the static pressure is inversely proportional to the flow velocity, low static pressure regions indicate elevated

velocity magnitude. Close analysis in the fan angle range of 90°-135° reveals that areas of high static pressure coincide with areas of substantial StreamVane blockage which could lead to mass flow redistribution. Similarly, near the fan angle of 225° the static pressure sharply rises; this rise is likely due to the support strut immediately upstream of the measurement location.

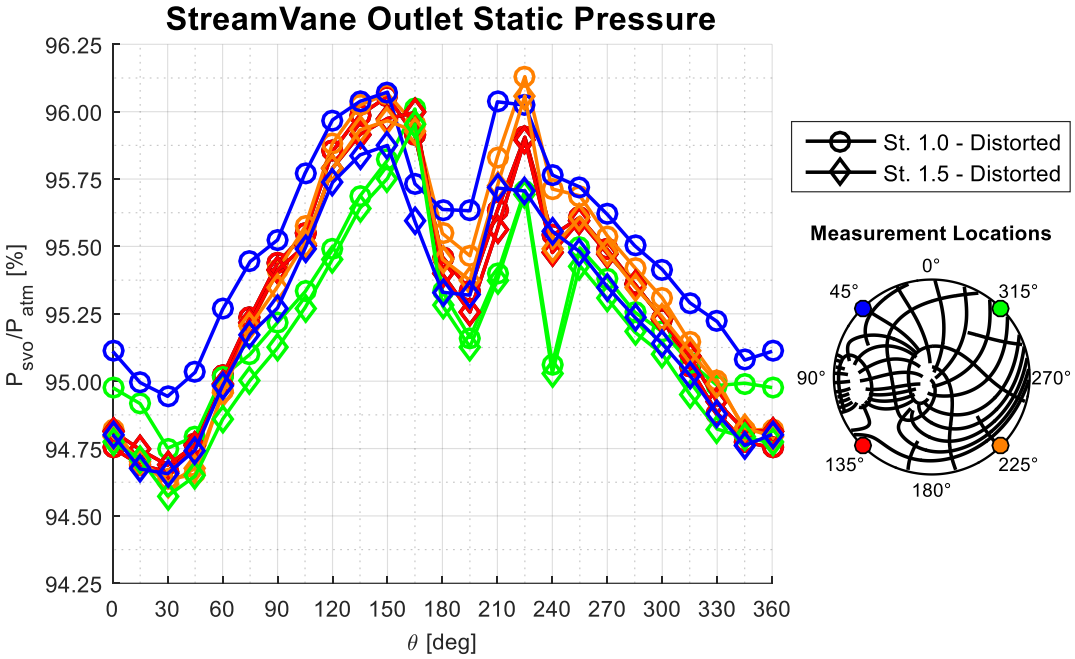

Figure 4.5: StreamVane Outlet Static Pressure w.r.t. Fan Angle

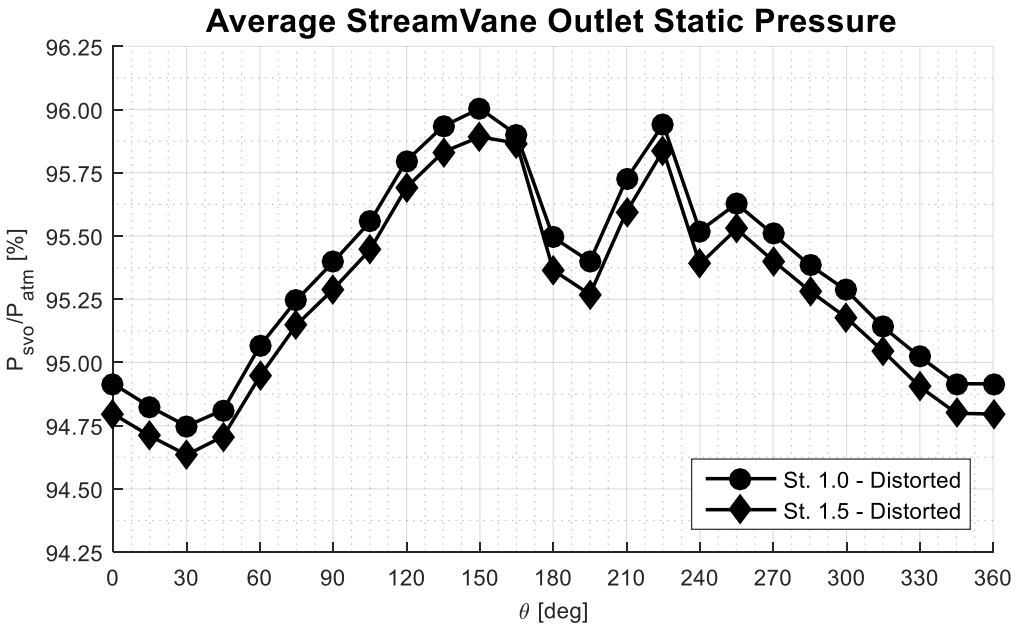

Figure 4.6: Average StreamVane Outlet Static Pressure w.r.t. Fan Angle

4.3 Station 1.0 – Fan Rotor Inlet Results

4.3.1 Overview

This section presents the flow conditions measured at Station 1.0, immediately upstream of the fan rotor leading edge. The data presented in the subsequent plots is the test-to-test average results from five repeated tests at a single, constant fan speed. Clean and distorted test results are presented for side-by-side comparison. When applicable, the deviations from clean results are also calculated and provided. In an attempt to efficiently and effectively present the data, all supporting figures can be found in Section 4.3.10 following the discussion of each individual parameter in Sections 4.3.2 – 4.3.9.

All results are presented forward-looking-aft (FLA) with the fan angle beginning at top-dead-center and progressing anti-clockwise in the direction of fan rotation.

4.3.2 Radial Flow Angle

The radial flow angle results at the fan rotor inlet plane (Station 1.0) are summarized in Figure 4.7. The radial flow angle measurements are presented positively outward from engine centerline, forward-looking-aft, and use the key found in lower right corner of the figure to illustrate the relative StreamVane position. The clean test results revealed a weak, 0°-7° outward radial flow direction, which was attributed to the flow avoiding the spinner cone just upstream of the measurement plane. The distorted test results showed relatively strong radial flow localized to the tightly wound vortex feature in the swirl distortion profile.

Comparing the two conditions was accomplished by calculating the difference between distorted and clean test conditions (Equation 4.1). This method of comparison conserved the directionality of distorted test results as an increase or decrease from the clean test results.

$$\Delta\alpha = \alpha_{distorted} - \alpha_{clean} \tag{4.1}$$

From the plotted deviations, the StreamVane was found to contribute significant swirl in the region of the tightly wound vortex. This location was clearly outlined by the alternating radial flow angles from 90-150° fanwise from top-dead-center. The center of the vortex appeared to have convected in the fanwise direction from 90°, as designed, to approximately 120° at the fan inlet plane. This vortex movement was attributed to the co-rotating bulk swirl, fan spinner cone influence and the requirement of flow avoidance of the solid body, and fan rotor dynamics interacting slightly upstream of the fan blades. The radial flow angle in the bulk swirl region was relatively unchanged between the clean and distorted test results.

4.3.3 Tangential Flow Angle

The tangential flow angle results at the fan rotor inlet plane (Station 1.0) are summarized in Figure 4.8. The tangential flow angle measurements are presented positively fanwise (anti-clockwise), forward-looking-aft, and use the key found in lower right corner of the figure to illustrate the relative StreamVane position. The clean test results revealed negligible tangential flow at the fan inlet plane. The distorted test results showed relatively strong tangential flow, on the order of ±30°, localized to the tightly wound vortex feature in the swirl distortion profile, as well as substantial fanwise flow (co-swirl), on the order of +10°, in the co-rotating bulk swirl region.

Comparing the two conditions was accomplished by calculating the difference between distorted and clean test conditions (Equation 4.2). This method of comparison conserved the directionality of distorted test results as an increase or decrease from the clean test results.

$$\Delta\beta = \beta_{distorted} - \beta_{clean} \tag{4.2}$$

From the plotted deviations, the StreamVane was found to contribute significant swirl in the region of the tightly wound vortex. This location was clearly outlined by the alternating tangential flow angles from 90-150° fanwise from top-dead-center. Similar to the radial flow angle results, the center of the vortex appeared to have convected in the fanwise direction from 90° as designed to approximately 120° at the fan inlet plane. This vortex movement was attributed to the co-rotating bulk swirl (on the order of 10°), viscous effects of the fan spinner cone, and fan rotor dynamics interacting slightly upstream of the fan blades.

4.3.4 Flow Total Pressure

Figure 4.9 displays the Station 1.0 total pressure profiles at the two test conditions. The total pressure measurements were normalized by the atmospheric pressure and presented as percent recovery factors for the inlet duct and swirl profile. The resulting total-to-atmospheric pressure ratio at the fan rotor inlet plane under distorted test conditions was found to be relatively unchanged from clean inlet conditions. The difference between distorted test results and clean test results was calculated using Equation 4.3 and demonstrates the effect of swirl distortion on the total pressure field at the fan inlet plane.

$$\frac{\Delta p_0}{p_{atm}} = \left(\frac{p_{0_{distorted}} - p_{0_{clean}}}{p_{atm}}\right)\% \tag{4.3}$$

The total pressure recovery factor from the StreamVane distortion device was discovered to be very high, greater than 97%. This result was significant. By maintaining high relative inlet total pressure, the StreamVane was found to not appreciably affect the total pressure profile; therefore, the swirl distortion testing was effectively decoupled from the total pressure distortions common

to actual turbofan inlet ducts. This result also fulfilled a research goal of isolating a unique swirl distortion and measuring the fan response without the presence of significant total pressure distortions.

4.3.5 Flow Static Pressure

Figure 4.10 displays the Station 1.0 static pressure profiles at the two test conditions. The static pressure measurements were normalized by the atmospheric pressure and presented as a percentage. The resulting static-to-atmospheric pressure ratio at the fan inlet plane under distorted test conditions showed reductions from clean test results throughout the measurement domain with a localized exception near the bottom-dead-center of the profile. The difference between distorted test results and clean test results was calculated using Equation 4.4 and demonstrates the effect of swirl distortion on the static pressure field at the fan inlet plane.

$$\frac{\Delta p}{p_{atm}} = \left(\frac{p_{distorted} - p_{clean}}{p_{atm}}\right)\% \tag{4.4}$$

From the comparison, the static pressure in the majority of the measurement domain generally decreased when experiencing swirl distortion inlet conditions. Significant static pressure reduction was measured in the location of the tightly-wound vortex feature centered at 120° fanwise from top-dead-center. This result was due to the strong tightly-wound vortex feature and locally high magnitudes of secondary flow in this region. Alternatively, in areas of weak distortion, the static pressure was discovered to be nearly equal to the clean test results.

4.3.6 Flow Mach Number

Due to the negligible changes in total pressure and the relatively small changes in static pressure between the two test conditions, changes in the Mach number were found to be negligible. The resulting calculated Mach number of the flow at Station 1.0 averaged 0.30±0.02 across the entire measurement domain, regardless of clean or distorted test conditions. [Flow Mach number results for Station 1.0 are included in Appendix C.]

4.3.7 Flow Total Temperature

Because no work was performed on the flow in the inlet duct, the flow total temperature measured at the fan inlet (Station 1.0) was within 99% of ambient atmospheric temperature. The deviation between distorted and clean test conditions was found to be within ±0.20%. This result was well within the instrument uncertainty of the thermocouple system, and was considered insignificant. [Flow total temperature results for Station 1.0 are included in Appendix C.]

4.3.8 Flow Static Temperature

The static temperature is a calculated parameter based on the flow Mach number and the total temperature of the flow. Citing negligible changes in both Mach number and total temperature under each test condition, the changes in static temperature were also determined to be negligible regardless of clean or distorted test conditions. In fact, the static temperature at Station 1.0 was measured to be within 98% of ambient atmospheric temperature, with a deviation between test conditions within ±1%. [Flow static temperature results for Station 1.0 are included in Appendix C.]

4.3.9 Secondary Flow Velocity Profile

Although the Mach number and the static temperature were not significantly altered by the distortion profile, the measured values were critical in determining the secondary flow velocity profile at Station 1.0. Figure 4.11 illustrates the two-dimensional secondary flow velocity profile normalized by the maximum three-dimensional bulk velocity magnitude (Equation 4.5). In the figure, the StreamVane distortion device contributes to a significant increase in secondary flow with additionally augmented effects in the region of the tightly-wound vortex feature.

$$\frac{C_{r\theta}}{\max(C_{r\theta z})} = \left(\frac{\sqrt{C_r^2 + C_\theta^2}}{\max\left(\sqrt{C_r^2 + C_\theta^2 + C_z^2}\right)} \right)\% \tag{4.5}$$

Comparing the two test conditions was accomplished by calculating the difference between distorted and clean results (Equation 4.6).

$$\Delta\left(\frac{C_{r\theta}}{\max(C_{r\theta z})}\right) = \left(\left(\frac{C_{r\theta}}{\max(C_{r\theta z})}\right)_{distorted} - \left(\frac{C_{r\theta}}{\max(C_{r\theta z})}\right)_{clean}\right)\% \tag{4.6}$$

The secondary flow profile produced by the StreamVane was discovered to account for up to nearly 40% of the maximum through flow velocity magnitude. This result indicated that a substantial amount of the fluid motion was within the two-dimensional measurement plane, perpendicular to the engine axis. Interestingly, the distorted secondary flow magnitude in small regions of the flow field decreased when compared to the clean results, especially near the innermost measurement radii. A possible reason behind this phenomenon is mass flow redistribution in the mixing/swirling flow produced by the StreamVane. Unfortunately, the five-hole three-dimensional flow probe used throughout this investigation was geometrically restricted from advancing closer to the spinner to determine whether this result was due to core effects.

4.3.10 Supporting Figures

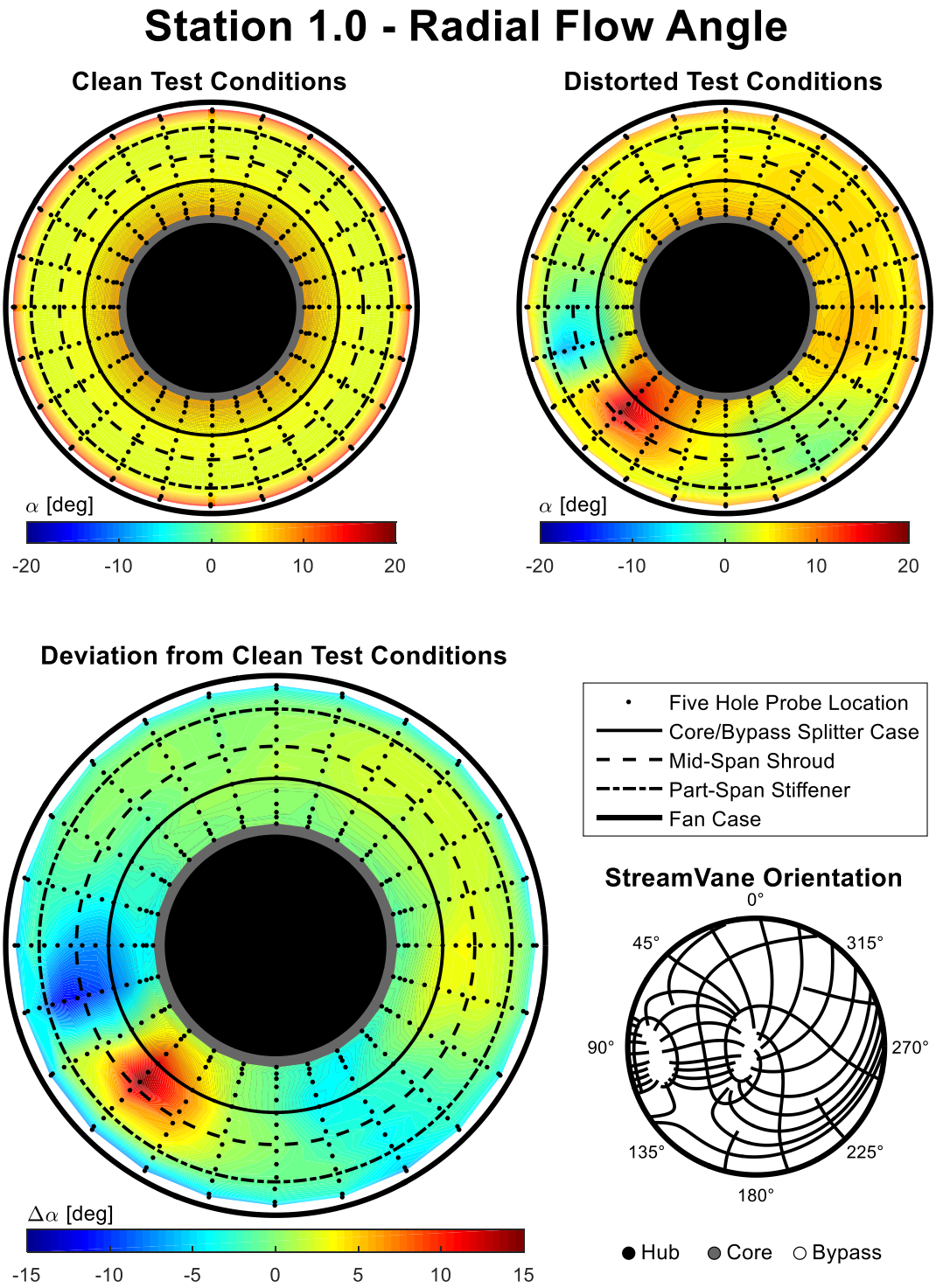

Figure 4.7: Station 1.0 Radial Flow Angle Results

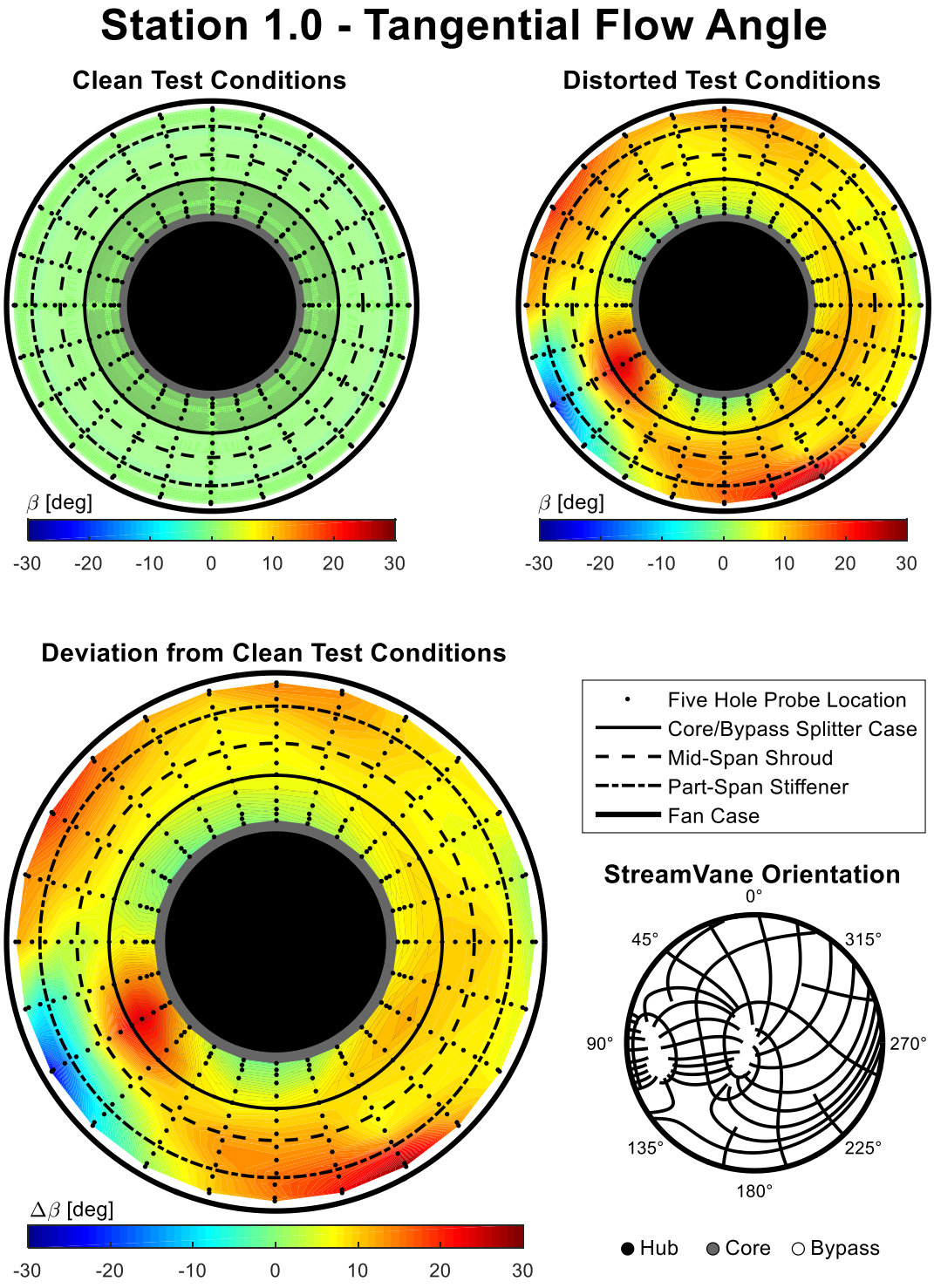

Figure 4.8: Station 1.0 Tangential Flow Angle Results

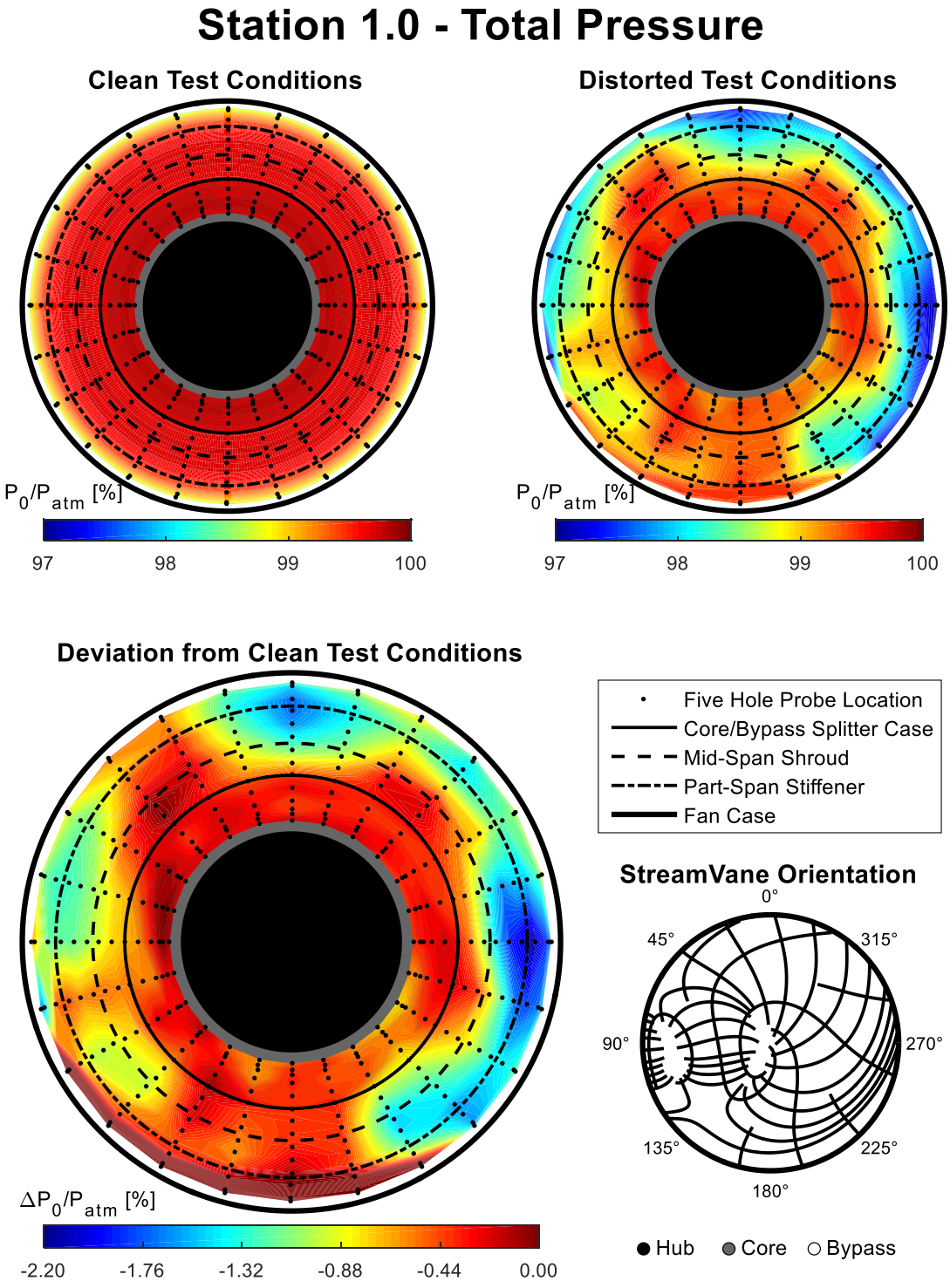

Figure 4.9: Station 1.0 Total Pressure Results

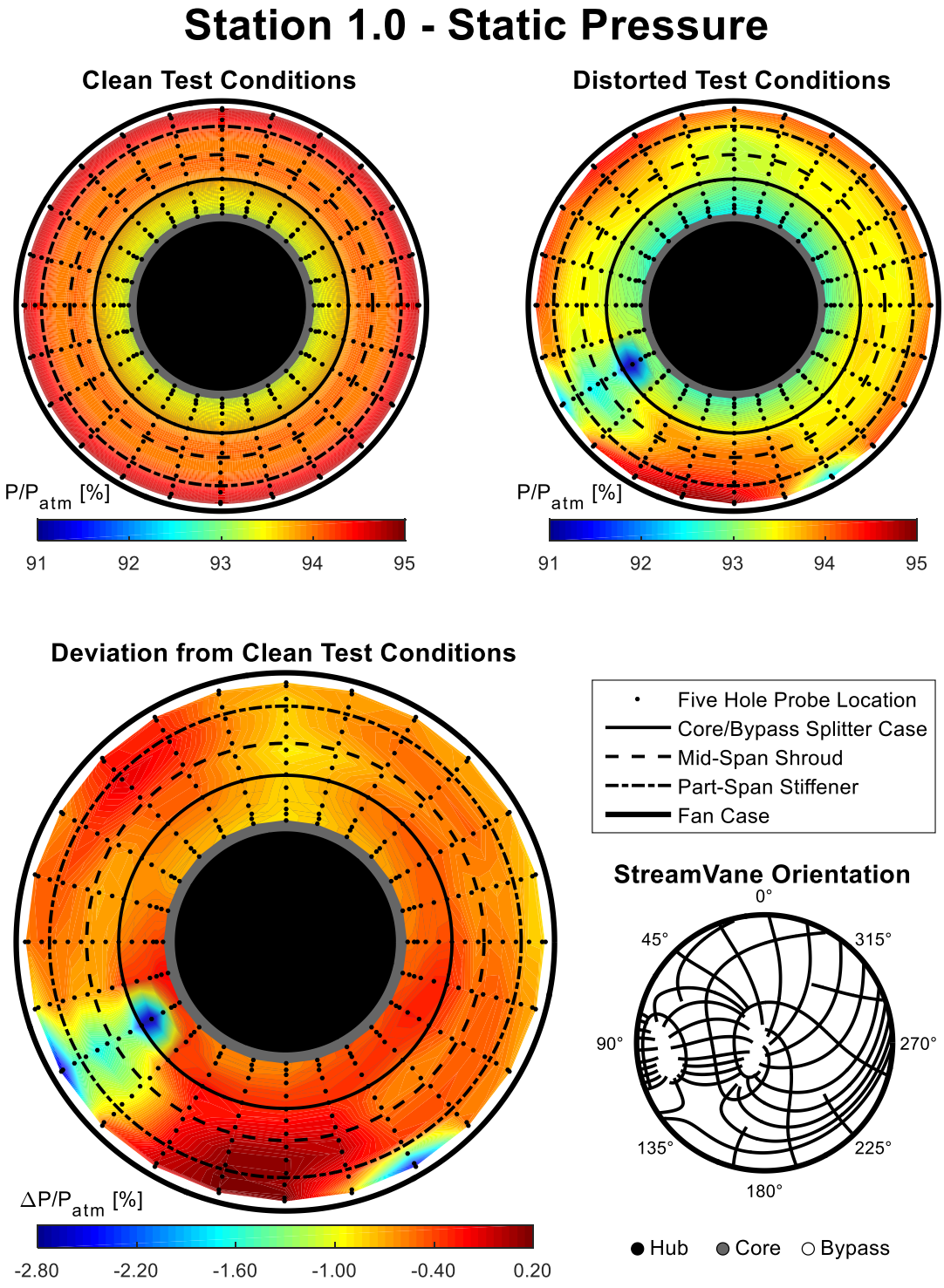

Figure 4.10: Station 1.0 Static Pressure Results

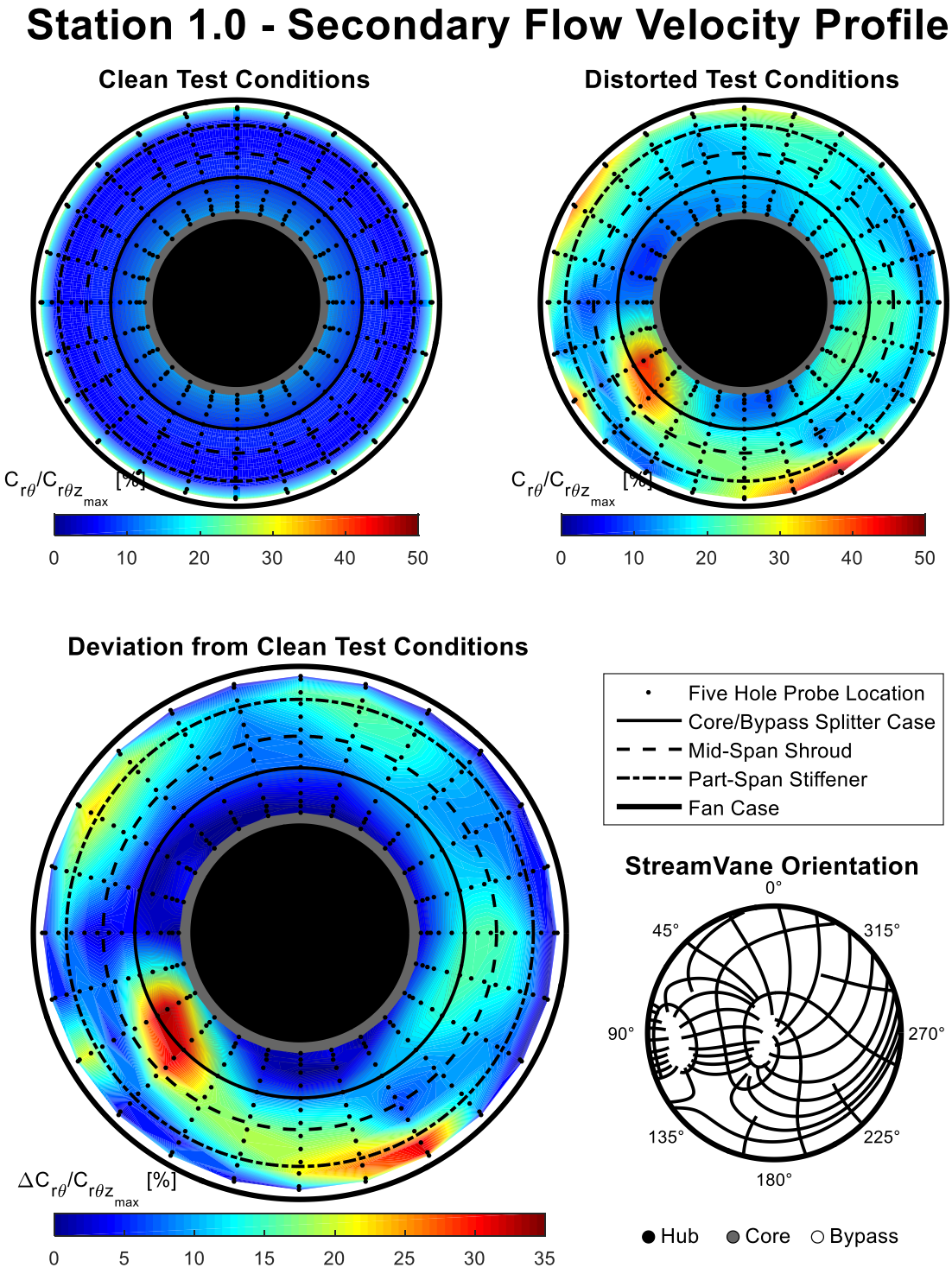

Figure 4.11: Station 1.0 Secondary Flow Velocity Profile Results

4.4 Station 1.5 – Fan Rotor Outlet Results

4.4.1 Overview

This section presents the flow conditions measured at Station 1.5, immediately downstream of the fan rotor trailing edge. The data presented in the subsequent plots is the test-to-test average results from five repeated tests at a single, constant fan speed. Clean and distorted test results are presented for side-by-side comparison. When applicable, the deviations from clean results are also calculated and provided. In an attempt to efficiently and effectively present the data, all supporting figures can be found in Section 4.4.10 following the discussion of each individual parameter in Sections 4.4.2 – 4.4.9.

All results are presented forward-looking-aft (FLA) with the fan angle beginning at top-dead-center and progressing anti-clockwise in the direction of fan rotation.

4.4.2 Radial Flow Angle

The radial flow angle results at the fan rotor outlet plane (Station 1.5) are summarized in Figure 4.12. The radial flow angle measurements are presented positively outward from engine centerline, forward-looking-aft, and use the key found in lower right corner of the figure to illustrate the relative StreamVane position. The clean test results revealed a slight radial outward flow direction of approximately 5° propagating from engine centerline. The distorted test results showed significant outward radial flow at the core/bypass splitter case. The hub-ward radial flow, coupled with the tip-ward radial flow at approximately 120° and 165° fanwise from top-dead-center, respectively, indicated evidence that the tightly-wound vortex persisted downstream of the fan rotor. Additionally, the center of the vortex appeared to have convected from approximately 90°, as designed, to approximately 135° in the fanwise direction. This additional vortex movement was attributed to the fan influence on the flow with the possible contribution of bulk swirl rotation effects.

In both clean and distorted tests, the radial flow direction exiting the fan was influenced by the fan and engine geometry. Large gradients in radial flow direction at the core/bypass splitter case and the mid-span shroud feature on the fan blades indicated that the in-plane flow was obstructed and redirected by these engine features.

Comparison of the two test conditions was accomplished by revisiting Equation 4.1 and calculating the difference between distorted and clean results. This method of comparison conserved the directionality of distorted test results as an increase or decrease from the clean test results.

$$\Delta\alpha = \alpha_{distorted} - \alpha_{clean} \tag{4.1}$$

From the plotted deviations, effects of the tightly-wound vortex contributed to significant distortions in the fan outlet radial flow direction. The radial flow angle in the bulk swirl region was relatively unchanged between the clean and distorted test results.

4.4.3 Tangential Flow Angle

The tangential flow angle results at the fan rotor outlet plane (Station 1.5) are summarized in Figure 4.13. The tangential flow measurements are presented positively fanwise (anti-clockwise), forward-looking-aft, and use the key found in lower right corner of the figure to illustrate the relative StreamVane position. The clean test results revealed nearly uniform tangential flow direction exiting the fan rotor, averaging approximately 47°±2°. The distorted test results showed relatively uniform tangential flow angle augmentation in the bulk swirl region of the distortion profile, with strong clockwise rotating flow in the location of the tightly-wound vortex. Additionally, the center of the vortex appeared to have convected from approximately 90°, as designed, to approximately 135° in the fanwise direction. This vortex movement was attributed to the fan influence on the flow with the possible contribution of bulk swirl rotation effects.

Comparison of the two test conditions was accomplished by revisiting Equation 4.2 and calculating the difference between distorted and clean results. This method of comparison conserved the directionality of distorted test results as an increase or decrease from the clean test results.

$$\Delta\beta = \beta_{distorted} - \beta_{clean} \tag{4.2}$$

The deviation from clean test results indicated that the co-rotating flow in the bulk swirl region and the co-rotating flow in one half of the tightly wound vortex produced increased tangential flow angle exiting the fan on the order of +5°. The increased measured flow angle, coupled with the fan rotation, likely contributed to the tightly wound vortex convection at the fan outlet. In the region of the tightly-wound vortex associated with anti-fanwise flow direction, a -10° reduction in tangential flow angle exiting the fan was discovered.

4.4.4 Flow Total Pressure

Figure 4.14 displays the Station 1.5 total pressure profiles at the two test conditions. The total pressure measurements were normalized by the atmospheric pressure and presented as percentages. In both the clean and distorted test results, the fan rotor outlet total-to-atmospheric pressure ratio increased with blade radius. This increase in pressure ratio progressing outward form engine centerline was attributed to increasing blade speed and therefore work input to the flow.

The difference between distorted test results and clean test results was calculated using Equation 4.3 and demonstrates the effect of swirl distortion on the total pressure field at the fan outlet plane.

$$\frac{\Delta p_0}{p_{atm}} = \left(\frac{p_{0_{distorted}} - p_{0_{clean}}}{p_{atm}}\right)\% \tag{4.3}$$

In general, the swirl distortion contributed to a global deficit of approximately 1.5% in the resulting total pressure of the flow exiting the fan rotor. The deviation from clean results indicated that the co-rotating, bulk swirl flow field reduced the pressure rise across the fan. Interestingly, the effects of the tightly-wound vortex feature of the inlet swirl profile produced negligible differences in the total pressure field downstream of the fan rotor. Also, the co-swirling flow did not produce measureable effects at the outermost radii, where the measured total pressure under distorted test conditions was equal to the measured total pressure under clean test conditions.

4.4.5 Flow Static Pressure

Figure 4.15 displays the Station 1.5 static pressure profiles at the two test conditions. The static pressure measurements were normalized by the atmospheric pressure and presented as a percentage. In both the clean and distorted test results, the static pressure generally increased radially outward from engine centerline while maintaining relatively small changes circumferentially. The difference between distorted test results and clean test results was calculated using Equation 4.4 and demonstrates the effect of swirl distortion on the static pressure field at the fan outlet plane.

$$\frac{\Delta p}{p_{atm}} = \left(\frac{p_{distorted} - p_{clean}}{p_{atm}}\right)\% \tag{4.4}$$

Comparing the distorted results to the clean results immediately revealed that the swirl distortion contributed to negligible changes to the static pressure field entering the core of the turbofan engine. In the bypass region, the swirl distortion contributed to a nearly uniform 2% deficit in static pressure; however, the local effects of the tightly-wound vortex (centered at approximately 135° fanwise from top-dead-center) appeared to have negated the static pressure changes. In this region, no measureable static pressure changes were measured between clean and distorted results.

4.4.6 Flow Mach Number

Citing small deviations in the total pressure and static pressure of the flow exiting the fan between clean and distorted test conditions, the variation in Mach number was found to be negligible. The Mach number varied radially with blade geometry appearing to have small effects on the calculated value; however, this result was constant regardless of test conditions. Overall, the Mach number at Station 1.5 averaged approximately 0.45, with less than ±2% variation, regardless of clean or distorted test conditions. [Flow Mach number results for Station 1.5 are included in Appendix D.]

4.4.7 Flow Total Temperature

A total temperature increase of approximately 3% above ambient was measured at the fan rotor outlet (Station 1.5). This result was nearly uniform across the measurement domain with slightly elevated values measured entering the core of the turbofan engine. The deviation between distorted and clean inlet conditions was found to be within ±2% and was considered an insignificant result of the swirl distortion profile. [Flow total temperature results for Station 1.5 are included in Appendix D.]

4.4.8 Flow Static Temperature

The static temperature is a calculated parameter based on the flow Mach number and the total temperature of the flow. Citing negligible changes in both Mach number and total temperature under each test condition, the changes in static temperature were also determined to be negligible, regardless of test conditions. In fact, the static temperature at Station 1.5 was measured to be within 96% ambient atmospheric temperature, with a deviation between test conditions within ±1.5%. [Flow static temperature results for Station 1.5 are included in Appendix D.]

4.4.9 Secondary Flow Velocity Profile

Although the Mach number and the static temperature were not significantly altered by the distortion profile, the measured values were critical in determining the secondary flow velocity profile at Station 1.5. Figure 4.16 illustrates the two-dimensional secondary flow velocity profile normalized by the maximum three-dimensional bulk velocity magnitude (Equation 4.5).

$$\frac{C_{r\theta}}{\max(C_{r\theta z})} = \left(\frac{\sqrt{C_r^2 + C_\theta^2}}{\max\left(\sqrt{C_r^2 + C_\theta^2 + C_z^2}\right)} \right)\% \tag{4.5}$$

Under clean test conditions, the secondary flow exiting the fan was nearly radially uniform with marginal increases near the mid-span shroud. The distorted test conditions resulted in nearly identical radial variations with exception to the tightly-wound vortex. In this location, the reversed flow contributed to reduced secondary flow magnitudes. Comparing the two test conditions was accomplished by calculating a difference between distorted and clean results (Equation 4.6).

$$\Delta\left(\frac{C_{r\theta}}{\max(C_{r\theta z})}\right) = \left(\left(\frac{C_{r\theta}}{\max(C_{r\theta z})}\right)_{distorted} - \left(\frac{C_{r\theta}}{\max(C_{r\theta z})}\right)_{clean}\right)\% \tag{4.6}$$

The calculated differences in secondary flow magnitude from clean test results were generally small. In the bulk swirl region, the secondary flow increased marginally which was attributed to the elevated tangential flow in this region. The secondary flow velocity profile local to the tightly-wound vortex was discovered to have significant differences from clean test results. The flow reversal from the fanwise direction in this area contributed to large deficits in secondary flow when compared to clean conditions.

4.4.10 Supporting Figures

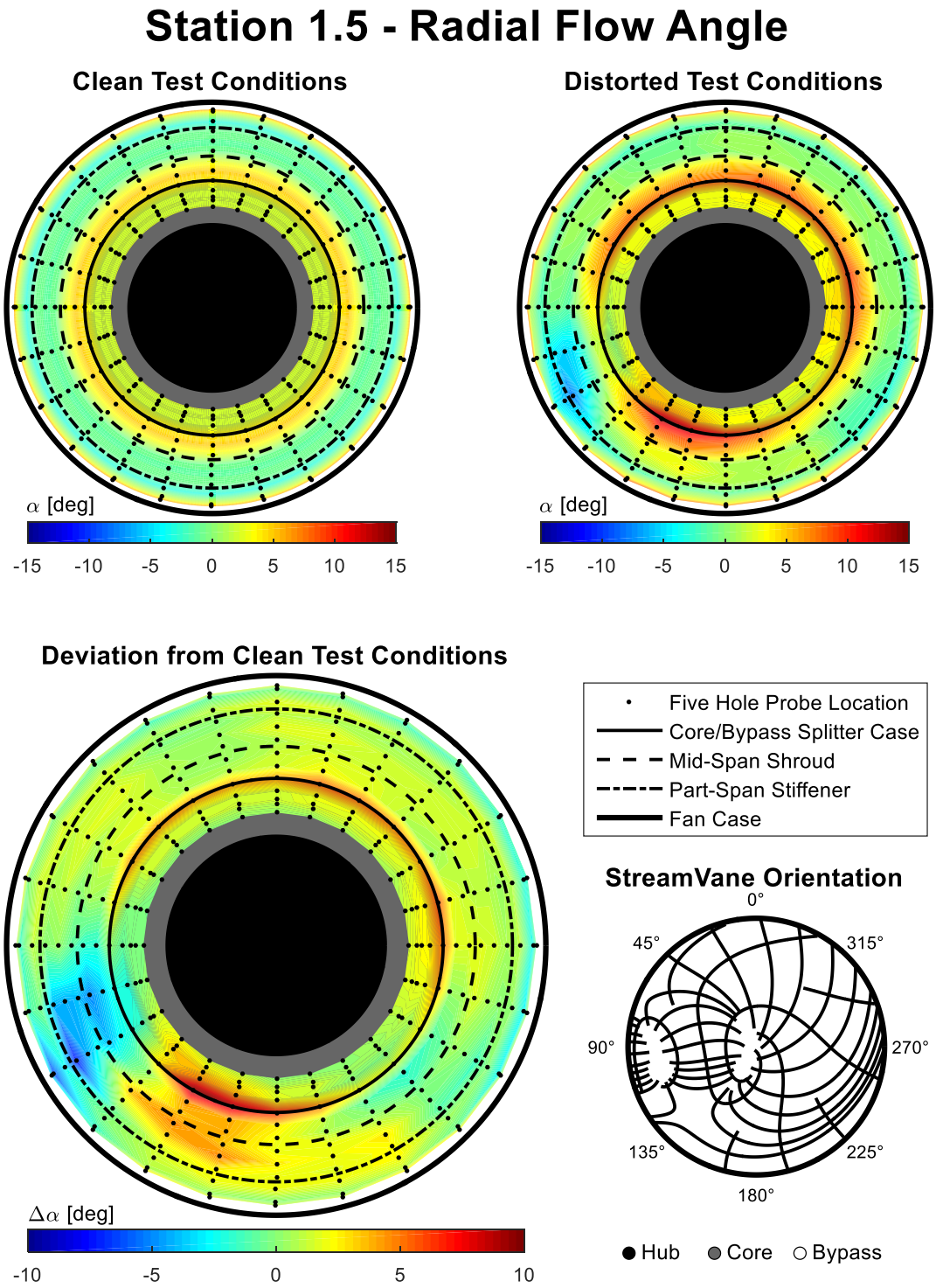

Figure 4.12: Station 1.5 Radial Flow Angle Results

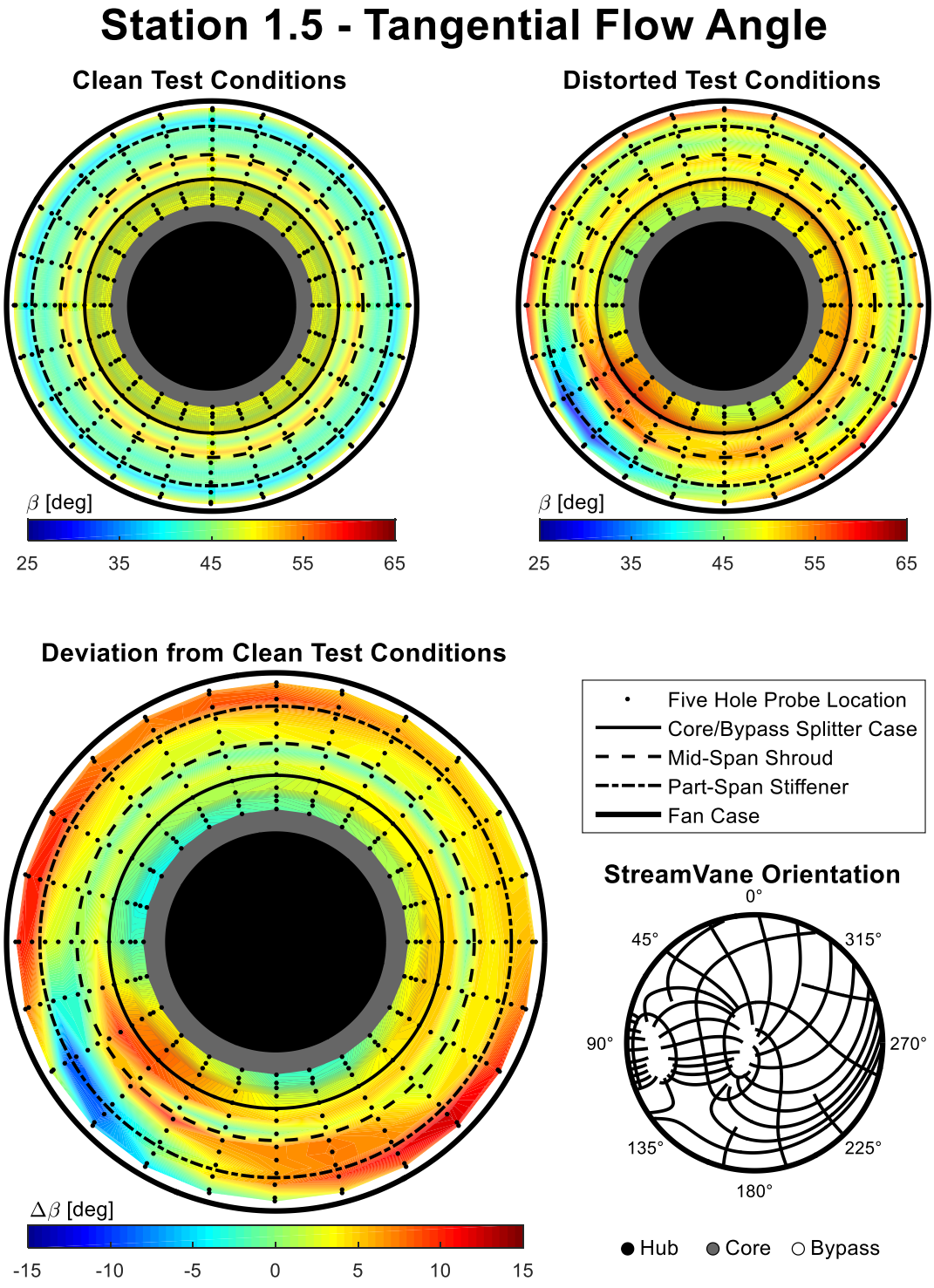

Figure 4.13: Station 1.5 Tangential Flow Angle Results

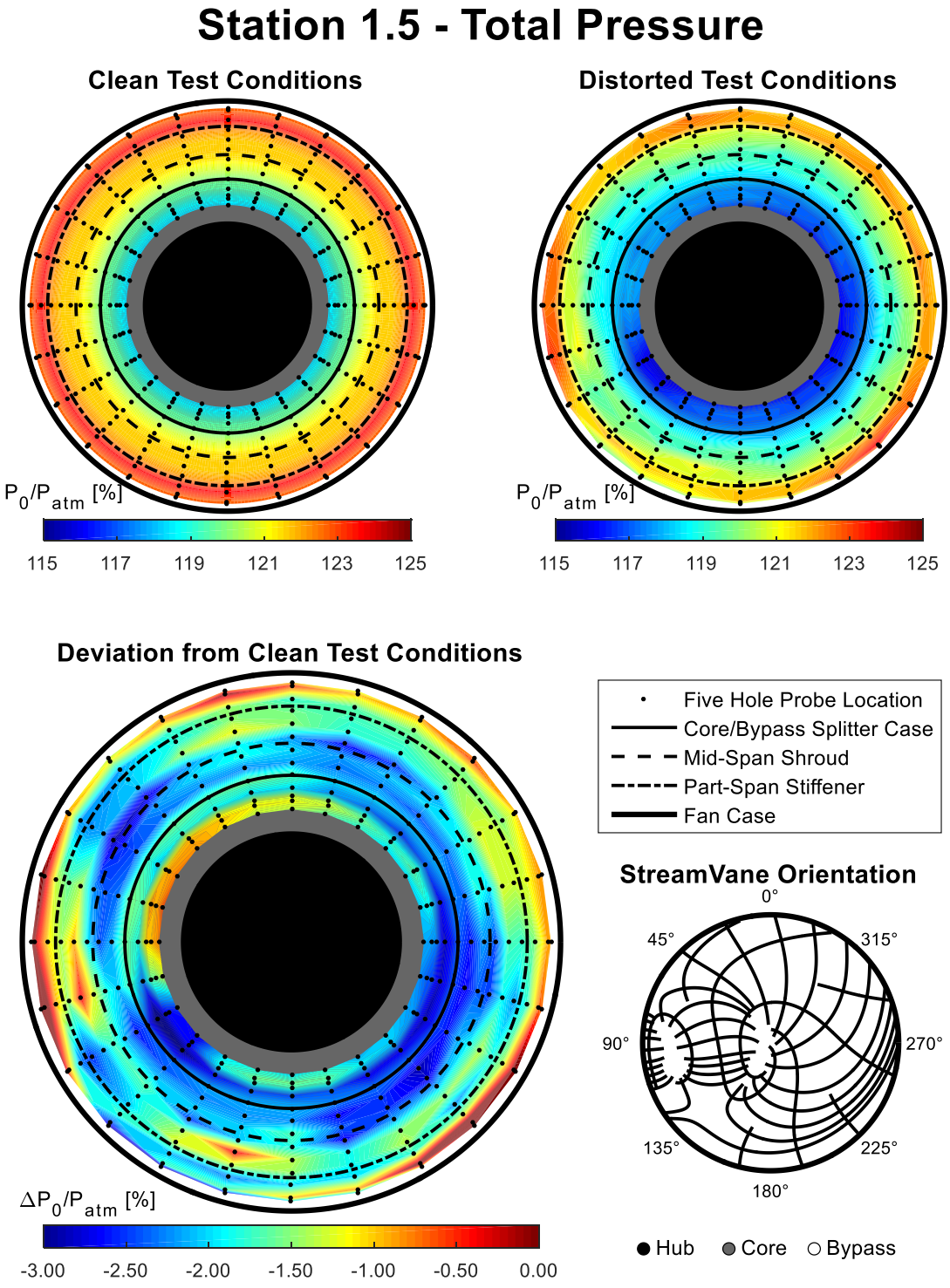

Figure 4.14: Station 1.5 Total Pressure Results

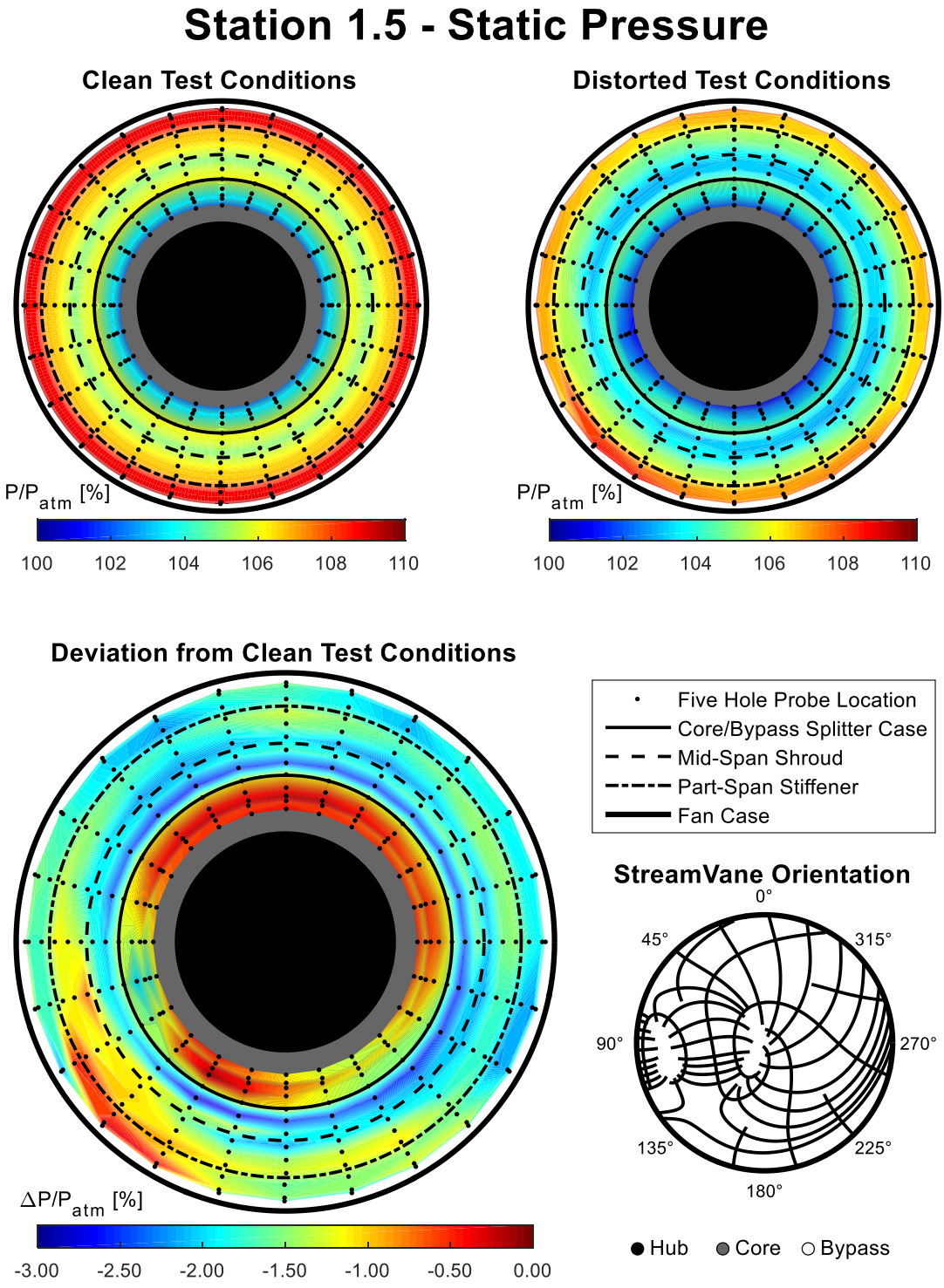

Figure 4.15: Station 1.5 Static Pressure Results

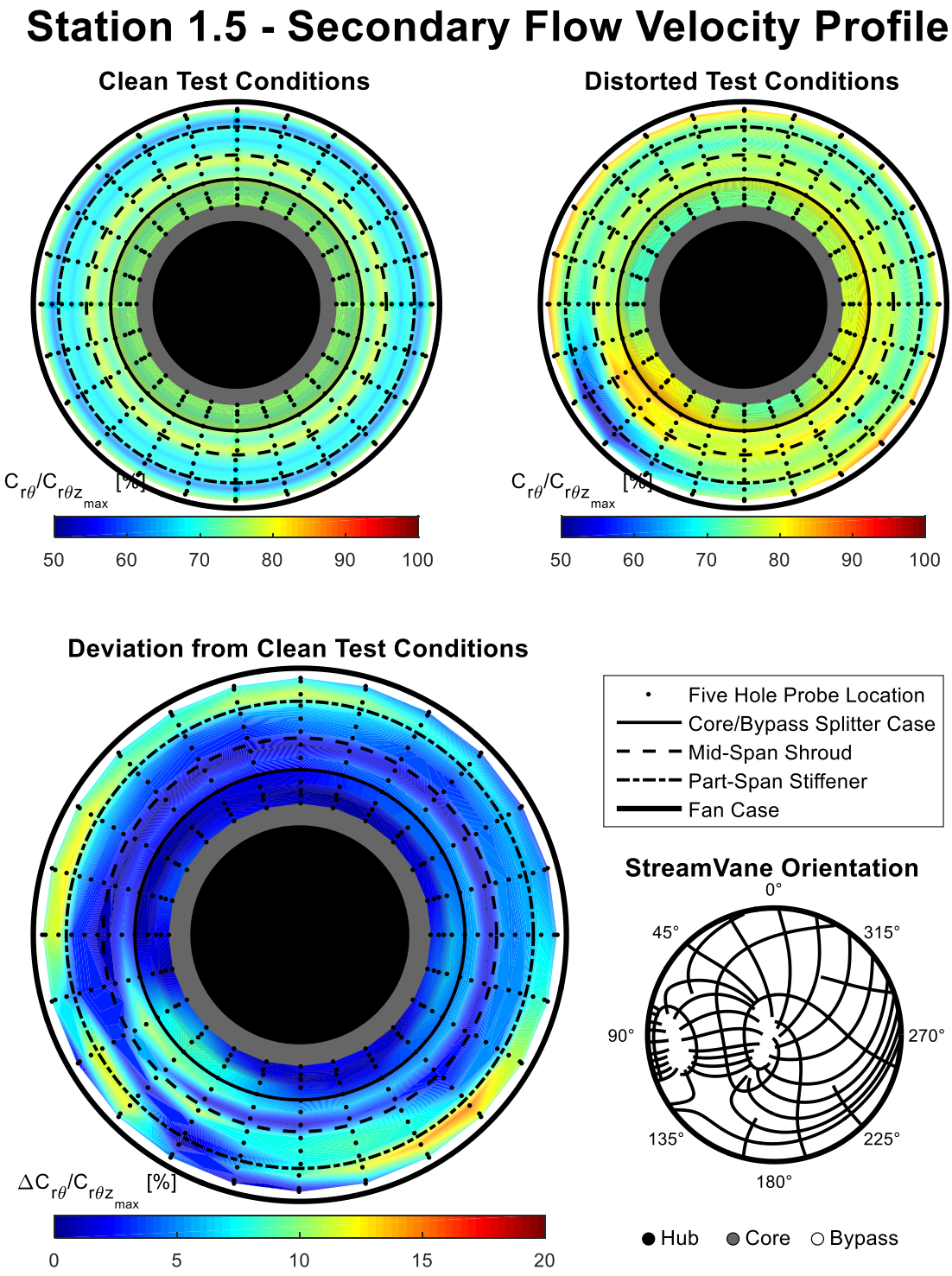

Figure 4.16: Station 1.5 Secondary Flow Velocity Profile Results

Chapter 5 – Summary and Conclusions

5.1 Summary of Findings

5.1.1 Overview

Of the many outcomes from the investigation of inlet swirl distortion discussed in the previous chapter, several significant results emerged that best define the inlet/fan interactions and the persistence of swirl distortion through the fan rotor. The radial flow angle, tangential flow angle, and secondary flow velocity profiles provided the best sources of comparison from the designed upstream inlet distortion profile, to the fan inlet measurement plane, to the fan outlet measurement plane.

The following section summarizes the significant results of flow angle and secondary flow velocity profile at three discrete planes within the engine inlet: The StreamVane Plane, The Station 1.0 Plane, and The Station 1.5 Plane. The StreamVane Plane was defined as the CFD results utilized to generate the StreamVane profile and was located theoretically two fan diameters upstream of the fan rotor leading edge. The Station 1.0 and Station 1.5 planes were the experimental results from this investigation and were located within inches of fan rotor leading and trailing edges, respectively. These experimental measurement planes isolated the fan rotor to best capture the interactions of the swirl distortion and the engine component.

All results are presented forward-looking-aft (FLA) with the fan angle beginning at top-dead-center and progressing anti-clockwise in the direction of fan rotation. The Station 1.0 and Station 1.5 experimental results presented are the calculated deviations from clean test conditions in the presence of the StreamVane distortion device. By removing the clean test results from the distorted test results, only the effects of the swirl distortion remained. This was important in determining the off-design nature of the resulting flow parameters.

5.1.2 Comparison of Radial Flow Angles

The radial flow angle is a measure of the local three dimensional velocity field projected in the two dimensional plane perpendicular to the engine axis with respect to the radial direction. By measuring and comparing the magnitude of the radial flow angle at two streamwise planes in the engine inlet, the magnitude of secondary flow in the radial direction was monitored through the

fan rotor. Figure 5.1 shows the measured radial flow angle deviations entering and exiting the fan rotor referenced to the CFD results that were utilized to generate the StreamVane distortion device. Due to the large differences in ranges of radial flow angle between the data planes, the scale of the contour plots was changed so as to capture the most information at each plane and to best represent the structure of the flow field.

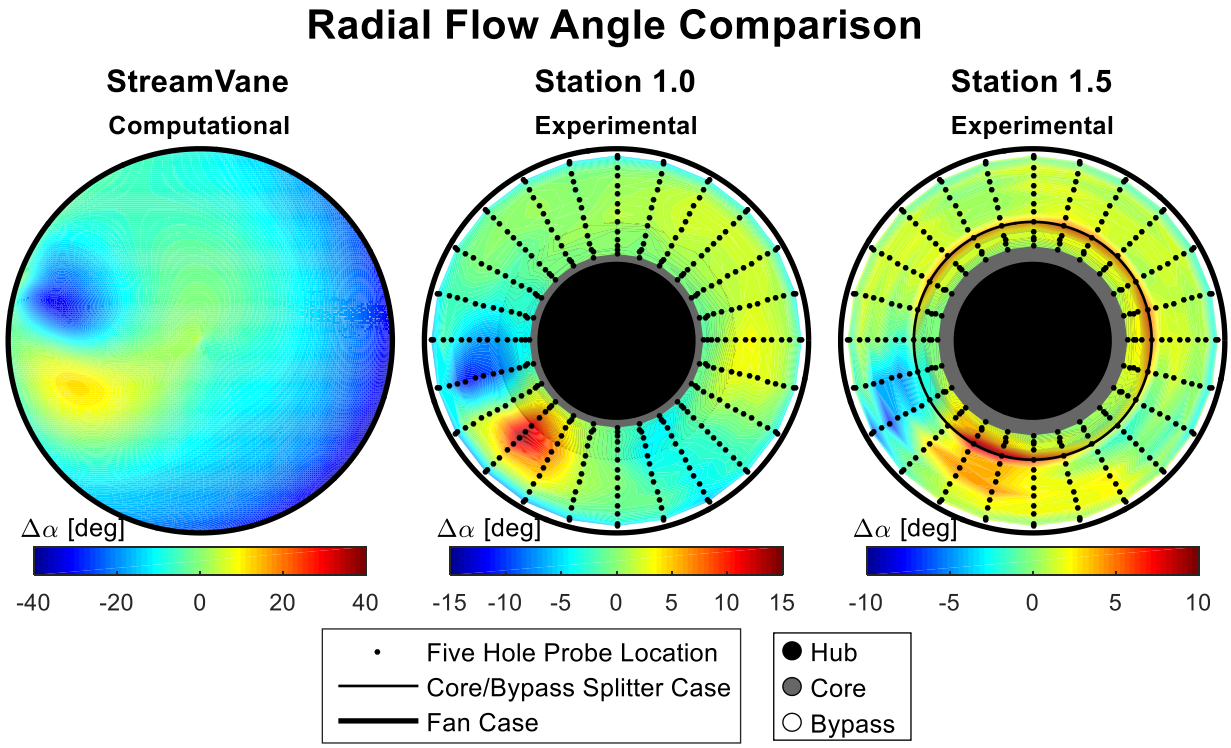

Figure 5.1: Comparison of Radial Flow Angle Results

The fanwise procession of the tightly-wound vortex feature was immediately evident. The center of the vortex initialized at 90° anti-clockwise from top-dead-center, convected fanwise approximately 30° before entering the fan rotor, and terminated an additional 15° further fanwise after exiting the fan rotor. Between the StreamVane plane and Station 1.0, the vortex movement was attributed to the co-rotating bulk swirl interacting with the counter-rotation vortex. The vortex movement found in the Station 1.5 results was attributed to the fanwise procession through the rotor and the blade interaction with the relatively small distortion feature.

The extent of the distortion remained constant between the StreamVane and Station 1.0 planes based on the size of the tightly-wound vortex signature. After passing through the fan, the extent of the distortion spread circumferentially. This result was related to the vortex maintaining a defined structure until it interacted with the fan rotor, the fan rotor then dissipated the tightly-wound vortex over a broader extent.

The various scales used for each measurement plane show a reduction in the intensity, or strength, of the distortion. The highest magnitudes of radial flow angle from the StreamVane plane were reduced to at least half the initial values before the distortion entered the fan at Station 1.0. This result was due to swirl dissipation in the connecting duct between the StreamVane outlet and the

fan rotor inlet planes. Less significant reductions were measured in swirl intensity between the Station 1.0 and Station 1.5 results. At Station 1.5, the core/bypass splitter case influenced the radial flow, as seen in the large radial flow angle gradients surrounding the splitter case.

5.1.3 Comparison of Tangential Flow Angles

The tangential flow angle is a measure of the local three dimensional velocity field projected in the two dimensional plane perpendicular to the engine axis with respect to the circumferential direction. By measuring and comparing the magnitude of the tangential flow angle at two streamwise planes in the engine inlet, the magnitude of secondary flow in the radial direction was monitored through the fan rotor. Figure 5.2 shows the measured tangential flow angle deviations entering and exiting the fan rotor referenced to the CFD results that were utilized to generate the StreamVane distortion device. Due to the large fluctuations in ranges of tangential flow angle between the data planes, the scale of the contour plots was changed so as to capture the most information at each plane and to best represent the structure of the flow field.

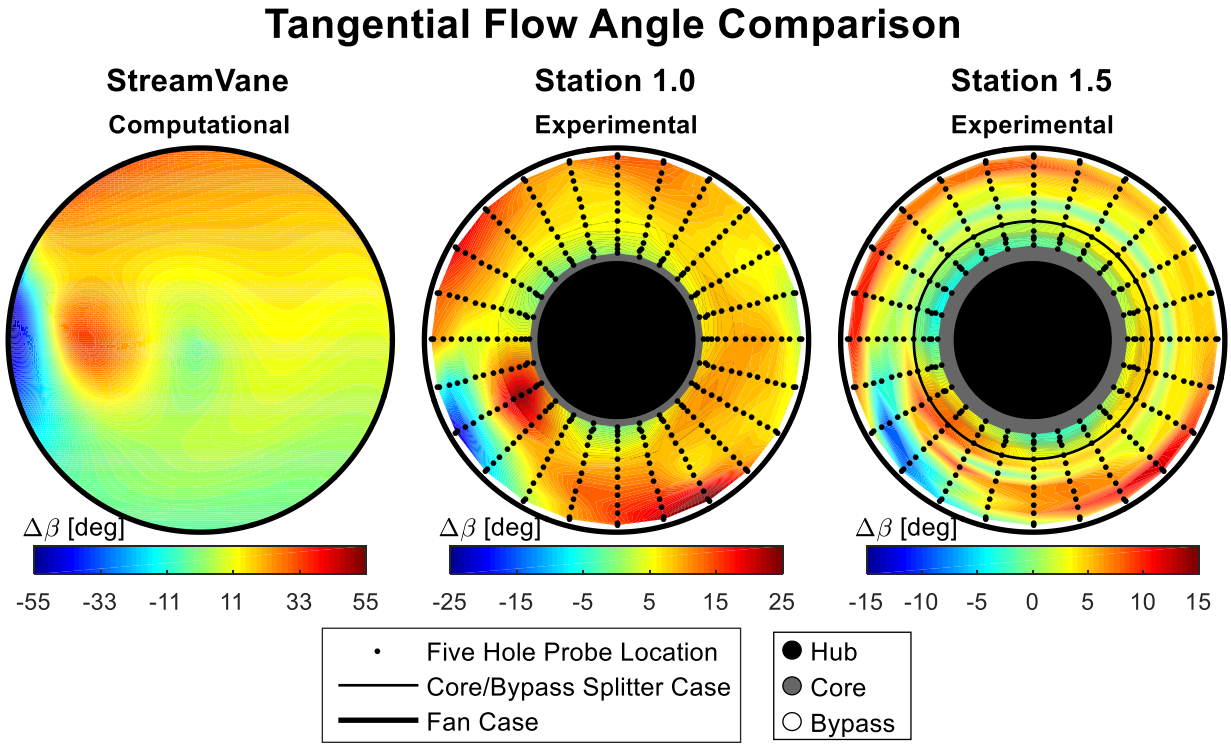

Figure 5.2: Comparison of Tangential Flow Angle Results

The fanwise procession of the tightly-wound vortex feature was immediately evident. Identical to the radial flow angle results, the center of the vortex initialized at 90° anti-clockwise from top-dead-center, convected fanwise approximately 30° before entering the fan rotor, and terminated an addition 15° further fanwise after exiting the fan rotor. Between the StreamVane plane and Station 1.0, the vortex movement was attributed to the co-rotating bulk swirl interacting with the counter-rotation vortex. The vortex movement found in the Station 1.5 results was attributed to

the fanwise procession through the rotor and the blade interaction with the relatively small distortion feature.

The extent of the distortion remained constant between the StreamVane and Station 1.0 planes based on the size of the tightly-wound vortex signature. After passing through the fan, the extent of the distortion spread circumferentially in the fanwise direction. This result was related to the vortex maintaining a defined structure until it interacted with the fan rotor, the fan rotor then dissipated the tightly-wound vortex over a broader extent.

The various scales used for each measurement plane show a reduction in the intensity, or strength, of the distortion. The highest magnitudes of tangential flow angle from the StreamVane plane were reduced to at least half the initial values before the distortion entered the fan at Station 1.0. This result was due to swirl dissipation in the connecting duct between the StreamVane outlet and the fan rotor inlet planes. Less significant reductions were measured in swirl intensity between the Station 1.0 and Station 1.5 results.

5.1.4 Comparison of Secondary Flow Velocity Profiles

The secondary flow velocity profile is a measure of the in-plane velocity magnitude of the flow field in a two dimensional plane perpendicular to the engine axis. This value served as a representation of the amount of non-axial flow in the inlet/fan subsystem. Figure 5.3 shows the calculated deviations of the measured distorted flow condition results compared to the clean flow condition results.

The difference between the two test conditions was normalized by the maximum through flow velocity magnitude, and plotted as an absolute value normalized deviation from clean according to Equation 5.1. The normalization and absolute value calculation allowed the three comparison planes to be analyzed on identical axes. Although directionality of the deviation was lost, the results from the radial and tangential flow angle analysis provided the missing information.

$$\left|\Delta \frac{C_{r\theta}}{\max(C_{r\theta z})}\right| = \left|\left(\frac{C_{r\theta}}{\max(C_{r\theta z})}\right)_{distorted} - \left(\frac{C_{r\theta}}{\max(C_{r\theta z})}\right)_{clean}\right| \% \qquad (5.1)$$

The secondary flow profile entering the fan rotor at Station 1.0 was very similar to the designed StreamVane distortion profile with the exception of the tightly-wound vortex feature. In the normalized plot for Station 1.0, the tightly-wound vortex showed augmented intensity compared to the remainder of the profile. Another important result for this plane was the bulk swirl levels compared to the StreamVane plane. Locally, up to 40% of the flow velocity profile entering the engine was off-engine-axis; this result was nearly identical to the CFD design plane.

As the fan processed the distortion and increased the axial velocity of the flow, a reduction in secondary flow was discovered. This was especially true in the core region where distorted results matched clean results and negligible deviations were found. The significant result at Station 1.5 was the continued appearance of strong secondary flow in the region of the tightly-wound vortex.

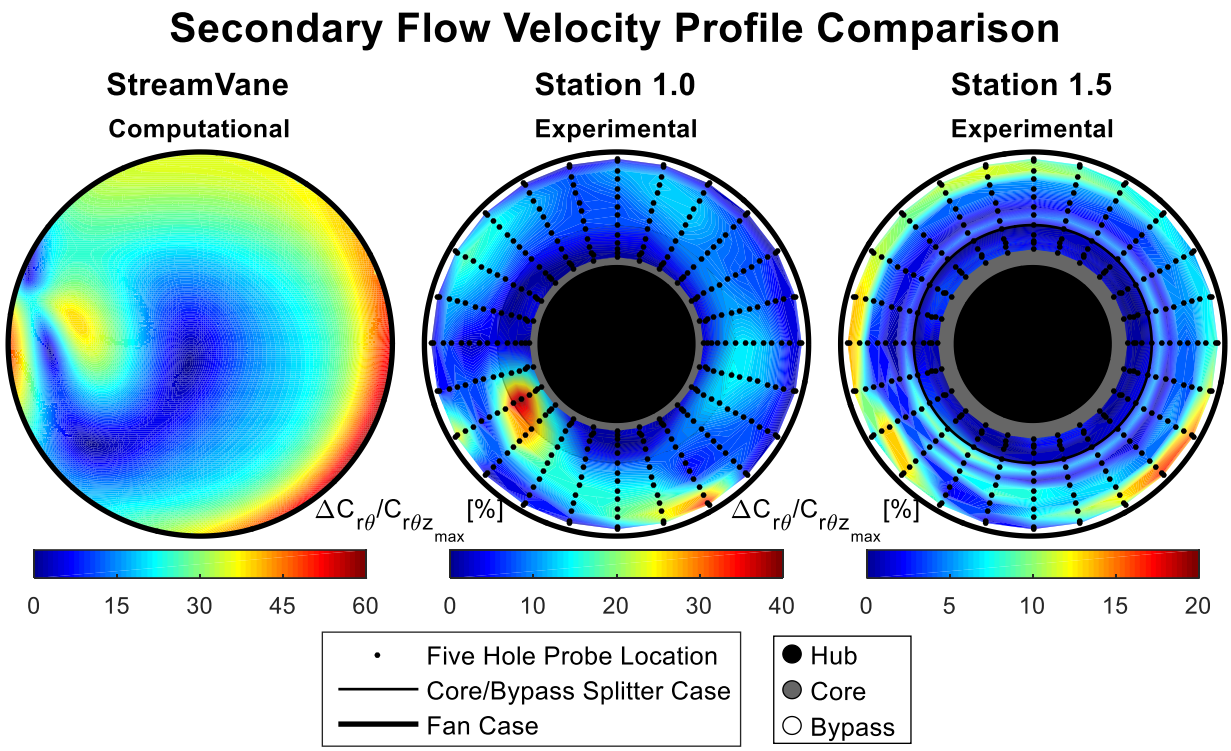

Figure 5.3: Comparison of Secondary Flow Velocity Profile Results

Because flow directionality was lost in Figure 5.3, the streamlines at each plane were calculated and displayed in Figure 5.4. The streamlines were calculated from the two-dimensional secondary flow distortions resulting after clean conditions were removed. Removing the clean results served as a form of background subtraction leaving only the off-design velocity streamlines. Without this calculation, the streamline structures would be effectively dominated by the natural flow turning of the fan rotor.

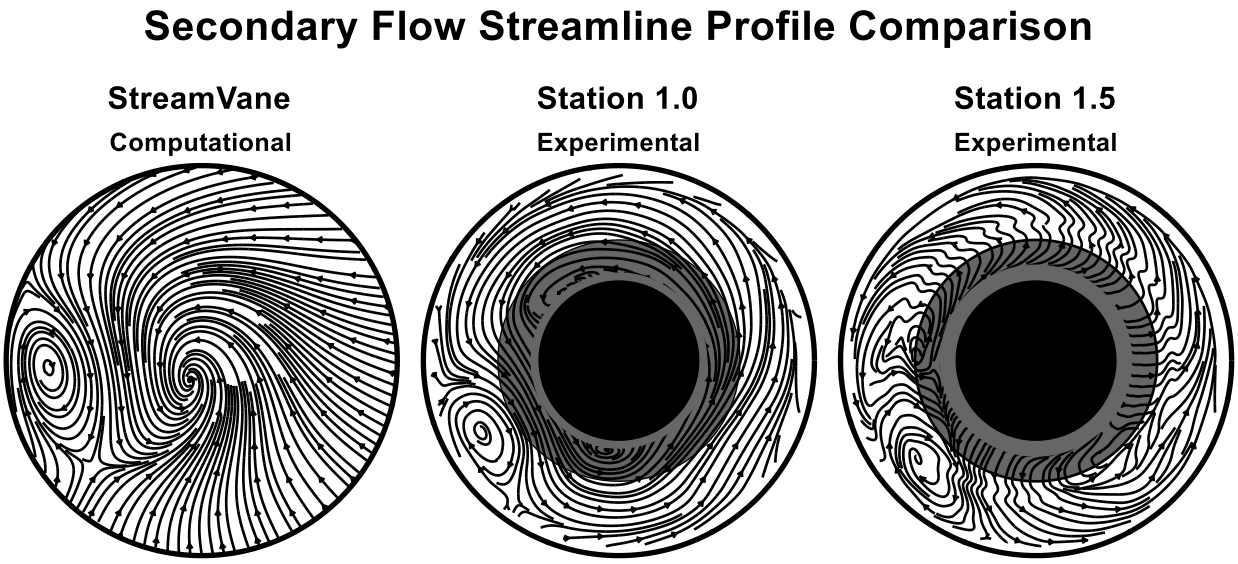

Figure 5.4: Comparison of Secondary Flow Streamline Profile Results

The streamlines provided the most striking representation of the fan rotor response to inlet swirl distortion. Between the StreamVane plane and Station 1.0, minimal changes in flow directionality or structure were evident. The exceptions to this were the circumferential convection of the tightly-wound vortex core and the necessity of the flow to avoid the solid body of the spinner cone. The spinner cone interactions reduced the amount of radially inward flow produced by the StreamVane. As the distortion passed through the fan rotor, much of the circumferential flow found upstream at Station 1.0 had been processed resulting in nearly clean conditions in the bulk swirl region. Again, the exception to this result was the tightly-wound vortex feature which appears to have passed almost unchanged through the fan rotor, with additional convection in the fanwise direction.

5.2 Conclusions and Recommendations

The results from this experimental investigation of fan response to inlet swirl distortion provided novel insights into the fluid dynamics of non-uniform flow entering a turbofan engine. Measurements immediately upstream and immediately downstream of the fan rotor isolated the component and allowed a thorough study of the ability of the fan rotor to process a tailored swirl distortion. Additionally, the total pressure measurements recorded at the fan inlet plane (downstream of the StreamVane) confirmed that the swirl distortion was decoupled from the complex, combined swirl/pressure distortions typically created by full-scale engine inlets. This was an important discovery in that the fan response to a single component of distortion was investigated.

The most significant outcome from this investigation was the confirmation of secondary flow in the measurement plane downstream of the fan rotor. This result indicated that the fan rotor was incapable of completely eliminating the swirl distortion leading to off-design conditions propagating into downstream components. The off-design conditions not only affect the performance and efficiency of the fan rotor, but also have cascading effects on the performance and efficiency of the entire propulsion system.

While the flow exiting the fan rotor was determined to contain artifacts of the upstream swirl distortion profile, significant reductions in flow angularity and secondary flow velocity magnitudes were achieved by the fan. This partial processing of the swirl distortion suggested that fan rotors can be designed to mitigate the effects of non-uniform inlet flow. The persistence of swirl through the fan rotor also leads to the possibility of utilizing multiple stages to straighten the flow. For example, swirl with high flow angles can be partially processed by the fan and fan exit guide vane system rather than only in the fan rotor components. Additionally, non-uniform engine architecture can be designed that focuses on more severe local distortions, such as the tightly wound vortex from this investigation. This recommendation reduces the amount of design changes to any single component and attempts to optimize the propulsor at the system level.

From this investigation, it was found that the type of swirl distortion interacting with the fan was important. Large scale, bulk swirl throughout the annulus of the fan rotor was nearly eliminated by the fan rotor; however, a smaller, tightly-wound vortex passed almost unaltered through the fan rotor. This result demonstrated that small-scale, intense vortex structures should be avoided when designing and optimizing next generation aircraft and propulsion inlet systems.

The entrance length between the swirl generation plane and the fan inlet also had an effect on the resulting measured flow field properties. Vortex convection and dissipation are two important mechanisms to analyze when designing turbofan inlets. Natural mixing of the flow reduced distortion magnitudes from the predicted CFD models. Furthermore, vortex-to-vortex and vortex-to-fan interactions were shown to move the well-defined tightly-wound vortex in the fanwise direction before reaching the fan inlet.

Overall, the investigation provided useful information for the design of next-generation, highly-integrated aircraft architectures. Through the use of a StreamVane, this investigation also proved that tailored swirl distortion profiles can be created in the inlet duct of a turbofan engine research platform without the requirement of full scale engine inlet test articles. While distorted inlet flows may be an unavoidable challenge facing aircraft/engine integration, the results presented in this document will assist in understanding and effects of swirl distortion, increase the practicality of boundary layer ingestion, and provide novel data for decision making and design of distortion tolerant aircraft engine components.

Bibliography

[1] Collier, F., Thomas, R., Burley, C., Nickol, C., Lee, C., and Tong, M., "Environmentally Responsible Aviation – Real Solutions for Environmental Challenges Facing Aviation," *27th International Congress of the Aeronautical Sciences*, No. ICAS 2010-1.6.1, ICAS, Nice, France, September 2010.

[2] Suder, K. L., "Overview of the NASA Environmentally Responsible Aviation Project's Propulsion Technology Portfolio," *48th AIAA/ASME/SAE/ASEE Joint Propulsion Conference & Exhibit*, No. AIAA 2012-4038, AIAA, Atlanta, Georgia, August 2012.

[3] Whalen, E. A., Lacy, D., Lin, J. C., Andino, M. Y., Washburn, A. E., Graff, E., and Wygnanski, I. J., "Performance Enhancement of a Full-Scale Vertical Tail Model Equipped with Active Flow Control," *53rd AIAA Aerospace Sciences Meeting*, No. AIAA 2015-0784, AIAA, Kissimmee, Florida, January 2015.

[4] Joslin, R. D., "Aircraft Laminar Flow Control," *Annual Review of Fluid Mechanics*, Vol. 30, 1-29, Annual Reviews, January, 1998

[5] Young, T. M., Tobin, E. F., and Kok, M., "Laboratory Testing of Insect Contamination for Laminar Flow Applications using an Insect-Impact Test Facility," *28th International Congress of the Aeronautical Sciences,* No. ICAS 2012-3.4.4, ICAS, Brisbane, Australia, September 2012.

[6] Wohl, C. J., Smith, J. G., Connell, J. W., and Siochi, E. J., "Engineered Surfaces for Mitigation of Insect Residue Adhesion," *51st AIAA Aerospace Sciences Meeting including the New Horizons Forum and Aerospace Exposition*, No. AIAA 2013-0413, AIAA, Grapevine, Texas, January 2013.

[7] Velicki, A., Thrash, P., and Jegley, D., "Airframe Development for the Hybrid Wing Body Aircraft," *47th AIAA Aerospace Sciences Meeting including the New Horizons Forum and Aerospace Exposition*, No. AIAA 2009-932, AIAA, Orlando, Florida, January 2009.

[8] Velicki, A. and Jegley, D., "PRSEUS Development for the Hybrid Wing Body Aircraft," *AIAA Centennial of Naval Aviation Forum "100 Years of Achievement and Progress,"* No. AIAA 2011-7025, AIAA, Virginia Beach, Virginia, September 2011.

[9] Jegley, D. and Velicki, A., "Status of Advanced Stitched Unitized Composite Aircraft Structures" *51st AIAA Aerospace Sciences Meeting including the New Horizons Forum and Aerospace Exposition*, No. AIAA 2013-0410, AIAA, Grapevine, Texas, January 2013.

[10] Velicki, A. and Jegley, D., "PRSEUS Structural Concept Development,"*52nd Aerospace Sciences Meeting*, No. AIAA 2014-0259, AIAA, National Harbor, Maryland, January 2014.

[11] Suder, K. L., Delaat, J., Hughes, C., Arend, D., and Celestina, M., "NASA Environmentally Responsible Aviation Project's Propulsion Technology Phase I Overview and Highlights of Accomplishments," *51st AIAA Aerospace Sciences Meeting including the New Horizons Forum and Aerospace Exposition*, No. AIAA 2013-0414, AIAA, Grapevine, Texas, January 2013.

[12] Halbig, M. C., Jaskowiak, M. H., Kiser, J. D., and Zhu, D., "Evaluation of Ceramic Matrix Composite Technology for Aircraft Turbine Engine Applications," *51st AIAA Aerospace Sciences Meeting including the New Horizons Forum and Aerospace Exposition*, No. AIAA 2013-0539, AIAA, Grapevine, Texas, January 2013.

[13] Daggett, D. L., Kawai, R., and Friedman, D., "Blended Wing Body Systems Studies: Boundary Layer Ingestion Inlets with Active Flow Control," *NASA Contractor Report*, No. NASA/CR-2003-212670, December 2003.

[14] Gern, F. H., "Conceptual Design and Structural Analysis of an Open Rotor Hybrid Wing Body Aircraft," *54th AIAA/ASME/ASCE/AHS/ASC Structures, Structural Dynamics, and Materials Conference*, No. AIAA 2013-1688, AIAA, Boston, Massachusetts, April 2013.

[15] Greitzer, E., Bonnefoy, P., De la Rosa Blanco, E., Dorbian, C., Drela, M., Hall, D., Hansman, R., Hileman, J., Liebeck, R., Lovegren, J., Mody, P., Pertuze, J., Sato, S., Spakovszky, Z., Tan, C., Hollman, J., Duda, J., Fitzgerald, N., Houghton, J., Kerrebrock, J., Kiwada, G., Kordonowy, D., Parrish, J., Tylko, J., Wen, E., and Lord, W., "N+3 Aircraft Concept Designs and Trade Studies, Final Report, Volume 1," *NASA Contractor Report*, No. NASA/CR-2010-216794/VOL1, December 2010.

[16] Ashcraft, S. W., Padron, A. S., Pascioni, K. A., Stout, G. W., and Huff, D. L., "Review of Propulsion Technologies for N+3 Subsonic Vehicle Concepts," *NASA Technical Memorandum*, No. NASA/TM-2011-217239, October 2011.

[17] Drela, M., "Development of the D8 Transport Configuration," *29th AIAA Applied Aerodynamics Conference*, No. AIAA 2011-3970, AIAA, Honolulu, Hawaii, June 2011.

[18] Pandya, S. A., "External Aerodynamics Simulations for the MIT D8 'Double-Bubble' Aircraft Design," 7th International Conference on Computational Fluid Dynamics, No. ICCFD7-4304, ICCFD7, Big Island, Hawaii, July 2012.

[19] Tong, M. T., Jones, S. M., Haller, W. J., and Handschuh, R. F., "Engine Conceptual Design Studies for a Hybrid Wing Body Aircraft," *NASA Technical Memorandum*, No. NASA/TM-2009-215680, November 2009.

[20] Gatlin, G. M., Vicroy, D. D., and Carter, M. B., "Experimental Investigation of the Low-Speed Aerodynamic Characteristics of a 5.8-Percent Scale Hybrid Wing Body Configuration," 30th AIAA Applied Aerodynamics Conference, No. AIAA 2012-2669, AIAA, New Orleans, Louisiana, June 2012.

[21] Thomas, R. H., Czech, M. J., and Doty, M. J., "High Bypass Ratio Jet Noise Reduction and Installation Effects Including Shielding Effectiveness," *51st AIAA Aerospace Sciences Meeting including the New Horizons Forum and Aerospace Exposition*, No. AIAA 2013-0541, AIAA, Grapevine, Texas, January 2013.

[22] Hamed, A. and Numbers, K., "Inlet Distortion Considerations for High Cycle Fatigue in Gas Turbine Engine," *33rd Joint Propulsion Conference and Exhibit*, No. AIAA 1997-3364, AIAA, Seattle, Washington, June 1997.

[23] Kawai, R. T., Friedman, D. M., and Serrano, L., "Blended Wing Body (BWB) Boundary Layer Ingestion (BLI) Inlet Configuration and System Studies," *NASA Contractor Report*, No. NASA/CR-2006-214534, December 2006, Boeing Phantom Works, Huntington Beach, California.

[24] Plas, A. P., Sargeant, M. A., Madani, V., Crichton, D., Greitzer, E. M., Hynes, T. P., and Hall, C. A., "Performance of Boundary Layer Ingesting (BLI) Propulsion System," *45th AIAA Aerospace Sciences Meeting and Exhibit*, No. AIAA 2007-450, AIAA, Reno, Nevada, January 2007.

[25] Hardin, L. W., Tillman, G., Sharma, O. P., Berton, J., and Arend, D. J., "Aircraft System Study of Boundary Layer Ingesting Propulsion," *48th AIAA/ASME/SAE/ASEE Joint Propulsion Conference & Exhibit*, No. AIAA 2012-3993, AIAA, Atlanta, Georgia, August 2012.

[26] Ferrar, A. M., and O'Brien, W. F., "Progress in Boundary Layer Ingesting Embedded Engine Research," *48th AIAA/ASME/SAE/ASEE Joint Propulsion Conference & Exhibit*, No. AIAA 2012-4283, AIAA, Atlanta, Georgia, August 2012.

[27] Qin, N., Vavalle, A., Le Moigne, A., Laban, M., Hackett, K., and Weinerfelt, P., "Aerodynamic Studies for Blended Wing Body Aircraft," *9th AIAA/ISSMO Symposium on Multidisciplinary Analysis and Optimization*, AIAA-2002-5448, AIAA, Atlanta, Georgia, September 2002.

[28] Daggett, D. L., "Ultra Efficient Engine Technology Systems Integration and Environmental Assessment," *NASA Contractor Report*, No. NASA/CR-2002-211754, July 2002, Boeing Commercial Airplane Group, Seattle, Washington.

[29] Cousins, W. T., "History, Philosophy, Physics, and Future Directions of Aircraft Propulsion System/Inlet Integration," *Proceedings of ASME Turbo Expo 2004: Power for Land, Sea, and Air*, No. GT2004-54210, ASME, Vienna, Austria, June 2004.

[30] Kurzke, J., "Effects of Inlet Flow Distortion on the Performance of Aircraft Gas Turbines," *Proceedings of ASME Turbo Expo 2006: Power for Land, Sea, and Air*, No. GT2006-90419, ASME, Barcelona, Spain, May 2006.

[31] Lucas, J. R., O'Brien, W. F., and Ferrar, A. M., "Effect of BLI-Type Inlet Distortion on Turbofan Engine Performance," *Proceedings of ASME Turbo Expo 2014: Turbine Technical Conference and Exposition*, No. GT2014-26666, ASME, Dusseldorf, Germany, June 2014.

[32] Ferrar, A. M., "Measurement and Uncertainty Analysis of Transonic Fan Response to Total Pressure Inlet Distortion," Ph.D. Dissertation, Mechanical Engineering Department, Virginia Polytechnic Institute and State University, 2015.

[33] Gunn, E. J., Tooze, S. E., Hall, C. A., and Colin, Y., "An Experimental Study of Loss Sources in a Fan Operating with Continuous Inlet Stagnation Pressure Distortion," *Journal of Turbomachinery*, ASME, Vol. 135, September 2013.

[34] Gunn, E. J. and Hall, C. A., "Aerodynamics of Boundary Layer Ingesting Fans," *Proceedings of ASME Turbo Expo 2014: Turbine Technical Conference and Exposition*, No. GT2014-26142, ASME, Düsseldorf, Germany, June 2014.

[35] Bakhle, M. A., Reddy, T. S. R., Herrick, G. P., Shabbir, A., and Florea, R. V., "Aeromechanics Analysis of a Boundary Layer Ingesting Fan," *NASA Technical Memorandum*, No. NASA/TM-2013-217730, January 2013.

[36] Choi, M., Vahdati, M., and Imregun, M., "Effects of Fan Speed on Rotating Stall Inception and Recovery," *Journal of Turbomachinery*, ASME, Vol. 133, October 2011.

[37] Owens, L. R., Allen, B. G., and Gorton, S. A., "Boundary-Layer-Ingesting Inlet Flow Control," *44th AIAA Aerospace Sciences Meeting and Exhibit*, No. AIAA 2006-839, AIAA, Reno, Nevada, January 2006.

[38] Davis, M. and Hale, A., "A Parametric Study on the Effects of Inlet Swirl on Compression System Performance and Operability using Numerical Simulations," *Proceedings of ASME Turbo Expo 2007: Power for Land, Sea, and Air*, No. GT2007-27033, ASME, Montreal, Canada, May 2007.

[39] Pardo, A. C., Mehdi, A., Pachidis, V., and MacManus D. G., "Numerical Study of the Effect of Multiple Tightly-Wound Vortices on a Transonic Fan Stage Performance," *Proceedings of ASME Turbo Expo 2014: Turbine Technical Conference and Exposition*, No. GT2014-26481, ASME, Düsseldorf, Germany, June 2014.

[40] "A Methodology for Assessing Inlet Swirl Distortion," Aerospace Information Report, SAE AIR5686, SAE Aerospace, November 2010.

Bibliography

[41] Davis, M., Hale, A., and Beale, D., "An Argument for Enhancement of the Current Inlet Distortion Ground Test Practice for Aircraft Gas Turbine Engines," *Journal of Turbomachinery*, ASME, Vol. 124, April 2002.

[42] Sheoran, Y., Bouldin, B., and Krishnan, P. M., "Compressor Performance and Operability in Swirl Distortion," *Journal of Turbomachinery*, ASME, Vol. 134, July 2012.

[43] Hoopes, K. M. and O'Brien, W. F., "The StreamVane© Method: A New Way to Generate Swirl Distortion for Jet Engine Research," *49th AIAA/ASME/SAE/ASEE Joint Propulsion Conference*, No. AIAA 2013-3665, AIAA, San Jose, California, July 2013.

[44] Nelson, M. A., Lowe, K. T., O'Brien, W. F., Kirk, C., and Hoopes, K. M., "Stereoscopic PIV Measurements of Swirl Distortion on a Full-Scale Turbofan Engine Inlet," *52nd Aerospace Sciences Meeting*, No. AIAA 2014-0533, AIAA, National Harbor, Maryland, January 2014.

[45] Guimarães, T., Lowe, K. T., Nelson, M., O'Brien, W. F., and Kirk, C., "Stereoscopic PIV Measurements in a Turbofan Engine Inlet with Tailored Swirl Distortion," *AIAA Aviation 2015*, No. AIAA 2015-2866, AIAA, Dallas, Texas, June 2015.

[46] "Measurement of Gas Flow by Bellmouth Inlet Flowmeters," An American National Standard, ASME MFC-26-2011, ASME, August 2011.

[47] Treaster, A. L., and Yocum, A. M., "The Calibration and Application of Five-Hole Probes," *24th International Symposium*, No. TM 78-10, Albuquerque, New Mexico, January 1978.

[48] Hill, P. G. and Peterson, C. R., "Mechanics and Thermodynamics of Propulsion," Addison-Wesley Publishing Company, Second Edition, Boston, Massachusetts 1992.

Appendix A – Five-Hole Three-Dimensional Flow Probe Calibration

The five-hole three-dimensional flow probe was calibrated using an open jet wind tunnel in the Virginia Tech Aerospace and Ocean Engineering wind tunnel facilities. The probe was mounted in a custom two-axis rotary table (Figure A.1) that allowed for probe rotation in both the yaw (tangential) and pitch (radial) directions.

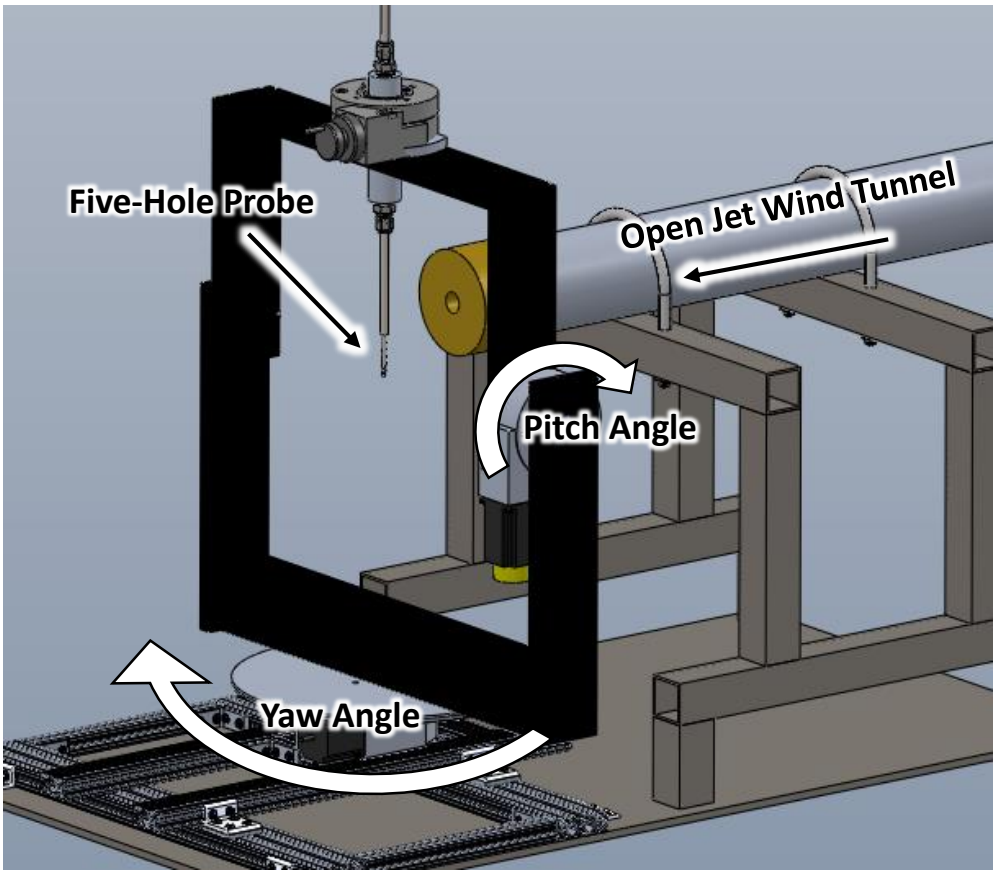

Figure A.1: Two-Axis Rotary Table for Five-Hole Probe Calibration

The probe was aligned radially (vertically) with the exit of the open jet wind tunnel using a laser device mounted on a stand-alone tripod downstream of the tunnel outlet. A crosshair target was placed at the exit of the wind tunnel and used to align the laser with the flow direction. Once the

light emitted by the laser device was aimed at the crosshair target, the target was removed. The probe was then installed in the mount via compression fittings attached to a tertiary rotary table on the upper cross member. The probe was positioned such that the P1 pressure port was aligned with the laser device, indicating that the probe sensing region was positioned at the centerline of the wind tunnel.

Using the manual rotary table, the probe was rotated 180° to face the outlet of the wind tunnel. A Dwyer 477A-1 handheld digital manometer was then connected to the P2-P3 pressure ports on the five-hole probe and compressed air was supplied to the upstream end of the open jet wind tunnel. Exploiting the nulling nature of the prism style five-hole probe, the rotary table was rotated while monitoring the manometer until the measured differential pressure was stable near zero. The angle on the rotary table was noted, and the process was repeated several times until the standard error of the average measured angle was within a tolerance threshold of ±0.020°.

With the probe now aligned in both the radial and tangential flow directions, the five outlet pressures as well as a wind tunnel plenum reference total pressure were connected to the ZOC17 pressure transducer. Air was then supplied to the open jet wind tunnel and the tunnel plenum reference pressure was allowed to stabilize. The probe was sequentially moved to a radial/tangential angle pair and pressure data was collected. The process of moving the probe to an angular pair and recording pressures was repeated until the entire calibration map was measured.

The processed pressure data was then reduced into pressure coefficients (Equations A.1 – A.5) [47]. The normalized pressure coefficients related measured pressures with flow anlgy pairs, effectively building two-dimensional calibration maps (Figure A.2 – Figure A.5). These calibration maps were then interpolated for use with the experimental data reduction processes described in Chapter 3.

$$Cp_{\alpha} = \frac{P_4 - P_5}{P_1 - \bar{P}} \tag{A.1}$$

$$Cp_{\beta} = \frac{P_2 - P_3}{P_1 - \bar{P}} \tag{A.2}$$

$$Cp_{P0} = \frac{P_1 - P_0}{P_1 - \bar{P}} \tag{A.3}$$

$$Cp_{P} = \frac{\bar{P} - P}{P_1 - \bar{P}} \tag{A.4}$$

$$\bar{P} = \frac{P_2 + P_3 + P_4 + P_5}{4} \tag{A.5}$$

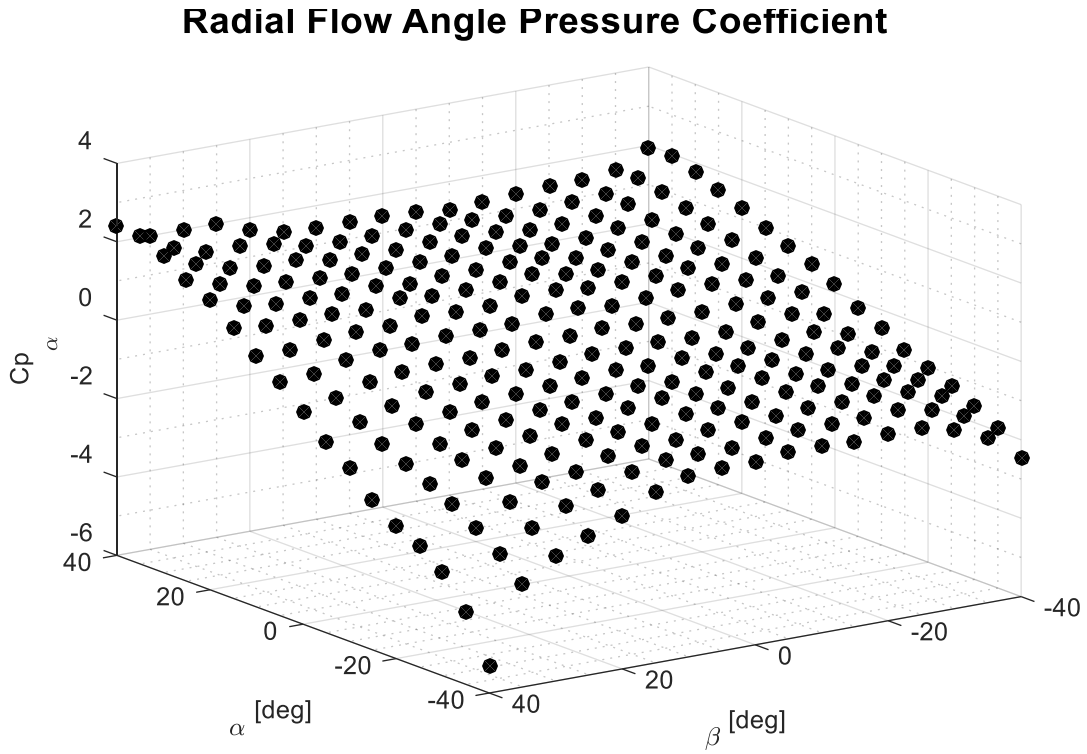

Figure A.2: Radial Flow Angle Calibration Map

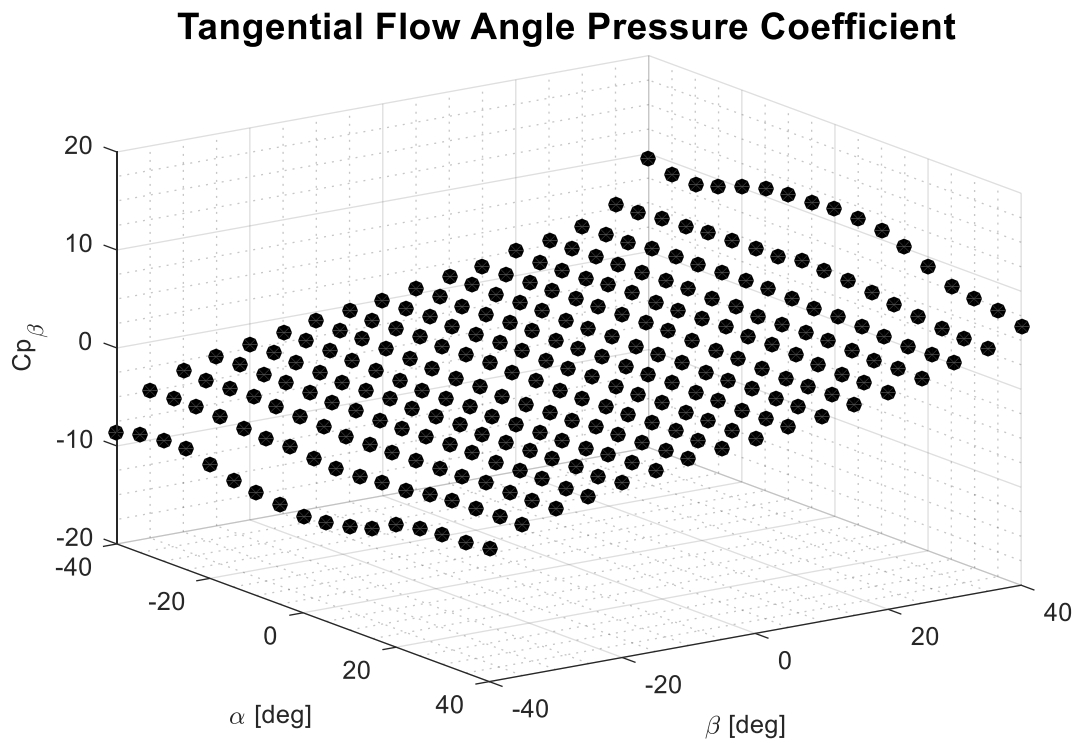

Figure A.3: Tangential Flow Angle Calibration Map

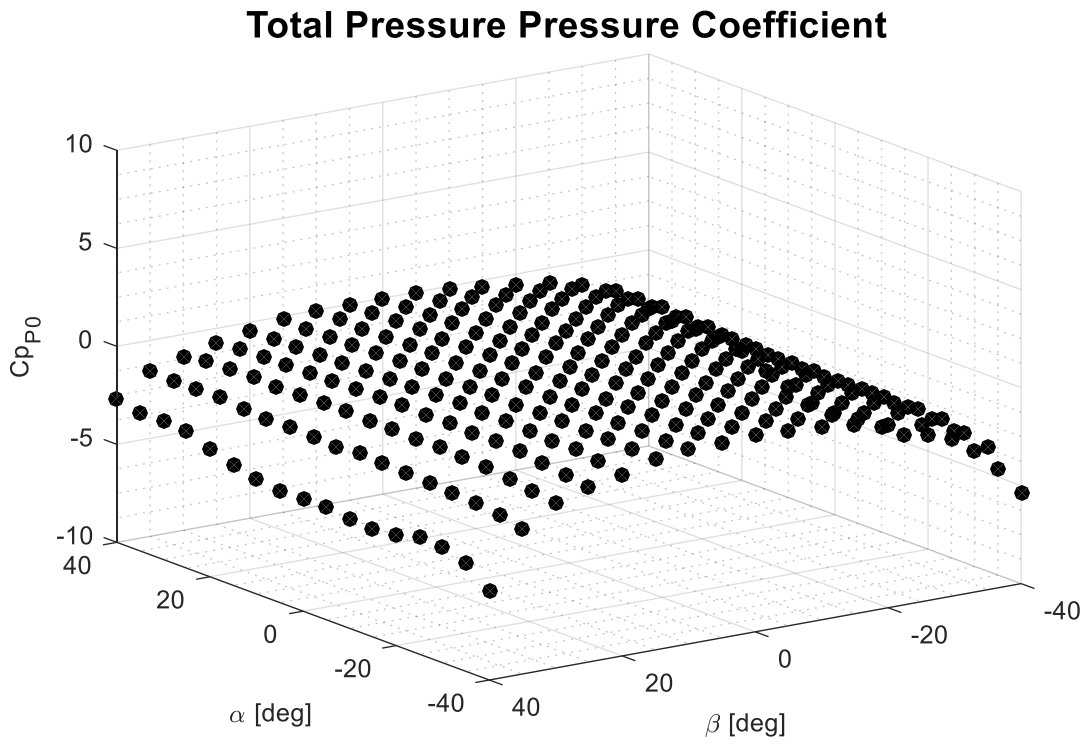

Figure A.4: Flow Total Pressure Calibration Map

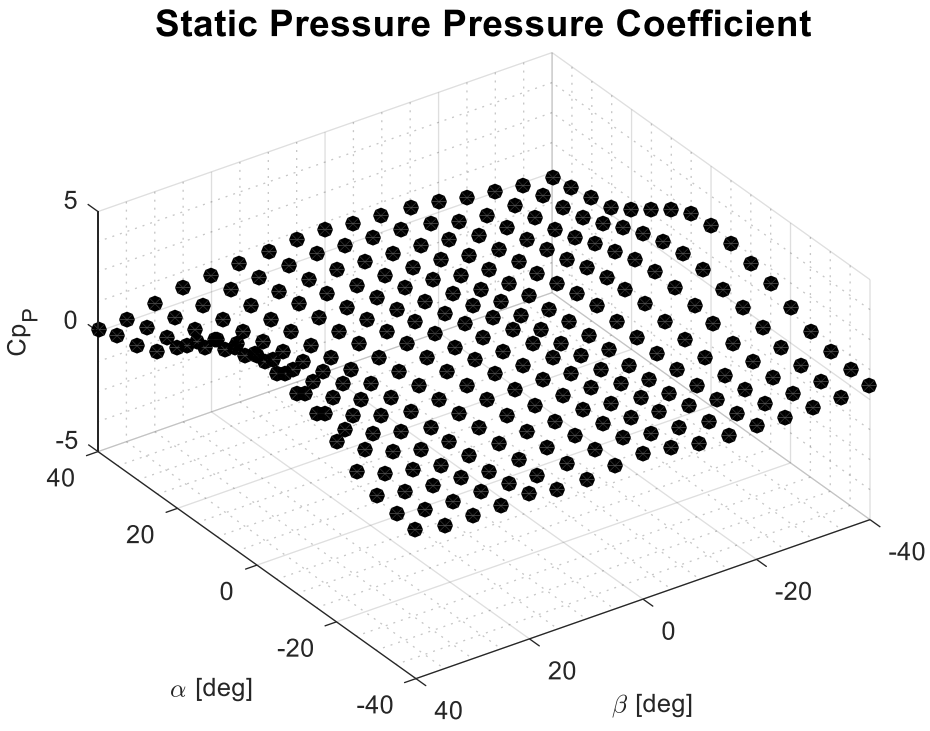

Figure A.5: Flow Static Pressure Calibration Map

Appendix B – Detailed Experimental Setup

The experimental setup began with the P&WC JT15D-1 turbofan research engine housed at the Virginia Tech Turbomachinery and Propulsion Research Laboratory (Figure B.1). The engine was mounted in a custom pylon that allowed researchers ample space to outfit the fan case with instrumentation. The fan case on the research platform had two threaded penetrations at top-dead-center. One penetration was positioned immediately upstream of the fan rotor and one penetration was positioned immediately downstream of the fan rotor. Compression fittings were threaded into the fan case penetrations (Figure B.2) to ensure an air tight seal around the five-hole three-dimensional flow probe.

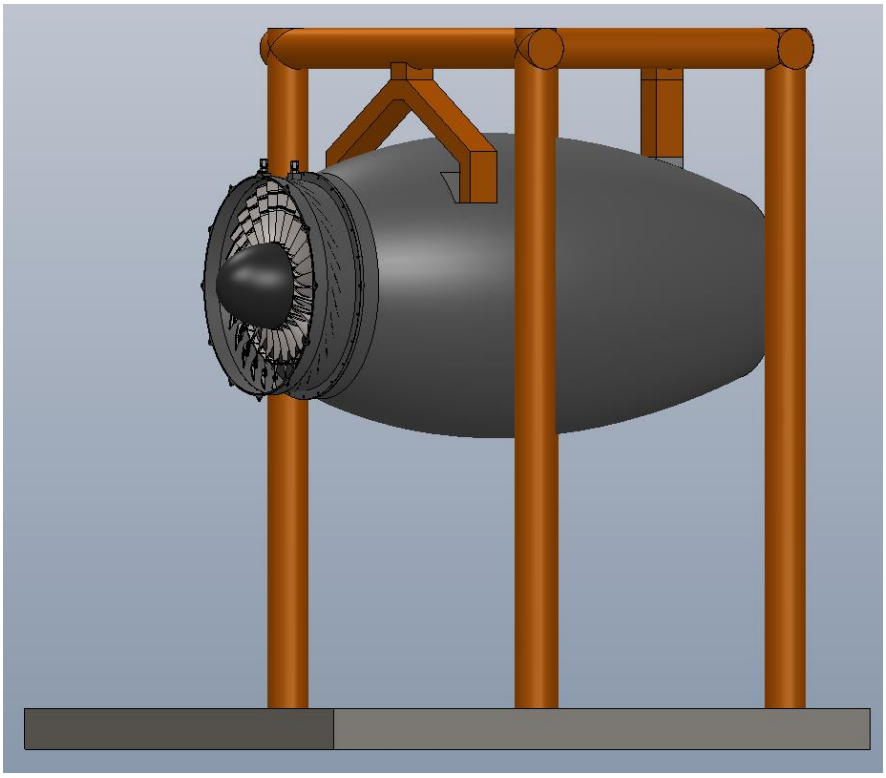

Figure B.1: P&WC JT15D-1 Turbofan Engine Research Platform

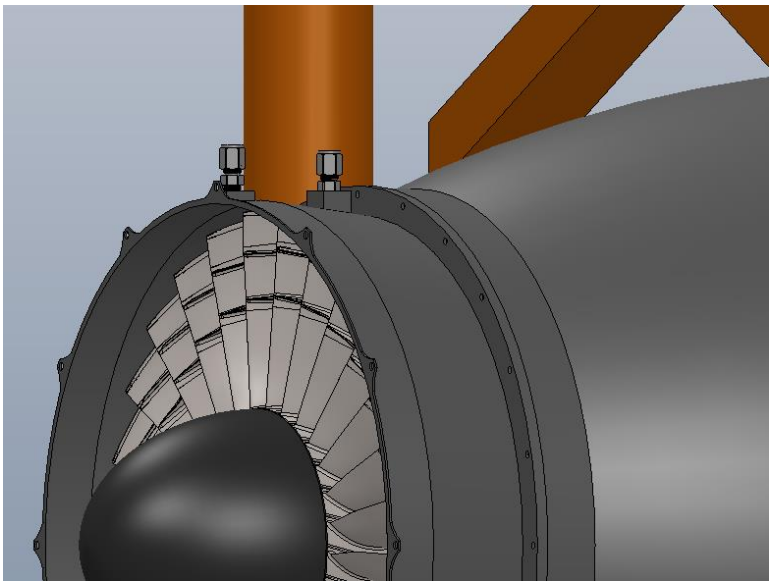

Figure B.2: Fan Case Probe Penetrations with Compression Fittings Installed

The five-hole three-dimensional flow probe radial traversing mount was fastened to the fan case using existing hardpoints. The probe axis was aligned with the selected fan case penetration through the use of a certified straight alloy steel shaft. Once aligned, the shaft was removed and replaced by the five-hole probe (Figure B.3).

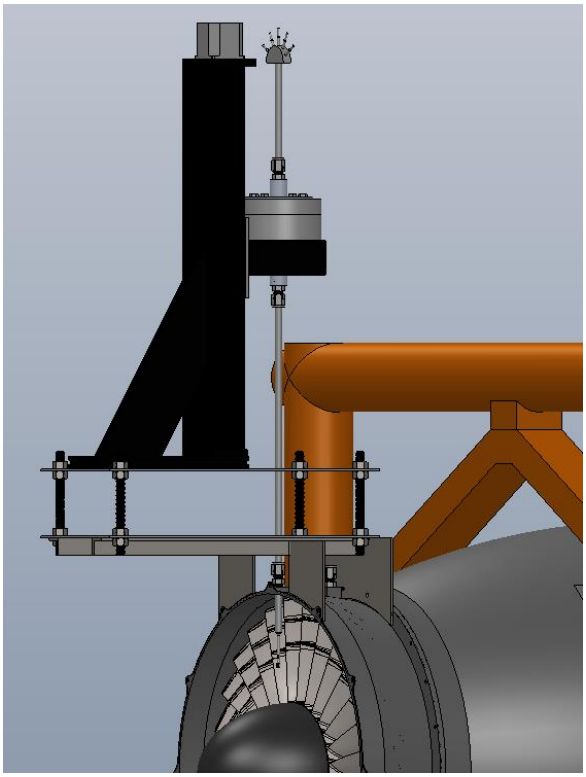

Figure B.3: Probe Radial Traversing Mount Installed Upstream of Fan Rotor

Due to the nulling nature of this probe, the differential pressure across the P2-P3 pressure ports read zero when the probe was properly aligned with the flow. A handheld digital manometer (Dwyer 477A-1) was connected to the P2-P3 pressure ports on the five-hole probe to measure the differential pressure. This manometer measured the differential pressure within fractions of an inch of water and provided sufficient accuracy to align the probe in the yaw direction.

The five-hole probe was then aligned to the engine axis using a custom open jet compressed air nozzle (Figure B.4). The nozzle apparatus consisted of a compressed air source, a flow straightening pipe, a machined frame bolted to the fan case, and a small downstream pipe to locate the jet exit as close as possible to the five-hole probe. The machined frame was assumed to position the nozzle parallel to the engine axis. The nozzle was positioned in front of the probe and the probe was aligned vertically such that the jet of air exiting the nozzle impinged on the sensing region. The nozzle apparatus was then connected to a compressed air source and regulated to a desired pressure.

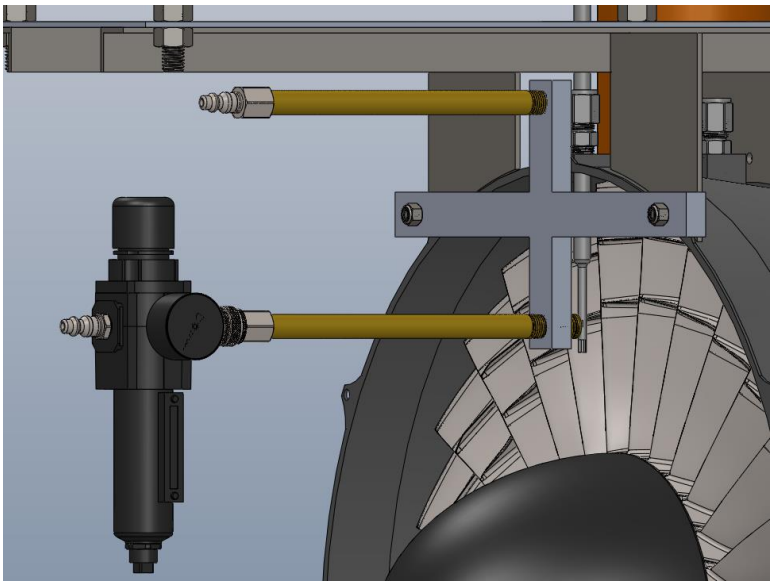

Figure B.4: Five-Hole Three-Dimensional Flow Probe Alignment Nozzle

Using the rotary table attached to the radial traversing mount, the probe was rotated until the measured differential pressure across the P2-P3 pressure ports stabilized near zero. The angle was recorded from the rotary table and the process was repeated approximately ten times until the standard error of the average angle was within ±0.020°. This value was selected based on a sensitivity analysis of the probe during calibration procedures.

Once the probe was sufficiently aligned with the flow, the open jet nozzle was removed and the probe was retracted to the inner wall of the fan case. A feeler gauge was utilized to ensure that the probe tip was flush with the in inner wall. This position served as home for all radial plunge movements during testing.

[Note: This procedure was nearly identical for the downstream probe location with the significant difference being that the probe was aligned outside the fan case. First, the upstream compression fitting was removed from the fan case due to interference constraints. The nozzle was then

attached to the fan case as pictured in Figure B.4 with a slightly longer outlet pipe to reach the downstream probe location. The probe was then aligned identically to the upstream case, plunged through the case wall, and positioned such that the tip was flush with the fan case.]

Next, a thin walled, cylindrical tunnel section was fastened to the fan case (Figure B.5). This tunnel section connected the StreamVane rotator to the fan case and allowed the swirl distortion to develop before entering the fan rotor.

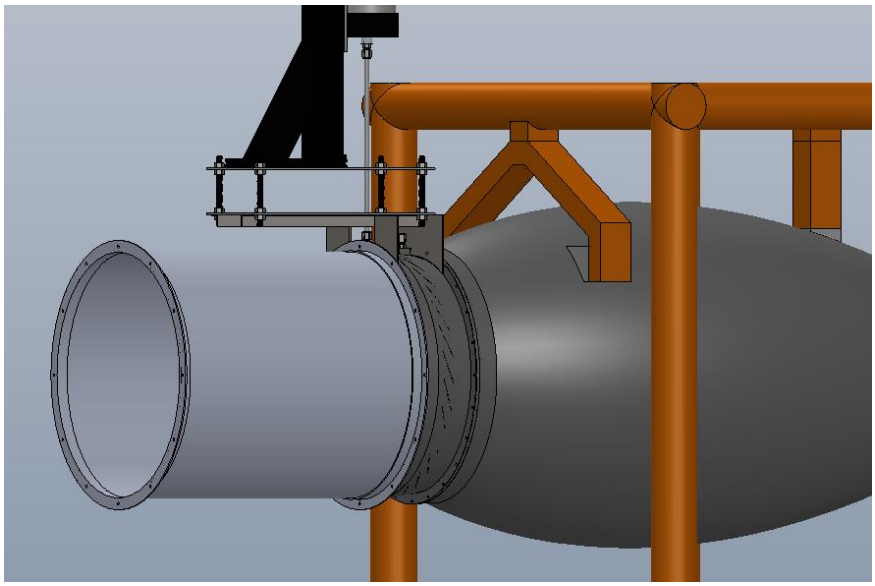

Figure B.5: Swirl Development Tunnel Section Fastened to the Fan Case

The StreamVane rotator was connected to the thin walled tunnel section (Figure B.6). This apparatus rotated the StreamVane swirl distortion device such that a single circumferential probe penetration could be utilized to collect data for the entire engine annulus.

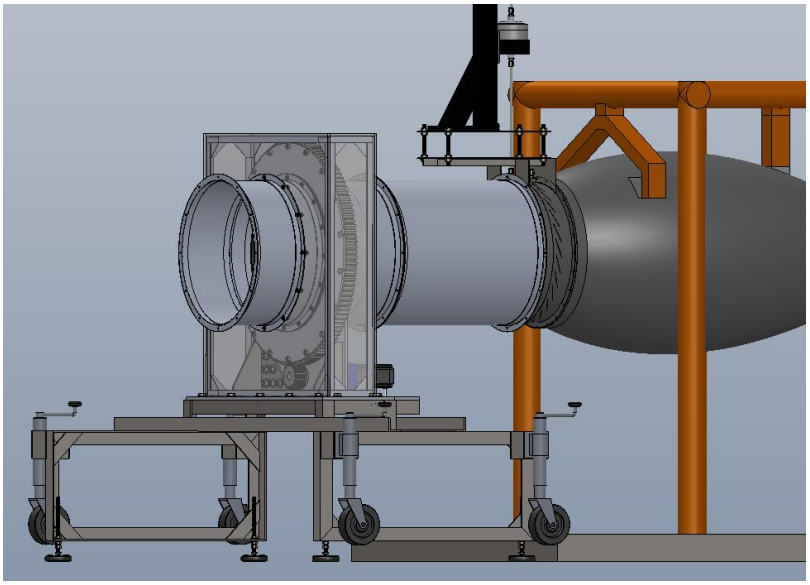

Figure B.6: StreamVane Rotator Installed on the Turbofan Engine Research Platform

The StreamVane was housed in a rotating slew bearing that consisted of a stationary frame, bearing system, external gear, drive pinion, drive gearbox transmission, and a drive motor (Figure B.7). The StreamVane was positioned using markings within the rotator tunnel section that were positioned during fabrication. The entire apparatus was contained within an air tight polycarbonate plastic pressure chamber. Rotator movements were monitored by a closed circuit camera viewing the pinion/slew gear contact point. Additionally, backlash in the gear system was eliminated by always rotating the StreamVane in one direction.

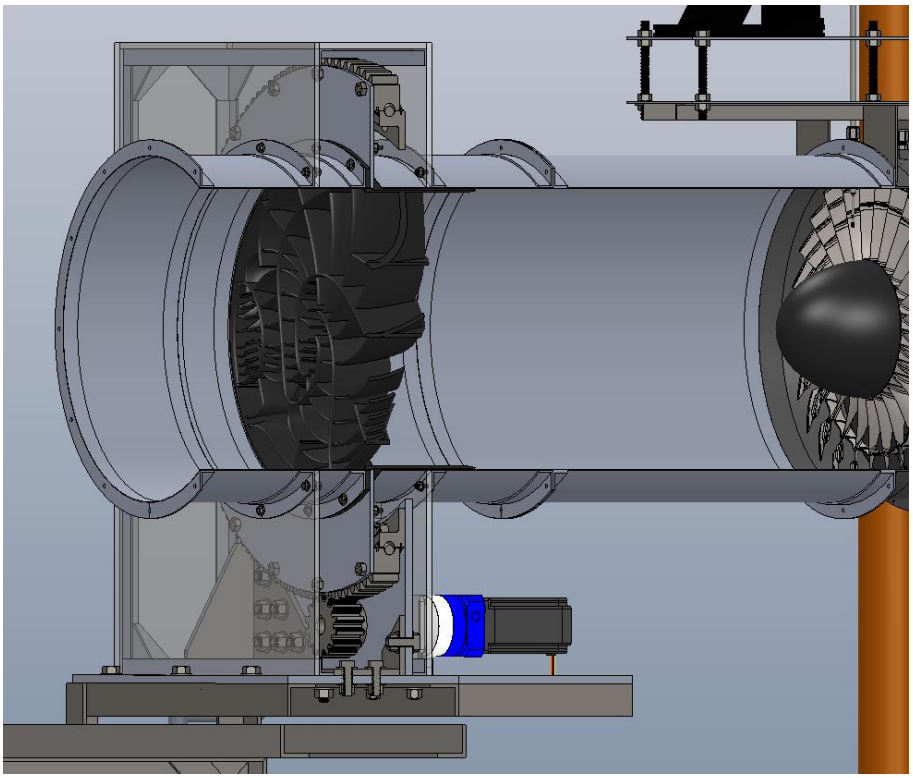

Figure B.7: Detailed View of StreamVane Rotator

[Note: For clean test conditions, the StreamVane and StreamVane rotator were removed from the engine inlet duct and replaced by a thin walled tunnel section that was an identical length as the StreamVane rotator.]

The bellmouth inlet and associated tunnel sections were installed upstream of the StreamVane rotator and secured. These components conditioned the flow in the inlet of the tunnel before the flow interacted with the StreamVane swirl distortion device.

Finally, the probes (wall static pressure taps, five-hole flow probe, thermocouple, optical once-per-rev) were connected to the instrumentation and data acquisition devices via tubing and wiring. The completed setup (Figure B.8) was now ready for test.

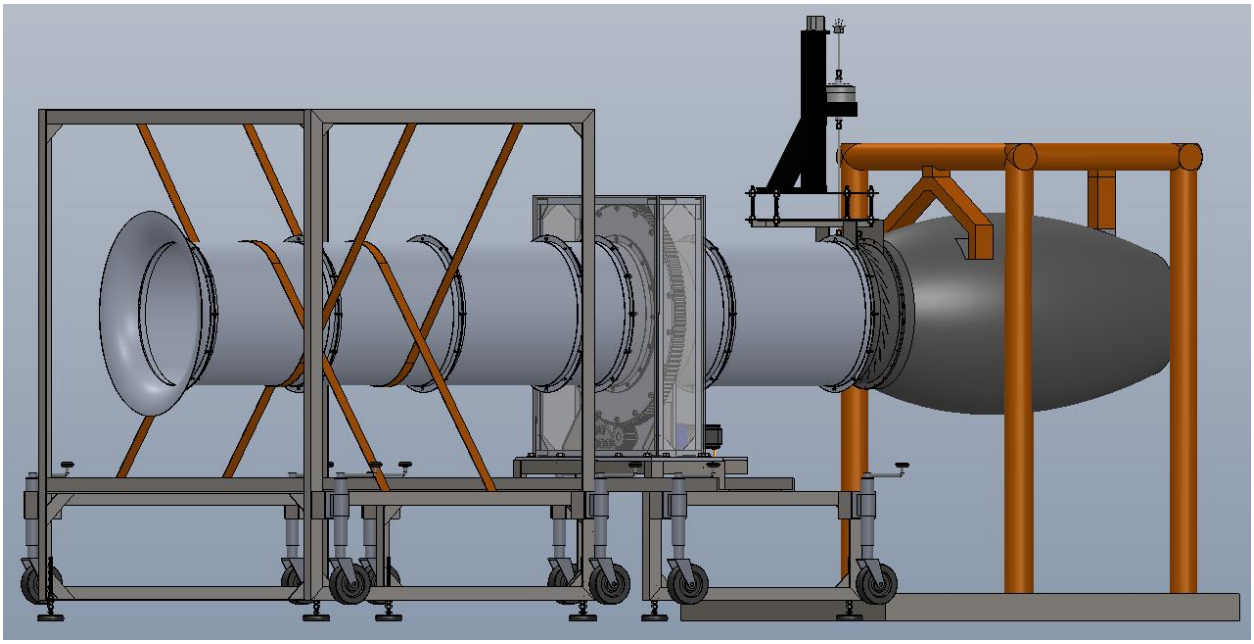

Figure B.8: Completed Test Setup Installed on the Turbofan Engine Research Platform

Appendix C – Station 1.0 Expanded Experimental Results

The following section contains the intermediate results that were utilized in the calculation of secondary flow velocity at the fan rotor inlet measurement plane (Station 1.0). Due to the large amount of information already contained in the discussion of results in Chapter 4, priority was placed on presenting only the most significant outcomes. While the following results were determined to be insignificant for the purposes of understanding and measuring the effects of swirl on the fan rotor and the corresponding response of the component to an inlet swirl distortion, it was important to provide this information for reference and completeness of experimental documentation.

The plotted values are presented without detailed discussion; however, all normalization equations are included where appropriate.

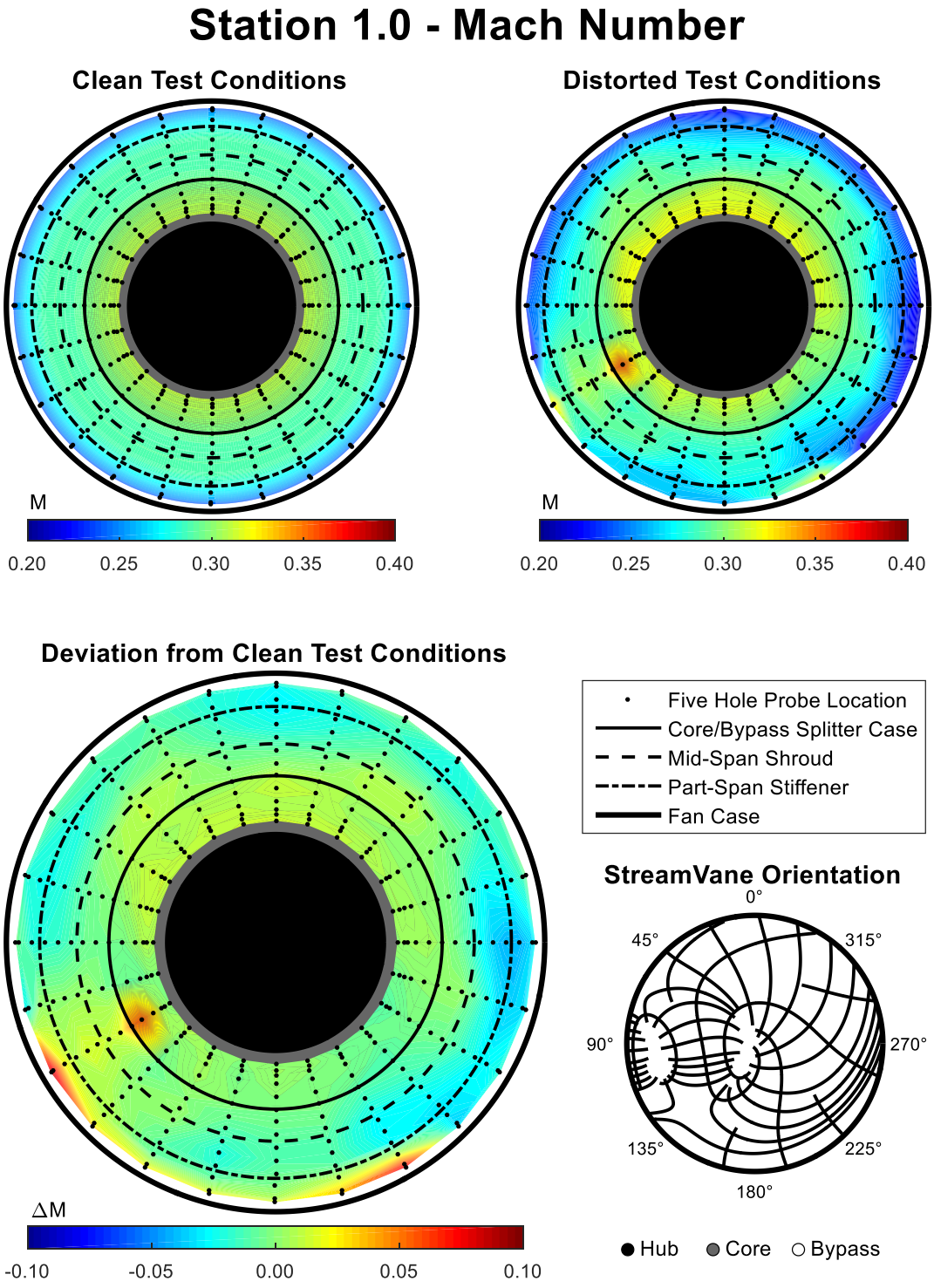

Figure C.1: Station 1.0 Mach Number Results

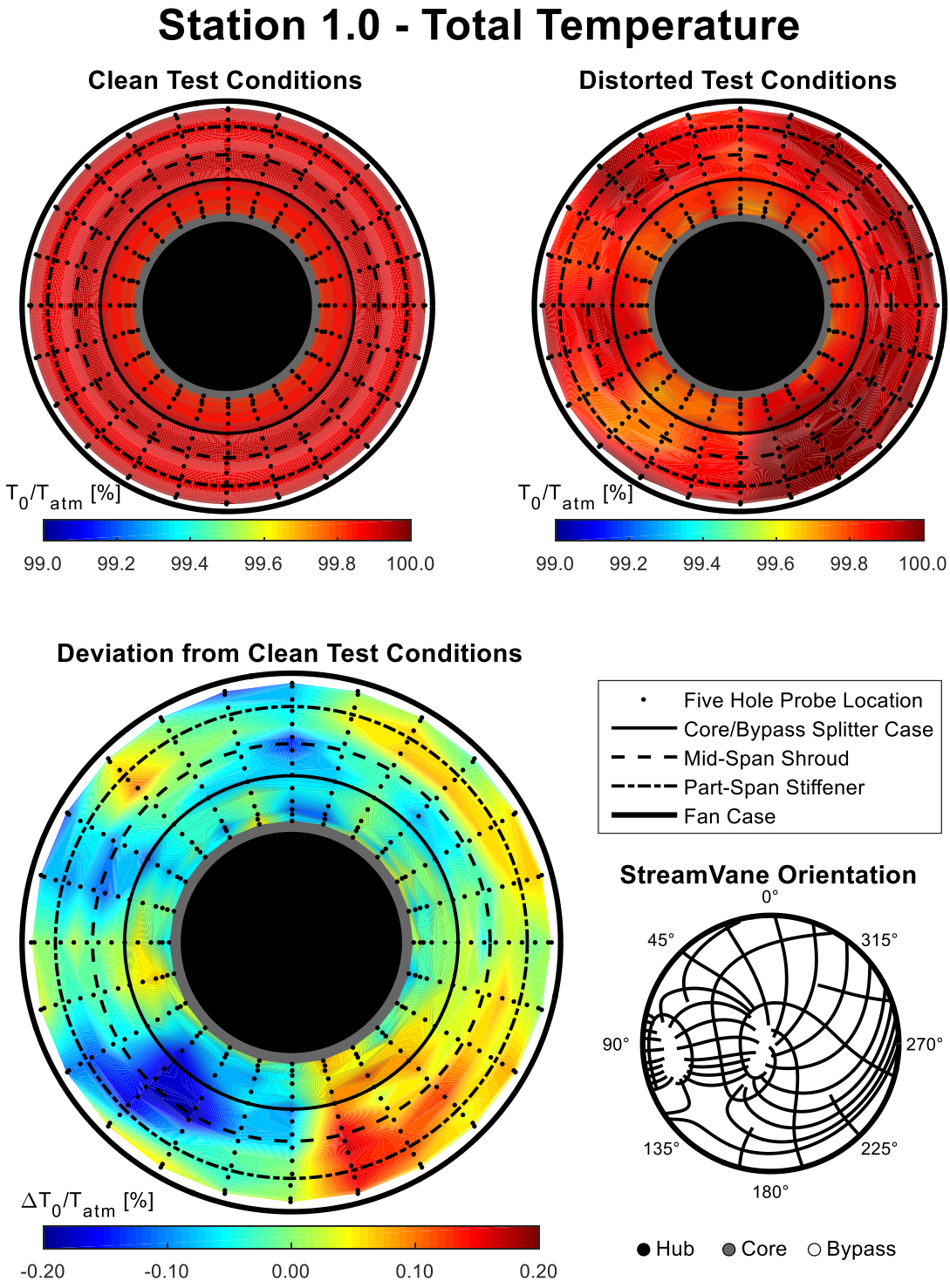

Figure C.2: Station 1.0 Total Temperature Results

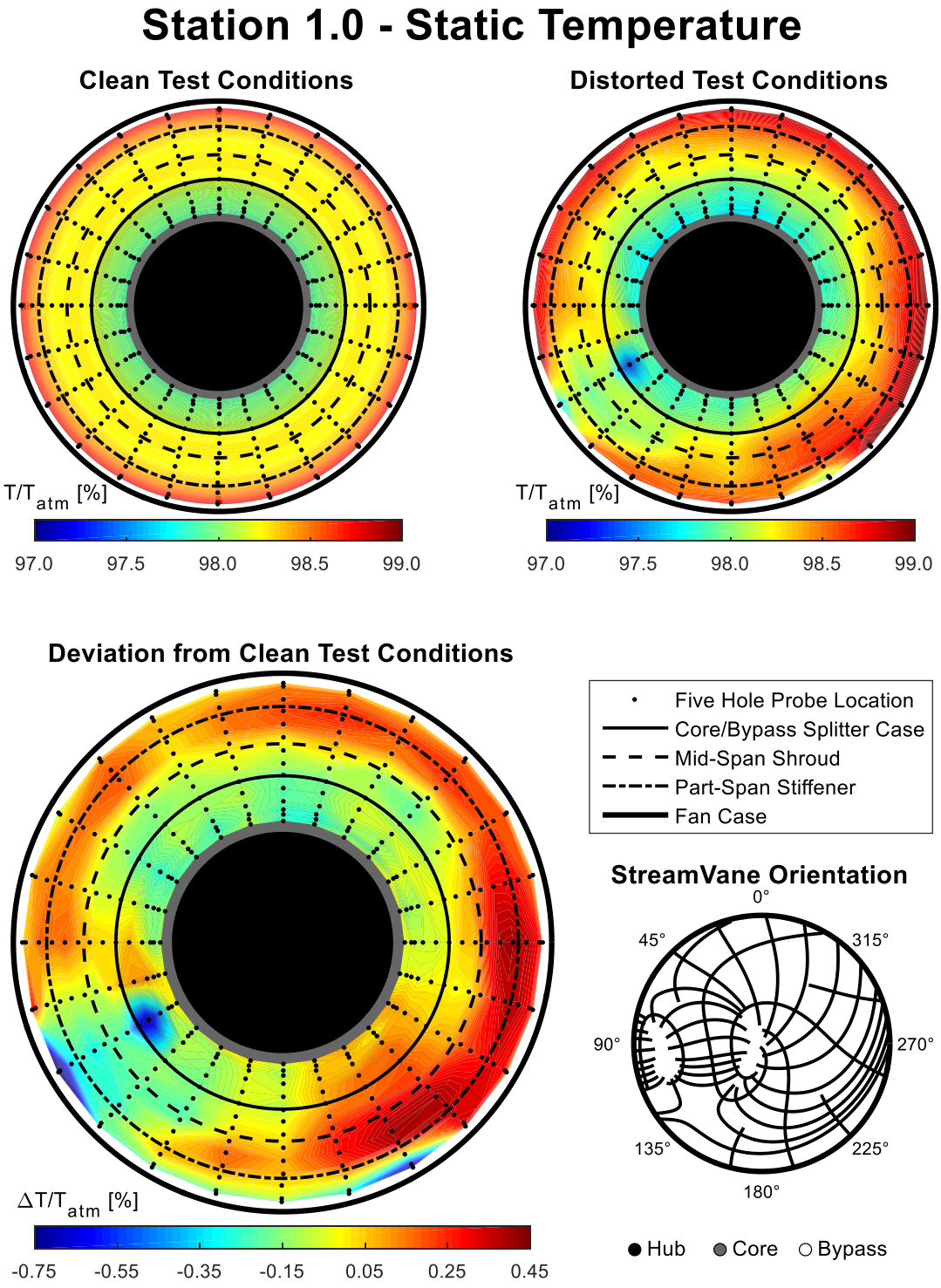

Figure C.3: Station 1.0 Static Temperature Number Results

Appendix D – Station 1.5 Expanded Experimental Results

The following section contains the intermediate results that were utilized in the calculation of secondary flow velocity at the fan rotor outlet measurement plane (Station 1.5). Due to the large amount of information already contained in the discussion of results in Chapter 4, priority was placed on presenting only the most significant outcomes. While the following results were determined to be insignificant for the purposes of understanding and measuring the effects of swirl on the fan rotor and the corresponding response of the component to an inlet swirl distortion, it was important to provide this information for reference and completeness of experimental documentation.

The plotted values are presented without detailed discussion; however, all normalization equations are included where appropriate.

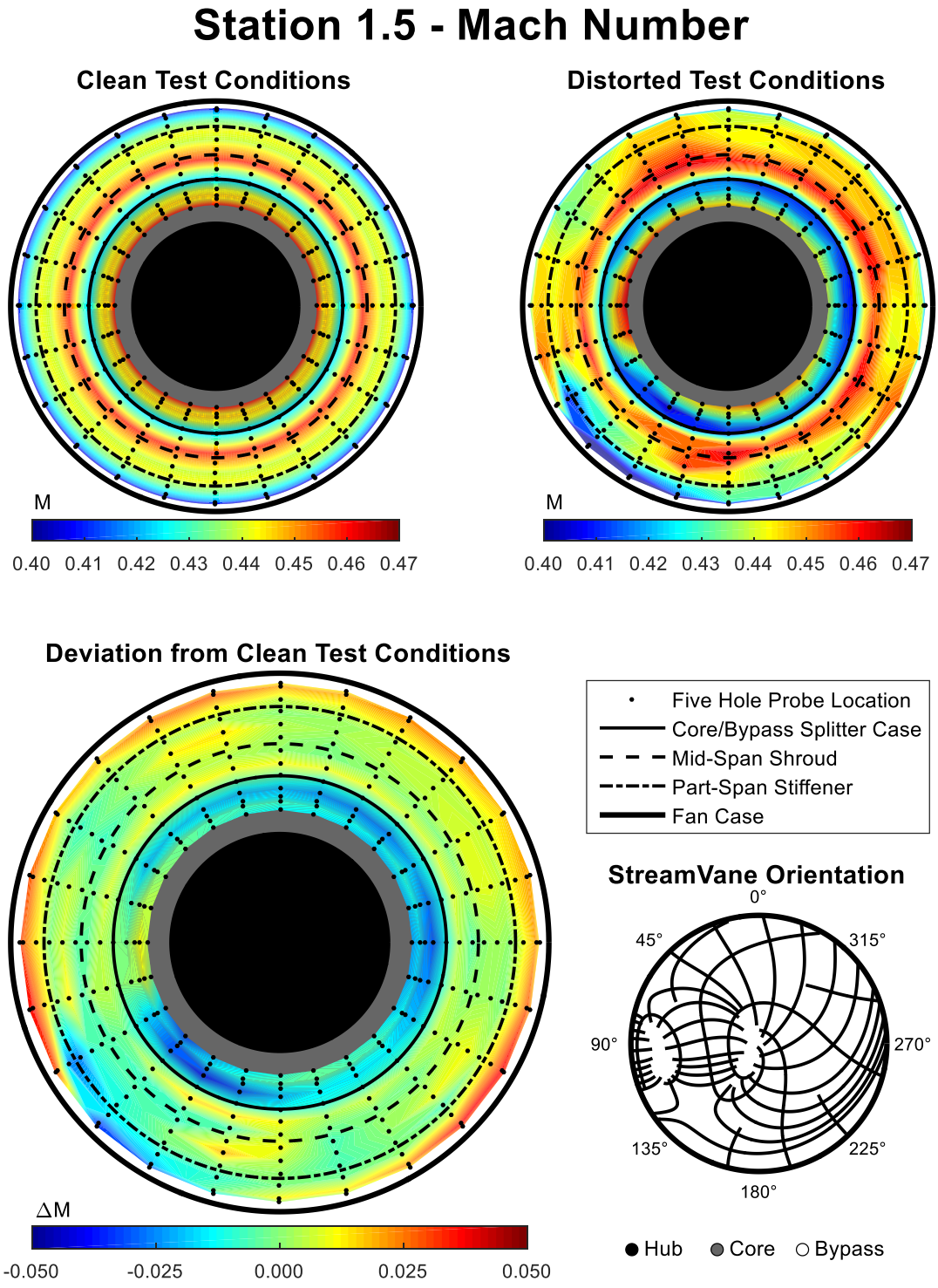

Figure D.1: Station 1.5 Mach Number Results

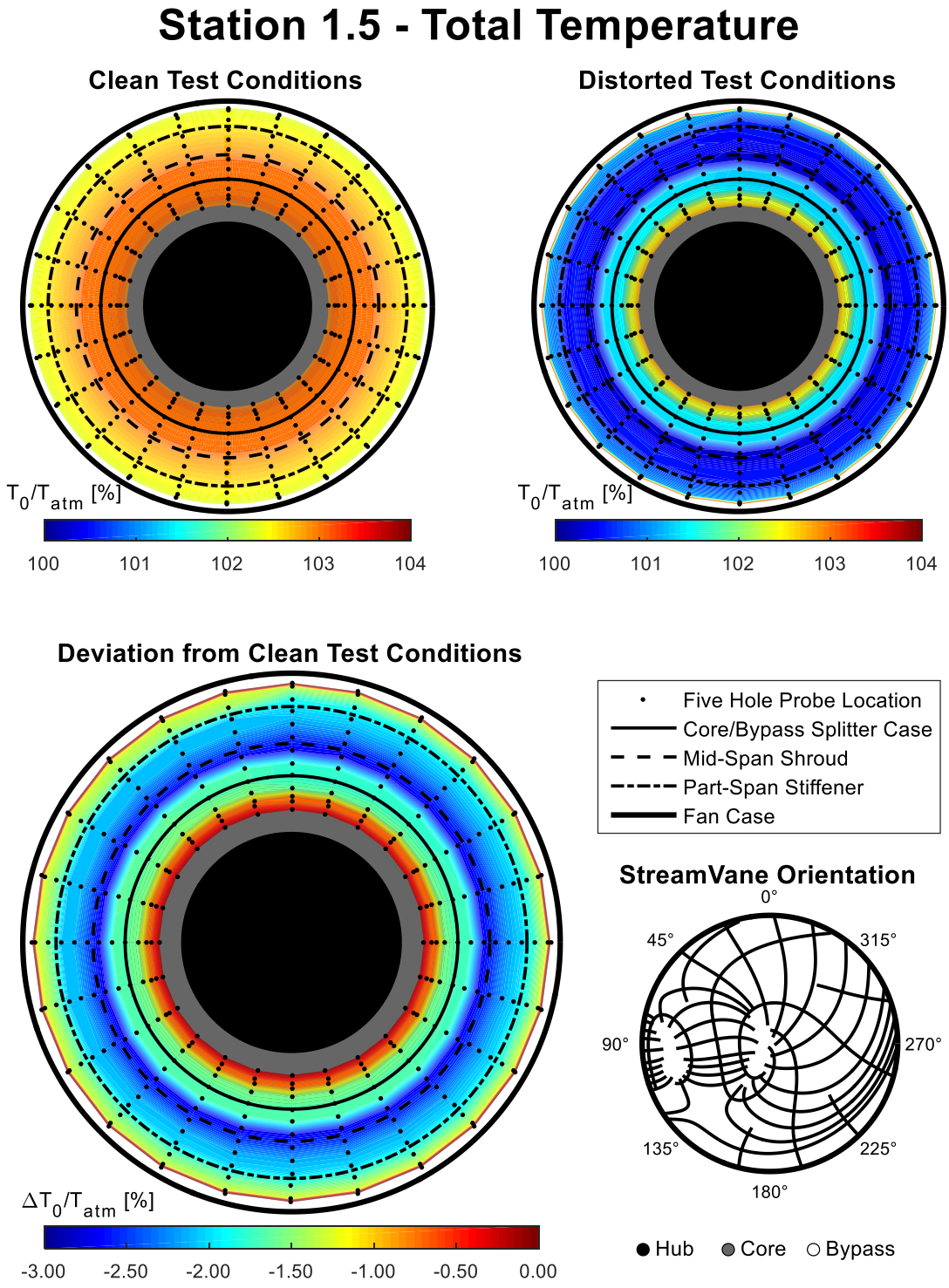

Figure D.2: Station 1.5 Total Temperature Results

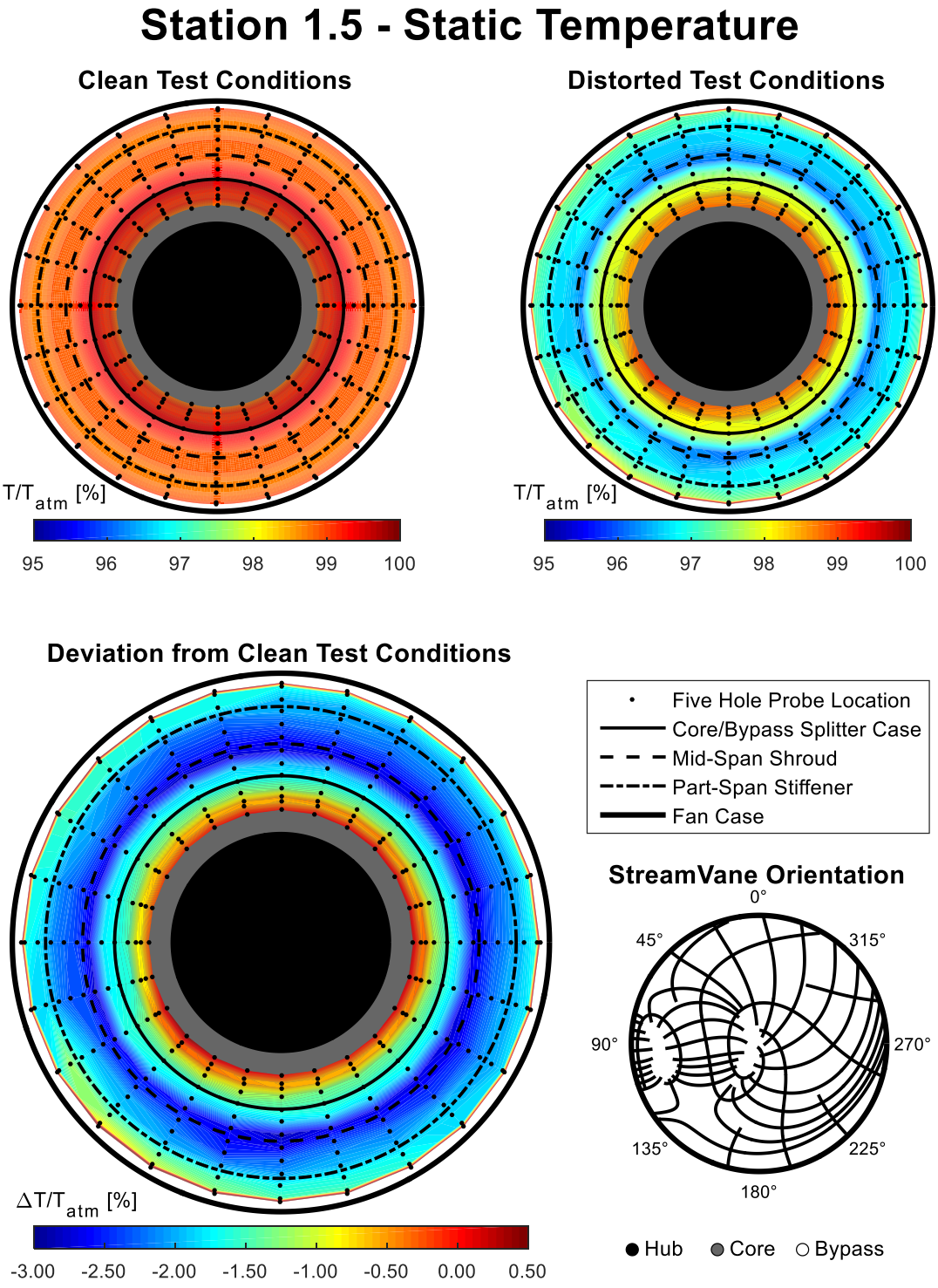

Figure D.3: Station 1.5 Static Temperature Results